SPECTROSCOPIC STUDY OF A BRIGHT MASER SOURCE - METHANOL MASER G9.62 + 0.19E: THEORY AND OBSERVATIONS

A THESIS SUBMITTED TO AUCKLAND UNIVERSITY OF TECHNOLOGY IN PARTIAL FULFILMENT OF THE REQUIREMENTS FOR THE DEGREE OF MASTER OF SCIENCE (RESEARCH)

Supervisor
Prof. S. Gulyaev
Senior Lecturer. T. Natusch

January 2024

By
Hannah Mae Wetzel
School of Engineering, Computer and Mathematical Sciences

Abstract

Astrophysical masers are naturally occurring galactic sources of anomalously intense non-thermal microwave radiation. The study presented in this thesis focuses on the analysis of the Class II methanol maser source G9.62 + 0.19E through theoretical modelling, observations, data processing, and spectral analysis. This active stellar region is of particular interest due to its high, quasiperiodic variability – as well as it being the brightest recorded methanol maser. The study of maser sources is crucial for validating their role as sensitive tracers of celestial objects and facilitating the exploration of their unique properties, aiding in measuring physical parameters and understanding the kinematics of our Galaxy.

We review approaches to deriving the radiative transfer equation for unsaturated masers of different geometries, consulting both standard and semi-classical maser theory variations. A simplified form of the radiative transfer equation is derived for approximating an unsaturated spherical maser source and used for numerical modelling of spectral line shapes in active (masing) media.

Our findings reveal that the maser spectral line shape deviates from a single Gaussian, comprised of a strong narrow peak on a wide (Gaussian) pedestal. Demonstrating that the ratios of amplitudes and widths between the narrow and wide features are dependent on the maser source's optical depth. These ratios enable the determination of individual maser source optical depth and, consequently, key astrophysical parameters like density, temperature, and pumping mechanism, given knowledge of the object's geometry and size.

As a case study, observations of the 6.67 GHz methanol maser source G9.62 + 0.19E were conducted using the New Zealand 30-m radio telescope at Warkworth. Implementing multiple frequency switching (MFS) confirmed the presence of a wide pedestal - typically excluded in standard polynomial continuum reduction. Utilizing amplitude

and width ratios of the narrow peak and pedestal, we determined the optical depth to be within the range of $\tau = 4 \rightarrow 6$.

To further validate this method, future studies should encompass more refined numerical modelling and observations of other maser sources.

Contents

List of Tables

List of Figures

Attestation of Authorship

I hereby declare that this submission is my own work and that, to the best of my knowledge and belief, it contains no material previously published or written by another person nor material which to a substantial extent has been accepted for the qualification of any other degree or diploma of a university or other institution of higher learning.

Signature of student

Acknowledgements

I would like to commence by expressing my deep gratitude and admiration for my supervisor, Professor Sergei Gulyaev. For most of my tertiary education, he served as the Director of the Institute for Radio Astronomy and Space Research (IRASR) at the Auckland University of Technology. Without his unwavering support and belief in my abilities as an aspiring astrophysicist, I might not have reached the level I am at today. From my first astronomy lecture at the age of 18, I was captivated by the grandiose way he spoke of the Universe. Professor Sergei Gulyaev has nurtured my wax-poetic view of the study of the cosmos, and I hope I never forget how beautiful he helped me believe it to be. Over the last six years, I have been privileged to grow under his vote of confidence, which has made all the difference. I am forever thankful for his mentorship and companionship.

I extend my sincere thanks to the other team members of the IRASR, some of whom have also been my instructors. The work involving the observation of masers would not have been possible without the guru-like knowledge of Tim Natusch. His contributions to this thesis as a mentor and secondary supervisor, along with his specialized knowledge of data processing and radio astronomy, have been invaluable.

My gratitude extends to my family, both found and biological. These past couple of years have been profoundly challenging, and I struggle to find adequate words to express my appreciation and love for all of you. My academic journey has been lengthy, but my indebtedness to you extends far beyond that. I will always strive to make you proud, but, above all else, happy.

Dedication

Perhaps this part will be the hardest to write. There are some things that can be studied and prepared for, and some things that cannot; "Not everything feels like something else." Two years ago, I promised my mother that I would finish my thesis and dedicate it to her. It pains me more than words to be dedicating this to her posthumously. Countless times I have found myself asking, "What am I supposed to do without you?" Consider this my first expression and declaration of how I will live again. Reborn from a loss that I didn't know my body could take. I will unclench my teeth, and feel like something else.

If grief is love persevering,
then I will never stop.
If grief is love with nowhere to go,
I will send it to your last known address.

I know precisely the way you would smile at me, hearing I had finally finished this. I know, devastatingly, the way you would hold me. I hope you are not far away and that you can feel how much I love you. I wish you could have helped proofread this for me. I would also like to dedicate this, in part, to my nieces. I'm sorry that I haven't been at home with you while you grow up. I hope that someday you will see this and feel proud of your Aunty. Whenever I feel disenchanted with the world, I think of you. I love you.

Chapter 1

Introduction

For thousands of years, mankind has been enraptured by the inscrutable qualities of the cosmos. Our innate and relentless desire to seek knowledge and understand our Universe is an inevitable, and integral part of human nature. This study aims to contribute to our understanding of the physical conditions within bright cosmic masers. Cosmic masers are natural amplifiers of radio waves found in space that emit a specific frequency of radiation and are typically associated with regions of high densities of gas and dust, such as protostars, massive old stars, the interstellar medium, and the centres of galaxies.

Throughout this introductory chapter, topics relevant to this thesis will be explored in detail to provide a comprehensive understanding of the subject. The order of topics will be presented in a way that gradually unfurls the complexities and nuances of cosmic masers, such that by the end, the reader will be familiar with the rationale behind the objectives considered in this research. The information provided in this chapter will be divided into five categories: Section 1.1 will provide a brief historical background on the field of cosmic masers. Section 1.2 will discuss population inversion and the conditions necessary for sustaining maser activity. Section 1.3 will delve into aspects of astrophysical maser environments and parametric components that impact their spectra.

Section 1.4 will discuss the current theories surrounding the periodicity and variability of cosmic masers, with an emphasis on the methanol maser G9.62 + 0.19E. Finally, Section 1.5 will lay out the structure of the rest of the thesis and what can be expected from each chapter herein.

The area of study surrounding astrophysical masers and the nature of their environments has proven to be of high contemporary interest and value. As a relatively new branch of astrophysics, there is an abundance of unexplored areas of research in this sphere. Multiple projects involving masers have already been undertaken, with astrophysical masers being used as both the primary focus and as tools for studying other objects. Due to their compactness, high brightness, and pervasiveness, astrophysical masers are distinctive tools for gaining insight into the stages of star formation (Ginsburg & Goddi, 2019).

Maser spectra hold considerable significance due to their practical utility. There is much to be extracted about the physical conditions of their environments from the emission spectra/lines of maser sources. From the spectra, one can determine the optical depth, density, length, chemical composition, kinetic temperature, degree of ionization, velocities, turbulence, and geometry of the maser media (Sobolev & Gray, 2012; Gray, 2012). The above parameters can be further used as indicators of the wider environment of the star formation regions (SFR). For instance, Very Long Baseline Interferometry (VLBI) studies have shown that masers emission lines can provide information about accretion structures, molecular shocks in outflows from high-mass star-forming regions (HMSFR), and disk winds in the circumstellar environments of protostars (Goddi, Moscadelli & Sanna, 2011; Matthews et al., 2010).

The purpose of this research is to document the process of examining standard maser theory and implementing it in a practical way by using it to model an observed maser spectrum. The final objective is to extract information about the physical characteristics

of the maser source from the spectral data. This work will detail the review of theoretical works, the execution of maser observations, data processing, spectral modelling, and the evaluation of the model's goodness of fit.

Within this thesis, methanol maser G9.62 + 0.19E will serve as the case study subject to demonstrate the proposed modelling, observation, and data processing techniques. G9.62 + 0.19E is the brightest maser currently catalogued, with a distinctive main spectral feature. The defined methanol peak gives the advantage of simpler modelling, and the high intensity allows for the exploration of the effect of extreme masing mediums on the spectral shape. This source is also easily observed from within the southern hemisphere, making it an ideal candidate to study with the radio astronomy facilities available at the Warkworth Observatory, located in Auckland, New Zealand. The information presented in the rest of this chapter will further contextualize the aforementioned details about this study and astrophysical masers themselves.

1.1 Historical Background of Cosmic Masers

In this section, we will briefly review the pivotal historical milestones that facilitated contemporary research on astrophysical masers.

1.1.1 Optical and Radio Telescopes

In 1608, the first optical telescope was created by Hans Lipperhey, capable of magnifying objects threefold. A year later in 1609, Galileo Galilei enhanced the design to achieve twenty times the magnification. These advancements in optical astronomy led to the first recorded observation of the Orion Nebula. This observation was made in 1610 by the French astronomer Nicolas-Claude Fabri de Peiresc (Williams, M., 2015). 350 years later, the Orion Nebula would serve as the source of the first observed cosmic

maser emissions (Weaver, Williams, Dieter, & Lum, 1965; Cheung et al., 1969).

In 1937, 26-year-old engineer, Grote Reber, constructed the world's first dish antenna radio telescope. Using his 31-foot diameter (~ 9.5 meters) telescope, Reber successfully mapped the radio structure of the Milky Way and identified powerful sources of radio waves beyond our galaxy. His pioneering work also contributed to the discovery of non-thermal radiation by physicists, thereby laying the foundation for modern radio astronomy (National Radio Astronomy Observatory, 2023).

1.1.2 Laboratory and Astrophysical Masers

In 1951, Charles. H. Townes first conceived of the maser - microwave amplification by stimulated emission of radiation (Boyd, 2015). Townes' wartime work on radar provided him with an in-depth knowledge of microwave science, inspiring the idea that coherent microwave radiation could be produced by inducing population inversion between two energy levels via an external pump source. In December of 1953, Charles H. Townes and his colleagues built the first maser, using ammonia gas as the masing medium. The work of Charles. H. Townes and Arthur Schawlaw, published in 1958, laid the foundations for the discovery and eventual modelling of cosmic masers (Schawlow & Townes, 1958). The Nobel Prize in Physics 1964 was divided between Charles H. Townes $\left(\frac{1}{2}\right)$, Nicolay G. Basov $\left(\frac{1}{4}\right)$, and Aleksandr M. Prokhorov $\left(\frac{1}{4}\right)$ "for fundamental work in the field of quantum electronics, which has led to the construction of oscillators and amplifiers based on the maser-laser principle" (NobelPrize.org, 2023).

In 1965, unexpected emission lines at a frequency of 1665 MHz, of unknown origin, were discovered by Weaver et al. (Weaver et al., 1965). During this period, the discovery of molecules in space (McKellar, 1940) was not readily accepted by researchers, resulting in the unidentified emission being attributed to an unknown form of interstellar matter called 'Mysterium'. However, the emission was later identified as a spectral line

emission from hydroxide molecules (OH) located in compact sources within molecular clouds in the Orion Nebula (Cheung et al., 1969). In the preceding decade, discoveries of water (1969), methanol (1970), and silicon monoxide emissions (1974) were made. All of which emanated from within molecular clouds.

1.1.3 Einstein's Coefficients and The Theory of Radiation

Predating the construction of the first radio telescope and the conception of the maser, Einstein hypothesized the process of stimulated emission in his investigation of the Quantum Theory of Radiation (Einstein, 1917). Einstein proposed that from his analysis of the similarities between the spectral curves of Planck's chromatic distribution of black body radiation and Maxwell's velocity distribution, that the "elementary processes of emission and absorption obtain another support" (Einstein, 1917). In short, Einstein proved (through a series of derivations involving pre-existing quantum theory) that based on the rates of spontaneous emission and stimulated absorption, balance could not exist without the inclusion of a third process: Stimulated emission (Gray, 2012). In this paper, Einstein introduced a set of coefficients that serve as a measure of the probability of emission or absorption of radiation by an atom or molecule (Hilborn, 1982).

1.1.3.1 Spontaneous Emission

Spontaneous emission (Fig. 1) describes the process whereby an atom, molecule, or ion transitions from an excited state to a lower energy state, emitting quantized energy in the form of a photon. The frequency of the emitted photon corresponds to the change in energy between the excited and lower states. The process is considered spontaneous because the quantum system may decay to a lower energy state without external stimuli (Kwok, 2007). The occurrence of decay is probabilistic and often characterized by

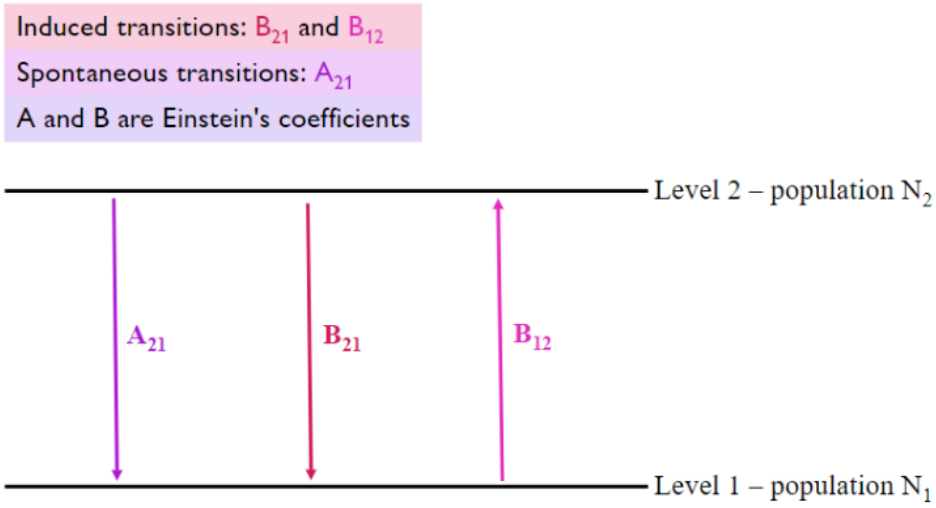

Figure 1.1: Visual representation of Einstein's Coefficients and the transitions associated with their radiative processes.

some time constant that represents the average time before transition (Hecht, J., 2021).

Let

$$\Delta E_{ij} = E_i - E_j = h\nu_0 \tag{1.1}$$

represent the spontaneous transition of a quantum mechanical system from the excited energy state E_i to the lower energy state E_j. Where h = Planck's constant, ν_0 = frequency of the emitted radiation, and $h\nu_0$ = energy of the emitted radiation. From the above scenario, Einstein devised an equation for the probability of the transition taking place.

Let dW be the probability that spontaneous emission occurs over a time period dt.

$$dW = A_{ij}dt \tag{1.2}$$

Where $A_{ij}(s^{-1})$ is the Einstein coefficient for the probability per unit of time that a system in the excited energy state E_i will spontaneously decay to the lower energy state E_j emitting radiation of energy $E_i - E_j = h\nu_0$ (Einstein, 1917).

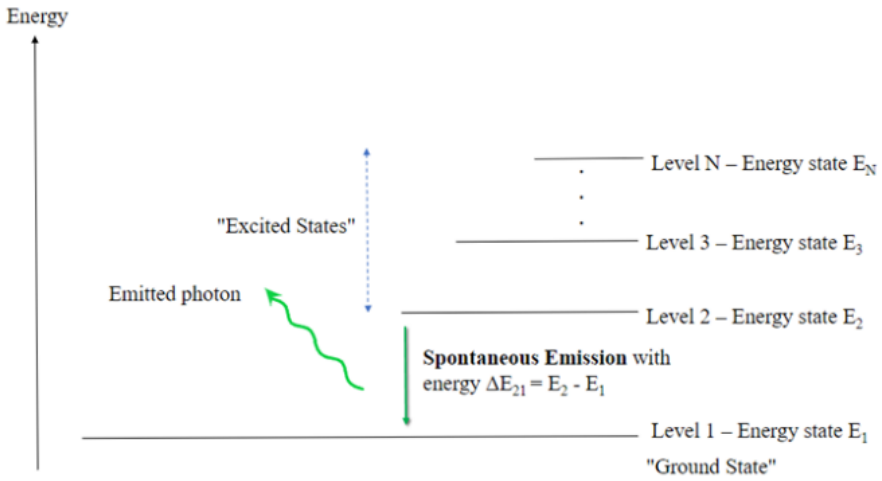

Figure 1.2: Energy level diagram depicting the spontaneous emission process of a quantum mechanical system with *'N'* energy states.

1.1.3.2 Stimulated Absorption

Complimentary to this process, there is (stimulated) absorption (Fig. 2) which describes the interaction between a quantum mechanical system and outside radiative sources. Stimulated absorption takes place when an incoming photon of a particular frequency collides with the atom/molecule and causes the internal energy level to jump to an excited state. As with spontaneous emission, the energy levels between states are quantized and the energy of the incoming photon must coincide for the absorption to take place. The coefficients for the "induced radiation processes" (Einstein, 1917) are as follows:

Let dW be the probability that under the radiation density ρ and with frequency ν, a molecule will make the transition between energy state E_j to energy state E_i via the absorption of energy equivalent to ΔE_{ji} over a period of time dt.

$$dW = B_{ji}\rho dt \tag{1.3}$$

Here, $B_{ji}(m^3 J^{-1} s^{-2})$ is the Einstein coefficient for the probability of the transition

from energy state E_j to energy state E_i via absorption of radiation under the above conditions.

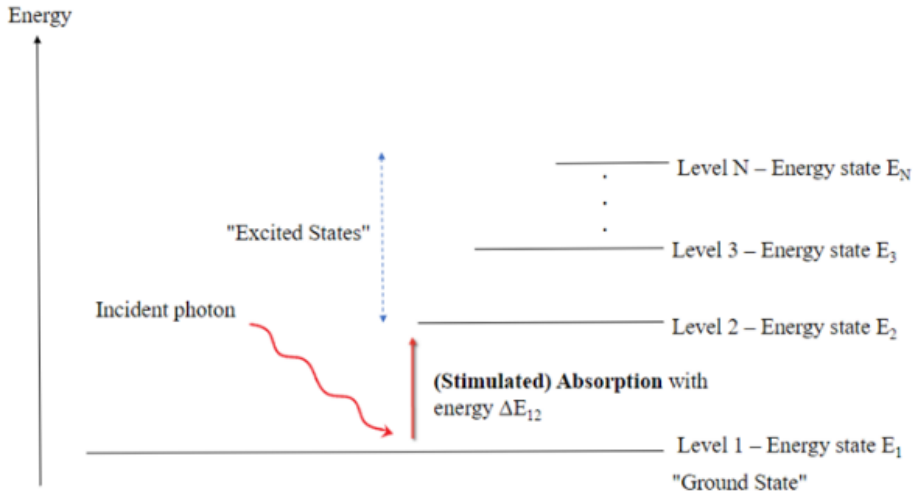

Figure 1.3: Energy level diagram depicting the stimulated absorption process of a quantum mechanical system with *'N'* energy states.

From this, Einstein then stated a transition like that associated with the A_{ij} coefficient could be possible under the influence of radiation.

$$dW = B_{ij}\rho dt \tag{1.4}$$

This hypothesized transition and corresponding coefficient $B_{ij}(m^3J^{-1}s^{-2})$ would later be described as Stimulated emission (Fig. 4).

1.1.3.3 Stimulated Emission

Stimulated emission occurs via the same process seen in stimulated absorption, whereby the quantized energy of an incident photon is absorbed and causes an opposite but identical transition in energy levels (from lower to higher) (Dirac, 1927). However, stimulated emission happens exclusively when an incoming photon interacts with a quantum mechanical system that is already in an excited state. The interaction results

in the molecule undergoing a downward transition to a lower energy state, whereby the incident photon then continues to propagate alongside an identical photon emitted from the transition. This degeneracy is unlike that of spontaneous emission where a single photon is emitted stochastically. Rather, stimulated emission results in two identical photons of a predictable nature (Kwok, 2007).

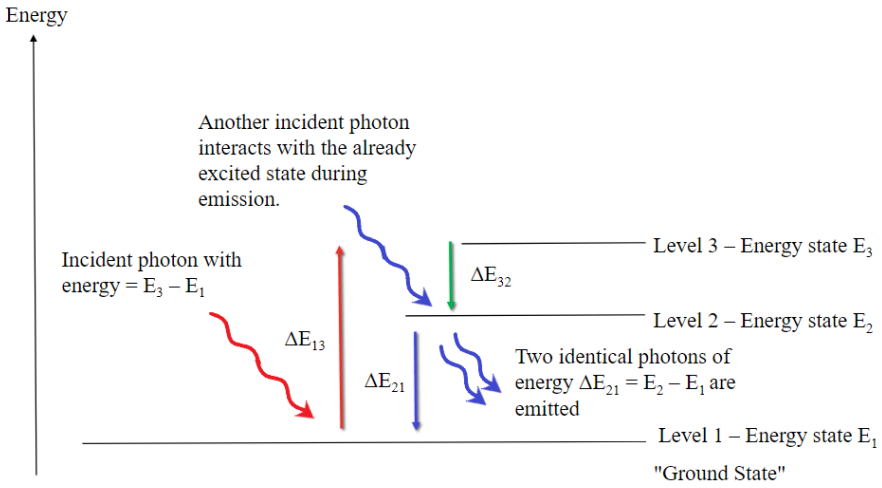

Figure 1.4: Energy level diagram depicting the stimulated emission process of a simple maser with three energy states.

The energy liberated from the subsequent absorption and emission of the incident photon is transferred to the electromagnetic field, where a 'new' photon is generated. Both the emitted photons will be coherent (of the same frequency, phase, polarization, and direction) with the incident photon (Kwok, 2007).

In the presence of several other atoms (or molecules) in the same initial state, stimulated emission causes a chain reaction where the emitted coherent photons continue to interact with other excited systems resulting in more stimulated emissions. Each time the process repeats, the number of coherent photons that are available for collisions increases by two. This chain reaction is exponential and is the source of amplification of maser radiation. However, for the maser effect to be observed, net microwave amplification must be achieved through a sufficient rate of stimulated emission within a population

Incident Photon(s)	Initial Energy State	Outcome
	(Ground or Excited)	
	Ground state	
	Excited energy state	

Figure 1.5: Table of relevant photon interactions within a quantum mechanical system.

(Gray, 2012).

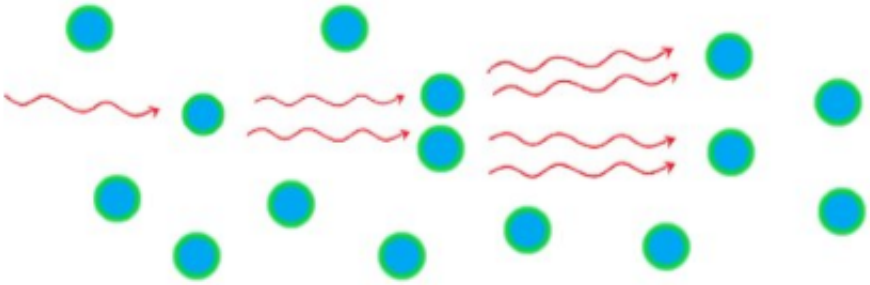

Figure 1.6: Illustration of the chain effect of stimulated emission within a population of quantum mechanical systems.

1.2 Population Inversion

The condition needed to sustain an adequate rate of stimulated emission is *population inversion*. The principle of population inversion is first and foremost an expression of statistical mechanics. Population inversion describes a system (in this case, of atoms or molecules) in which the majority of the members are in an excited state. The nomenclature of population inversion refers to the contradictory nature of having a system in which higher energy states are more probable. Physical systems are governed

by a hierarchy of different degrees of thermodynamic equilibrium. Most physical systems are in complete or local thermodynamic equilibrium and can be modeled by a Boltzmann distribution – for this reason, most natural environments cannot sustain population inversion (Svelto, 1998).

1.2.1 Equilibrium Breakdown

It is expected that within a system, in the absence of any process other than internal collisions, the objects of the system will disperse themselves across the possible energy states according to the equilibrium distribution derived by Boltzmann (Gray, 2012). The Boltzmann distribution is a probability distribution that defines the probability of a system being in a certain energetic state based on the energy of said state and the temperature of the system (McQuarrie, 2000). Given the above description of a system in thermodynamic equilibrium, let us examine the Boltzmann distribution under the conditions required for population inversion.

Let N_j represent the number of atoms or molecules in the ground state and N_i correspond to the amount in excited states, where the total population of the system is N.

$$N_j + N_i = N \tag{1.5}$$

The Boltzmann distribution gives the ratio of particles in N_i and N_j as a function of the difference in energy between states i and j and the temperature (T) of the system (Gray, 2012).

$$\frac{N_j}{N_i} = \frac{g_i}{g_j} e^{-\frac{E_i - E_j}{kT}} \tag{1.6}$$

Where g_j and g_i represent the statistical weights (degeneracies) of the states, k is the Boltzmann constant, T is the temperature of the system, and E_i and E_j are the respective energies of states i and j.

This equation can be manipulated to give an expression for the population difference ΔN_{ij}.

$$\Delta N_{ij} = \frac{N_i}{g_i} - \frac{N_j}{g_j} \tag{1.7}$$

Whereby rearranging equation (1.6) we get:

$$\frac{N_i}{g_i} = \frac{N_j}{g_j} e^{-\frac{\Delta E_{ij}}{kT}} \tag{1.8}$$

Then by substituting (1.8) into (1.7), we arrive at

$$\Delta N_{ij} = \frac{N_i}{g_i} - \frac{N_j}{g_j} = \frac{N_j}{g_j}\left(e^{-\frac{\Delta E_{ij}}{kT}} - 1\right) \tag{1.9}$$

Population inversion requires the ratio of $\frac{N_i}{N_j}\frac{g_j}{g_i} > 1$, in which the emission process dominates. For this to be true, ΔN_{ij} must then be positive.

In using the Boltzmann distribution for thermodynamic equilibrium, we thereby assume that the exponential component is always negative, thus, the term inside the brackets will also be negative. Since the minimum value of the statistical weight (g_j) of a non-degenerate level (N_j) is 1 (Gray, 2012), for the resulting product (ΔN_{ij}) to be positive, the value for N_j would have to be negative. This is a contradiction, as it is physically impossible for there to be a negative quantity of particles in an energy state. Therefore, population inversion cannot be achieved in a system that exists in thermodynamic equilibrium. Consequently, the physical processes responsible for the

mechanisms observed in cosmic masers are classified within the domain of non-local thermodynamic equilibrium (Non-LTE) physics (Gray, 2012).

1.2.2 Pumping

Pumping is the mechanism responsible for driving the maser system away from thermodynamic equilibrium. The pumping process involves introducing externally sourced energy into the maser system (in the same sense that one pumps fuel into a car). The source that supplies energy to the maser (gain) medium is referred to as the pump source (Gray, 2012). The energy pumped into the system enables the mass excitation of molecules in the ground state up to a higher energy state. The increased rate of excitation allows for the distribution of the population between energy states to favour higher energy states (population inversion).

1.2.3 Three and Four Level Maser Systems

Population inversion can be achieved within a system with a minimum of three energy levels (Fig. 4). Although three-level systems are by no means ideal, they provide an environment suitable for the induction of population inversion. If we were to consider a simplified system with only two possible energy states, the only allowed transitions would be excitation from the ground state to the second state, and de-excitation from the second state into the ground state. In this scenario, the second state is 'short-lived', meaning the time until decay is almost instantaneous. Due to this, the excited molecules would return to the ground state incredibly quickly (meaning the pump source would need to be very efficient to sustain population inversion).

Stimulated emission is necessary to produce coherent photons; a process that can only occur when an incoming 'passer-by' photon interacts with a system already in a state of excitation. The incident photon must approach the excited quantum mechanical system

before it decays back to the ground state. A consequence of spontaneous decay is that all energy levels except the ground state have a finite width (Gray, 2012). The characteristic lifetime of an energy state is modeled by Heisenberg's uncertainty principle for energy and time:

$$\delta E_{ij} \delta t_{ij} \approx \frac{\hbar}{2} \tag{1.10}$$

where δt_{ij} is the characteristic lifetime, δE_{ij} is the uncertainty in the transition and $\hbar$ is the reduced form of Planck's constant (h) divided by 2π.

To bide enough time for stimulated emission to take place, the lifetime of one of the excited states must be metastable (long-lived). Theoretically, in a Bohr model molecule, it should remain in a metastable state forever. However, the probability of the transition still exists (the exact value of this small probability is arbitrary, as we simply wait for an incident photon to initiate the transition).

In a three-level system, the depopulation of the ground state via pumping sends the majority of the system into the 'short-lived' third energy state of excitation - before an almost instantaneous decay to the second energy state (non-radiative transition). The second level in this system is metastable which allows enough time for stimulated emission to occur. For this reason, the three-level system exists as the most basic model. However, in a three-level system, population inversion is only sustained until a chain of maser emissions results in the rapid re-population of the ground state. For this reason, the output of three-level masers is not continuous, but rather pulses of maser radiation (Gray, 2012).

To achieve a continuous beam of maser radiation, a four-level system is required. In the case of a four-level maser (Fig. 5), the lower maser level is not the ground state. As a result, so long as the lifetime of the upper maser level is longer-lived than that

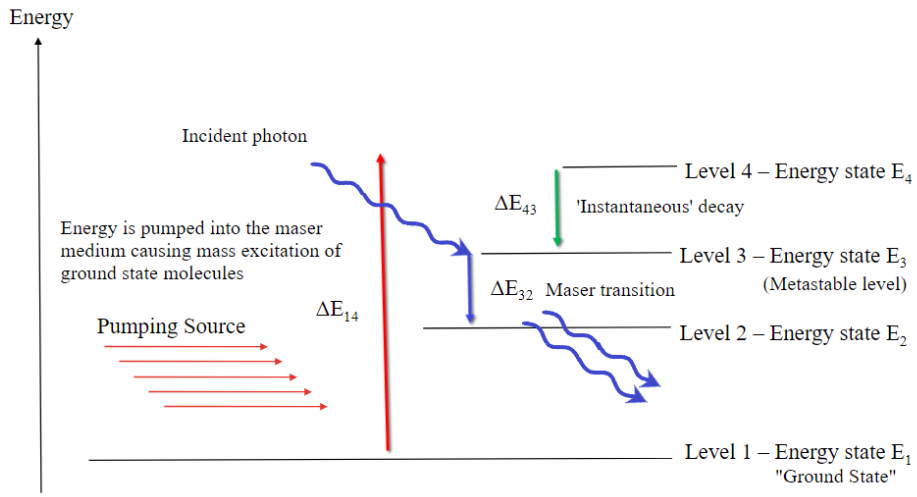

Figure 1.7: Energy level diagram depicting the 'pumping' process of a four-level maser system.

of the lower maser level, there is a lower power threshold for the pump needed to produce population inversion (Paschotta, 2008). The amplification of a four-level system involves the maser medium being pumped to the 4th energy level before a non-radiative transition occurs to the 3rd level. Since the 3rd level (the upper maser level) is metastable, molecules will accumulate in this energy state until stimulated emission occurs. After stimulated emission takes place and coherent photons are emitted, dropping the molecule to the 2nd level, a final non-radiative transition occurs whereby the molecule returns to the ground state (and pumping continues).

1.2.4 Methanol Molecular Levels

In reality, molecules have many radiatively allowed transitions, meaning the three and four-level models exist purely for demonstrational purposes. A methanol molecule could have several states of excitation higher than that of the metastable level (Fig. 6). Similarly, there could also be many lower energy states between the lower maser level and the ground state.

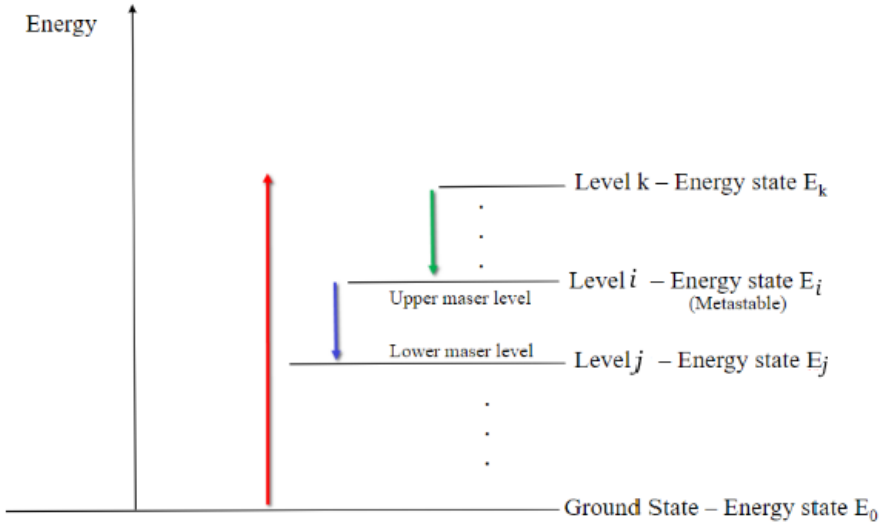

Figure 1.8: Energy level diagram of a methanol molecule with *k* energy states; in which the pumping process can be initiated from any level below the lower maser state and decay to the metastable level from any level above the upper maser level.

Accurate molecular energy level diagrams are far more complex than the above depictions - methanol molecules are no exception.

Numerous radiatively allowed transitions can occur within the states of a methanol molecule. The methanol molecule transition associated with the 6.7 GHz emission is between levels $5_1 - 6_0\, A^+$. The transition from the initial state (5_1) to the final state (6_0) describes the changes in the molecule's rotational and vibrational energy levels. The A^+ refers to the classification of the two types of symmetry found in methanol, denoted A and E. These symmetries are related to energy changes between atoms in the methanol molecule. Both A and E symmetries follow different rules when transitioning, and the key distinction lies in A-type transitions, which involve an $A\pm$ state indicating the parity of the spatial symmetry. These symmetries refer to the spin of the hydrogen within the CH_3 group, parallel and non-parallel in A and E methanol, respectively (Rabli & Flower, 2010).

Methanol molecules (CH_3OH) have a slightly asymmetric top, characterized by the methyl (CH_3) group's internal torsional movement around the molecular symmetry axis

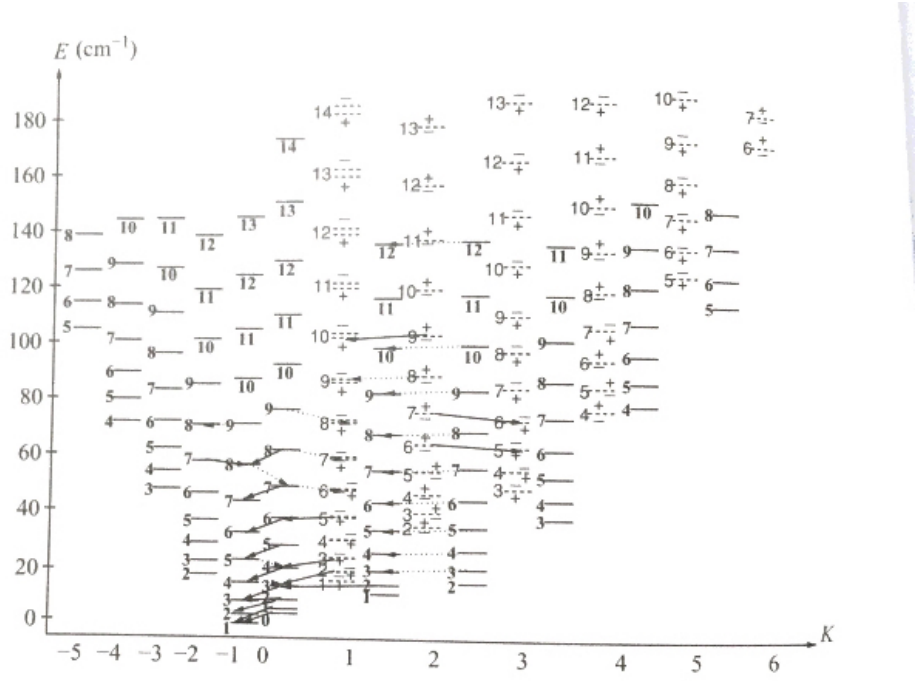

Figure 1.9: Energy levels of methanol. Taken from the Leiden Atomic and Molecular Database. Source: (Gray, 2012, page 184).

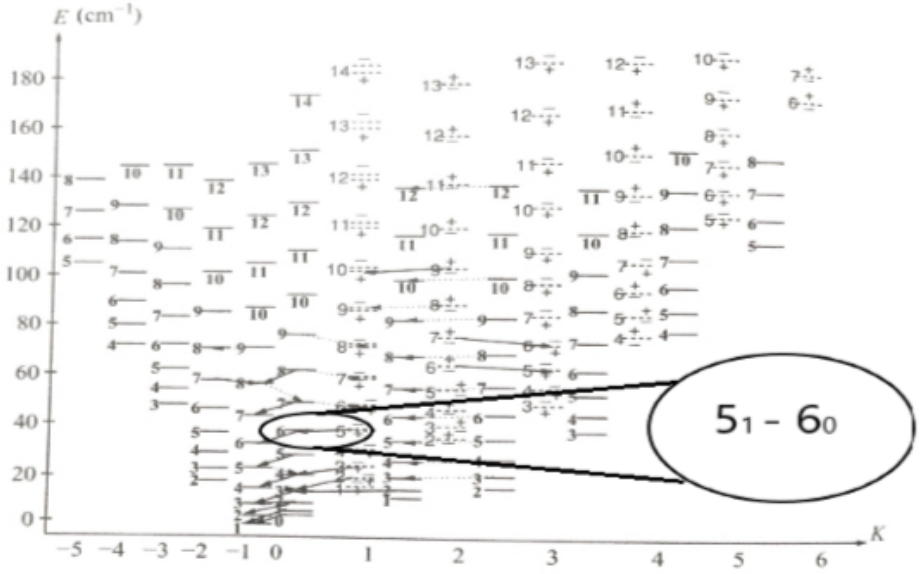

Figure 1.10: Methanol energy level transition corresponding to maser emission at 6.7 GHz Source: (Gray, 2012, page 184).

about the hydroxyl (OH) radical. This rotational motion represents a type of vibration, where the specific degree of freedom involved is an angle rather than the distance between the nuclei within the molecule (Rabli & Flower, 2010).

1.3 Astrophysical Masers

In 1991, Karl Menten discovered anomalously strong methanol maser emissions in galactic star-forming regions (Menten, 1991); many of the most notable observations showed high-intensity spectral lines at 6.7 GHz (Houghton & Whiteoak, 1995) (in full, the transition is 6.6668 GHz). Methanol maser G9.62 + 0.19E is the strongest source of 6.7 GHz emissions on record, with a spectral flux density in the range of 5000 to 7000 Janskys (Jy). The transition at 6.7 GHz is exclusively related to high-mass star-forming regions (HMSFR), which is indicative of the close association between Class II methanol masers and ultracompact HII (UC HII) regions (Gray, 2012).

In Menten's early studies, the two classes of methanol masers were empirically distinguished. Class II masers (at 6.7, 12, 37.7, and 107 GHz) are pumped by the infrared radiation of dust heated by young stars (Cragg, Sobolev & Godfrey, 2002, 2005; Voronkov et al., 2006), formed in the accretion disks in star-forming regions. Class I masers (at 36, 44, and 95 GHz) occur as a result of collisional-radiative pumping (Sobolev et al., 2007; Strel'nitskii, 1981). Class I masers are formed in bipolar outflows and usually indicate the presence of gas compressed by a shock wave (Ladeyschikov, Bayandina & Sobolev, 2019). Protostellar objects evolve within giant molecular clouds undergoing star formation.

Class II masers are also known as Late Masers, with the term "late" denoting the evolutionary stage of protostellar objects during which Class II masers are detected. Protostellar objects evolve within giant molecular clouds undergoing star formation.

Initially, material of low angular momentum within the molecular cloud experiences a short-lived gravitational infall, in which a dense, centralized mass is formed. A protostellar object in this phase is too cool to ionize its surroundings and continues to accumulate matter from an equatorial accretion disc. The poles of the protostar produce a material outflow, channeled by a combination of magnetic fields and radiative pressure. The formation of an HII region is initiated by the production of large amounts of ultraviolet radiation – a stage characterized by a significant increase in the protostar's temperature (Carraro, 2021; Kaplan & Pikelner, 1970; Kwok, 2007; Tielens, 2005).

From there, the HII region of the new star begins to envelop its surroundings, first as a hypercompact and then eventually as an ultracompact HII region. This evolutionary step corresponds to the formation of Class II masers. Dust in the protostellar material encasing the HII region serves as a frequency down-converter, in which ultraviolet stellar radiation is absorbed and re-emitted in the infrared range of the electromagnetic spectrum (Gray, 2012). For Class II masers, the most likely source of continuum pumping radiation is thermal emission from the aforementioned dust (Sobolev & Deguchi, 1994; Strel'nitskii, 1977). Thus, it is implied that the pumping of Class II masers requires radiation that is not self-generated by the maser molecules (radiative pumping). However, collisional population transfer is still likely to make a notable contribution as a pump source.

To observe a significant maser effect, astrophysical masers require a large gain (amplification of radiation). In turn, there must be a substantial concentration of molecules along the line of sight. However, violations of thermodynamic equilibrium tend to favour small molecular densities. To compensate for this, astrophysical masers have very large dimensions.

Laboratory masers and lasers amplify radiation in a highly tuned optical cavity. Usually, this optical cavity is controlled by a pair of mirrors, which enable multiple passages of

radiation through the amplifying medium. The result is several rounds of exponential chain reactions whereby the intensity, amplification, and coherence of the radiation can be controlled. In contrast, the amplification of astrophysical masers results from a single pass through the masing gas, where beams can amplify in many directions and frequencies. Therefore, the pattern of radiation emitted from astrophysical masers can reveal important aspects of its physical geometry (Gray, 2012).

1.3.1 Gain, Beaming, and Saturation

The intensity of a maser depends exponentially on the population inversion and the velocity-coherent path length. Regions of the molecular cloud with longer path lengths will appear brightest. For this reason, the beam of maser radiation will emerge from the longest path length, a phenomenon known as beaming. The exponential growth in intensity of radiation passing through a maser cloud continues so long as pumping processes maintain the population inversion against the growing losses by stimulated emission (Gray, 2012).

The above case corresponds to that of an unsaturated maser. Saturated masers have amplification that scales linearly with the size of the population inversion and path length (Goldreich & Keeley, 1972). Saturation in masers occurs when the rate of stimulated emission becomes comparable to the effective decay rate of the maser transition. At full saturation, the maser intensity reaches a maximum and does not increase further, even if the input radiation continues to increase. Regardless of saturation, the beam intensity increases with path length, meaning that both higher line-of-sight densities and greater optical cavity lengths produce higher degrees of maser amplification. The competition between different beams of radiation for available pump photons is a crucial factor in both unsaturated and saturated masers. This results in highly beamed radiation from a typical maser cloud, even in the case of a saturated maser, due to the asymmetric nature

of the cloud's shape (Alcock & Ross, 1985).

According to the standard theory of maser line widths, the width of maser lines is predicted to narrow when amplification is unsaturated, and then widen again to the full Doppler width when amplification becomes saturated (Goldreich & Kwan, 1974). As radiation propagates through the masing medium, the spectral line profile undergoes initial narrowing as the radiation intensity increases. Preferential amplification at the centre of the spectral line is the cause of this initial narrowing, as this is where the rate of stimulated emission and optical depth is maximized. At a sufficient intensity, the reduction of excited molecules at the line centre, due to saturation, is such that the amplification at the line centre drops below that in the wings. Here, the wings expand faster than the line centre and the line begins to rebroaden. In the presence of high enough intensities, the line ultimately expands to the full thermal width (Anderson & Watson, 1993).

1.3.2 Polarization

Strong maser sources, such as G9.62 + 0.19E, have magnetic field interaction as their main polarization mechanism (Deguchi & Watson, 1990). This polarization is independent of the intensity of incoming radiation but can be influenced by anisotropic pumping, which favours certain magnetic-state transitions (Lankhaar & Vlemmings, 2019). Linear polarization of the radiation from astrophysical masers involving molecules with closed electronic shells (and consequently, small magnetic moments), such as methanol (CH_3OH), is often a prominent feature of their spectra (Deguchi & Watson, 1990). In addition to the presence of a magnetic field in the masing region, geometrical effects in the transfer of the maser radiation can result in linear polarization. The degree of polarization is typically around 30% but can range up to complete polarization in some cases.

For non-paramagnetic molecules (molecules with no unpaired electrons), the magnetic fields present in the gas masing media are not strong enough to cause Zeeman splitting of comparable breadth to that of the spectral line widths (Deguchi & Watson, 1990). For diamagnetic systems with closed shells of electrons, the normal Zeeman effect is observed (Morgan & Kühne, 2020). The Zeeman effect describes the splitting of spectral lines in the presence of a magnetic field, which arises due to the principal quantum number of each state being separated into different substates.

More specifically, the Zeeman effect results from the energy difference between states with more than one direction for the angular momentum vectors when their orbital degeneracy is lifted by an external magnetic field (Morgan & Kühne, 2020). Since the manifestation of the Zeeman effect depends on both the strength of the external field and the magnetic moments of unpaired electrons (Morgan & Kühne, 2020; Petasis & Hendrich, 2015), the splitting of non-paramagnetic molecules is extremely small (Vlemmings, Torres & Dodson, 2011); such is the case for methanol masers, including G9.62 + 0.19E.

1.3.3 Optical Depth

Optical depth quantifies the rate of change of intensity over the change in distance from a source through some medium. In the case of astrophysical masers, the change in intensity refers to the amplification of radiation over some propagation distance through the gain medium (Kwok, 2007). This relationship is given by the radiative transfer equation:

$$dI_\nu = -I_\nu \alpha_\nu dr + \epsilon_\nu dr \tag{1.11}$$

where I_ν is the intensity of the incoming radiation (with respect to frequency), α_ν is

the absorption coefficient of the media, ϵ_ν is the emission coefficient and dr is the path length.

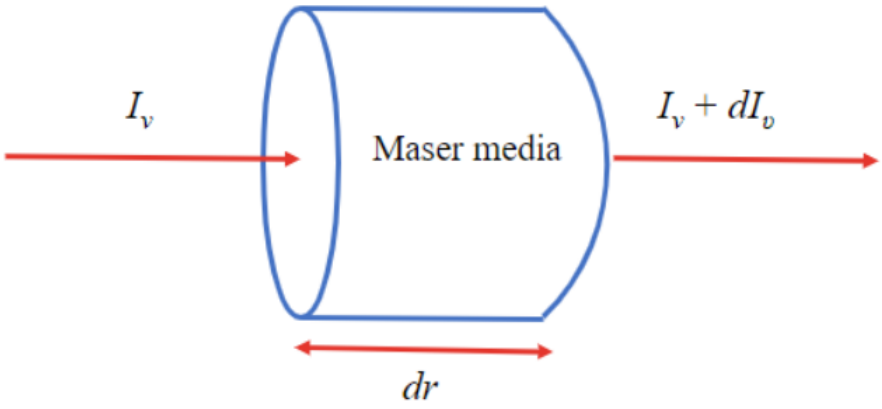

Figure 1.11: Visual depiction of the radiative transfer equation through a maser medium.

$$\frac{dI_\nu}{dr} = -I_\nu \alpha_\nu + \epsilon_\nu \tag{1.12}$$

To derive a term for the optical depth, we consider radiative transfer where only absorption occurs during propagation through the medium.

We take $\epsilon_\nu = 0$ then $\frac{dI_\nu}{dr} = -I_\nu \alpha_\nu$

Since optical depth represents the property of transparency of a medium, we can then consider optical depth (τ_ν) to be a measure of the progressive change of intensity over a distance (dr) that can be expressed by the ratio of the change in intensity and the initial intensity $(\frac{dI_\nu}{I_\nu})$. Using this relationship, we can rearrange the above formula to solve for the optical depth:

$$\tau_\nu = \int_0^R \alpha_\nu dr \tag{1.13}$$

From the above expression, it can be deduced that a large optical depth (τ_ν) can occur

because the maser media is efficient (strong population inversion) or the path through the media is very long.

1.3.3.1 Geometry

Within this paper, we consider the case of a cylindrical maser pathing through a globular medium. A visual of the proposed maser pathing will be provided in Chapter 2 - Section 2.4.2. Long thin tubes and spherically symmetric masers have been discussed in detail by Goldreich and Keeley (1972), Litvak (1973), and Reid et al. (1977; 1980). In the work of Goldreich and Keeley (1972), it is stated that there are two main reasons for suspecting that astrophysical masers are more often like tubes than spheres. Namely, the observed velocity differences (of the magnitude of several 10's of kilometers per second) among individual masers in a source complex, and the transfer of pump radiation in the sources. A more in-depth discussion of the geometries explored in Goldreich and Keeley (1972) will be featured in Chapter 2.

1.4 G9.62 + 0.19E Periodicity and Variability

In practice, when it comes to maser environments, the previous description of the conditions that surround Class I and Class II maser types are merely general classifications. The reality of astrophysical masers and their unique conditions is more nuanced. Certain maser behaviours have prompted researchers to delve deeper into the intricacies of their environments in an attempt to understand the underlying causes of these behaviours.

In 2003, Goedhart, Gaylard, and van der Walt discovered periodicity in the class II methanol masers associated with G9.62 + 19E (Goedhart, Gaylard & van der Walt, 2003). Presently, there are 25 known periodic maser sources – though, the cause(s) of maser periodicity and variability remain open for debate. The competing proposed

explanations for the phenomenon are a pulsating protostellar object (Inayoshi, Sugiyama, Hosokawa, Motogi & Tanaka, 2013; Sugiyama et al., 2015), periodic accretion (Araya et al., 2010), a rotating spiral shock (Parfenov & Sobolev, 2014), or a colliding wind binary system (van der Walt, Maswanganye, Etoka, Goedhart & van den Heever, 2016; van den Heever, van der Walt, Pittard & Hoare, 2019). As mentioned previously, G9.62 + 19E is an HMSFR with a hypercompact H II region (Garay, Rodriguez, Moran & Churchwell, 1993) and various maser species projected against it (Sanna et al., 2015; Sugiyama et al., 2015). It was shown by van der Walt, Goedhart, and Gaylard (2009) that the 6.7, 12.2, and 107 GHz methanol transitions flare simultaneously and are periodic. The best-fitting period of this prototypical periodic methanol maser was determined to be 243.3 days, by Goedhart et al. (Goedhart, Maswanganye, Gaylard & van der Walt, 2014).

1.4.1 Pulsating Protostellar Object

In both the works of Inayoshi et al. (2013) and Sugiyama et al. (2015), it is proposed that the periodic flux variations shown by 6.7 GHz methanol maser emissions can be explained by the pulsation of massive protostars growing under rapid mass accretion rates. Inayoshi et al. (2013) examine the pulsational stability of the bloated massive protostars with a linear stability analysis. Their results show that the observed periodicity of approximately 10–100 days can be well explained with stellar pulsation.

Alternative explanations are also discussed within the paper, with the authors explaining that binary-based models (periodic accretion (Araya et al., 2010) and colliding wind binary systems (van der Walt et al., 2016; van den Heever et al., 2019)) do not explain why periodic variations shorter than 10 days have not yet been identified - even though several OB star eclipsing binaries have periods of less than 10 days. However, a reason for this disparity was provided, stating that the flux variation period depends on the

accretion rate; with the variation period extending as the accretion rate increases. On the other hand, protostars with lower masses become unstable but fail to produce periodicity - which could also explain why a periodic variability shorter than 10 days has not been observed (Inayoshi et al., 2013). Sugiyama et al. (2015) provide similar reasoning supporting the theory of pulsating protostellar objects.

The results derived from their observations were indicative of a period of approximately 53 days, which is within the range proposed by Inayoshi et al. (2013). However, though both papers provide approximate periodicities, supported by mathematical relations describing the flux of maser emissions and the pulsation of the protostars pumping radiation into the maser media, the question at hand remains very open. Neither publication showed definitive proof that this theory is widely applicable, but mostly that the prospect of a pulsating protostar being the cause of maser periodicity is valid.

1.4.2 Periodic Accretion

Araya et al. (2010) published a paper detailing the results of their observational campaign using the Arecibo Telescope, the Very Large Array, and the Green Bank Telescope, to monitor the 6 cm formaldehyde maser in the young massive stellar object G37.55 + 0.20. During this campaign, they discovered quasi-periodic formaldehyde flares with a period of approximately 237 days, where they propose that the flares could be attributed to variations in the infrared radiation field, in which they could be possibly modulated by periodic accretion onto a young binary system (Araya et al., 2010).

In the paper, it is disclosed that although the flares were well sampled, in certain instances (such as in August 2009), they were still unable to make a good determination of its peak. When referring to observations made on the Arecibo telescope of 6.7 GHz methanol masers, it is stated that behaviour of the different methanol components shows that the flares are not caused by a homogeneous and large-scale change in

the background radio continuum. In addition, the possible link between flares and propagating sound/density waves or shock fronts is partially debunked. Rather, a radiative origin of the flares is offered as a more likely solution, with the authors explaining that if the two maser regions are in the plane of the sky with the source of pumping radiation between them, then the radiation front would take only about six days to reach the maser regions. This travel time provides a better match to the time scales of the flares.

In addition, changes in maser gain due to variability of the radiation field are consistent with the excitation mechanism of Class II methanol masers (Araya et al., 2010). Though the observations were thorough, and the explanations were supported with tangible evidence, the work fails to provide a compelling case for periodic accretion being the favourable theory for the cause of periodic maser flares.

1.4.3 Rotating Spiral Shock and Colliding Wind Binary System

In Parfenov and Sobolev (2014), reference is made to the other pre-existing theories surrounding maser periodicity. Mention is made to van der Walt (2011) and the proposed relation of maser variability with background variations. In this case, the background variations are caused by the variability of colliding winds in a massive binary. Similarly, Inayoshi et al. (2013) is referenced regarding the suggestion that dust temperature variations could be caused by pulsations of a massive protostar growing under high accretion rates. Araya et al. (2010) is also cited as explaining the dust temperature variations by the variability of the accretion rate of the disc material onto a young binary system.

Parfenov and Sobolev assert that at the time of publication (2014), there was a lack of strong evidence that the Class II methanol masers in any variable source with confirmed periodicity reside in the circumstellar disc. Alternatively, the authors consider the

possibility of explaining periodic methanol maser phenomena in the model with the masers produced in an accretion disc containing a binary system and rotating spiral shocks in its central cavity. In such a case, the disc model being considered is that of when a Class II methanol maser is formed in the accretion disc around the protobinary star containing large and intermediate-mass stars.

Here, there is a gap in the disc centre formed by rotating bow shocks. It is also assumed that the gas in the accretion disc is in thermal and ionization equilibrium. The theory centres around the luminosity and spectrum of the radiation being subject to variations due to the rotation of the bow shock. The results of the study showed that within the circumbinary accretion disc, the illumination of the disc by the bow shocks hot material led to variation in the dust temperature in the disc. The shock-induced variation in dust temperature was associated with a considerable increase in the probability of maser flares in the disc (Parfenov & Sobolev, 2014).

1.5 Thesis Outline

In Chapter 2, theoretical works detailing the derivations and formulations of the standard and semi-classical maser equations will be reviewed. Using these existing works as a foundational guideline, a theoretical maser model will be constructed through the analytical (non-numerical) solution to the equation of radiative transfer. This maser model will be used to generate theoretical maser spectra over a range of optical depth values. The theoretical maser spectra will be used as a means of testing the use of multiple Gaussian curves to approximate the main spectral feature. The multiple Gaussian approximations will later be used to fit the observed spectrum of G9.62 + 0.19E.

Chapter 3 will detail the process of observing the methanol maser source G9.62 + 0.19E,

using the 30-m radio telescope at the Warkworth Radio Astronomy Observatory. The steps undertaken include conducting the observation, processing the raw data, as well as importing the data into MATLAB for formatting and baseline fluctuation removal. The goal at the end of the process is to have a smoothed spectrum containing the main features of G9.62 + 0.19E, that can be fit with multiple Gaussians for analysis.

In Chapter 4, the results of fitting multiple Gaussians will be presented; as well as a parameter estimate for the optical depth value of the maser source G9.62 + 0.19E. Error calculations will be provided for the Gaussian parameter coefficients and the optical depth estimation.

These results, as well as the theoretical modelling and observation processes, will be discussed in Chapter 5. Here, recommendations for the improvement, and continuation, of the presented work will be made.

Finally, a summary of the key findings and insights made through the completion of this thesis will be provided in Chapter 6.

Chapter 2

Theory

The modelling of masers is a necessary process, as it validates the utilization of masers as sensitive tracers of various other celestial entities (such as young stellar objects, late-type stars, and active galactic nuclei). Beyond their use as indicators, masers serve as tools for facilitating the examination of celestial kinematics, the measurement of diverse physical parameters, direct distance measurements, and investigations into the structure of our Galaxy. Moreover, maser modelling enables the exploration of masers as a distinctive phenomenon in their own right (Sobolev & Gray, 2012).

Within this chapter, standard maser theory from existing literature is reviewed and adapted to serve the purpose of modelling observed maser data. The objective is to apply this theoretical framework toward extracting insights into the physical characteristics of the maser source G9.62 + 0.19E. Through the application of specific assumptions regarding the maser source, approximations are made using the standard maser theory, enabling an analytical (non-numerical) solution to the radiative transfer equation. Through the non-numerical solution, we can generate a theoretical maser spectrum that can then be used to test an appropriate modelling framework. This model will then be applied to the main feature of the observed spectrum from methanol maser G9.62 + 0.19E.

Three different published explanations of standard maser theory will be presented. The fundamentals of standard maser theory remain consistent between publications, with the main difference between the works being the treatment of "semi-classical" theory. Gray (2012) describes the domain of maser theory as containing a "hierarchy of approximations" (Gray, 2012) when explaining the interaction between radiation and matter. Different levels of approximation trade a degree of accuracy of the representation for the ease of use and simplicity of analysis (Gray, 2012). The most accurate representation of the interaction between radiation and matter is the fully quantum-mechanical model. This model describes an ensemble of active molecules, that together with a radiation field of a countable number of photons, forms a combined quantum state.

Standard maser theory is used in two earlier works by Litvak (1970) and Trung (2009). They deal with the assumption of a two-level system in a one-dimensional case. Semi-classical theory occupies a middle ground between standard maser theory and the fully quantum mechanical model. In this approach, the molecular response is treated quantum mechanically, while the radiation field is represented using Maxwell's equations (Gray, 2012). To align with the thesis scope, all equations referenced or utilized in modelling the observational data will be derived from classic maser equations.

The three works that will be reviewed in this chapter: "Linewidths of a Gaussian Broadband Signal in a Saturated Two-Level System" (Litvak, 1970), "On the theory of astronomical masers – I. Statistics of maser radiation" (Trung, 2009), and "Maser Sources in Astrophysics" (Gray, 2012). All three deal with the modelling of maser radiation using the radiative transfer equation in some capacity. Though the means of deriving the maser equations varies between publications, the end results are comparable forms of the formulation. Upon examining all three works, the assumptions and adjustments applied to the presented theories for modelling the maser observations in this study will be explained.

2.1 M. M. Litvak (1970)

Litvak derives the spectral power distribution of a broadband maser signal that is saturating a two-level system (Litvak, 1970). The analysis uses stationary Gaussian statistics for the electric fields, as well as the assumption that the bandwidth is significantly larger than the homogeneous linewidths of the two levels. The findings are then applied to traveling-wave amplifiers of this kind, specifically focusing on cosmic OH and H_2O masers. The main purpose being to determine the intensity and linewidth of the saturated maser output with respect to the length of the amplifier.

The main body of the paper lays out the derivations for the spectral power distributions for six cases of maser emission (A-F). These cases are distinguished by whether the line broadening is homogeneous or inhomogeneous, whether the signal is narrow or broadband, and whether the saturation is moderate or extreme (Litvak, 1970).

Before moving into the individual cases, Litvak begins by defining the equations of motion for the two-level (*i* and *j*) density matrix. Gaussian and stationary statistics are used to define the conditions of the electric field within the equations of motion (Litvak, 1970).

Out of the six cases, case E is of particular interest. The characteristics that define case E are inhomogeneous broadening, a broadband signal, and moderate saturation. Litvak models the saturated maser output intensity and linewidth as functions of amplifier length using case E to represent a steady traveling-wave broadband maser amplifier. The increase of maser intensity $I(r, \nu)$ with distance r, assuming propagation only along this direction, is equated to the power generated at frequency ν for case E (Litvak, 1970). [1]

[1] All equations have been given in notations that are consistent with what has already been defined within this thesis - the original notations of Litvak vary slightly from what is presented here.

$$\frac{dI(r,\nu)}{dr} = \beta(r,\nu)I(r,\nu) + \gamma(r,\nu) \tag{2.1}$$

where $\beta(r,\nu)$ is the gain coefficient, and $\gamma(r,\nu)$ is the power generated per unit volume due to spontaneous emission. The term for spontaneous emission is excluded hereafter. Litvak states that the amplifier will be considered to act on a weak input intensity $I_0(\nu)$ at $r = 0$. Therefore, the results are predicted to not differ substantially whether $I_0(\nu)$ has a very flat spectrum or a width equal to the Doppler width $\beta(0,\nu)$. The inclusion of spontaneous emission $\gamma(r,\nu)$ would likely not alter the results significantly, since it is usually a weak source of broadening comparable to that of the gain coefficient $\beta(r,\nu)$ for cosmic masers (Litvak, 1970).

The author then takes the intensity $I(r,\nu)$ at a position along the propagation path r, at frequency ν (measured with respect to the reference line-center frequency ν_{ij}) and characterizes it by an approximately Gaussian profile. The Gaussian profile represents amplitude and bandwidth as functions solely dependent on r (Litvak, 1970).

$$I(r,\nu) \simeq I(r)e^{\frac{-\nu^2}{\Delta\nu(r)^2}} \tag{2.2}$$

The emission coefficient is set to equal the increase of intensity with distance.

$$\frac{dI(r,\nu)}{\beta_c(\nu)dr} \simeq I(r,\nu)\frac{e^{\frac{-\nu^2}{\delta\nu_D^2}}}{1+\frac{I(r,\nu)}{I_s}} \tag{2.3}$$

Here, $\beta_c(\nu)$ is the line centre of the unsaturated gain coefficient $\beta_0(\nu)$, $\delta\nu_D$ is the Doppler half-width, and I_s is the saturation parameter (Litvak, 1970). A similar equation is derived by Trung (2009).

2.2 D. V. Trung (2009)

In this work, Trung re-evaluates the amplification process of broad-band radiation by one-dimensional astronomical masers (Trung, 2009). By deriving core equations and comparing them to established radiative transfer principles, the paper explores the foundational assumptions of current maser theory. Through simulations, Trung investigates the amplification of diverse radiation scenarios, revealing deviations from Gaussian statistics even under partial saturation. Interaction between frequency modes and population pumping gains importance as saturation nears. While standard radiative transfer holds for unsaturated and partially saturated masers, caution is advised for strong saturation scenarios (Trung, 2009).

The introductory section describes the similarity between astronomical masers and laboratory lasers, which are both sources of radiation produced by stimulated emission. The author continues to explain that it has been speculated that maser radiation might not follow Gaussian patterns and that past attempts to measure non-Gaussian statistics have yielded negative results (Evans et al., 1972; Moran, 1981). Early recognition of the broad-band nature of maser radiation led to the introduction of two significant assumptions when deriving transfer equations: the stationarity of the field and the Gaussian distribution of electric field components (Litvak, 1970; Goldreich, Keeley, and Kwan, 1973). These assumptions simplify equation derivation, but their validity, especially in saturation conditions, remains largely unexplored (Trung, 2009).

The study by Menegozzi and Lamb (1978) develops a physical model describing the amplification of broad-band radiation by a one-dimensional maser. Trung notes that their findings suggest that as radiation is amplified, Gaussian statistics cannot be maintained, impacting the maser's population inversion. However, due to limited computing power, they could simulate only a handful of realizations of the radiation field. Therefore, in

this paper, Trung intends to use the formulation worked out by Menegozzi and Lamb (1978) to study in detail the astronomical maser and simulate from first principles the amplification of the broad-band background radiation field by the maser (Trung, 2009).

Trung begins exploring the basic theory by defining the statistical properties of the radiation field. The continuum radiation is described as the superposition of waves coming from many small, independent sources propagating along the z-axis, arriving at the boundary of the masing medium. It is, therefore, defined as a random function of time. It is assumed that the incident radiation field is stationary and that the underlying probability distribution of the random variable $E(t)$ at any instant of time is described by a Gaussian with zero mean and variance $\langle |E(t)|^2 \rangle = \sigma^2$ (Trung, 2009).

Trung then goes on to derive equations relating the transfer of the radiation field to the density matrix of masing molecules. The basic equations are defined for the idealized case of a scalar one-dimensional maser. Meaning the masing molecules are represented as a system with only two energy levels (upper i and lower j) and the properties of the maser depend only on the z coordinate, which is the propagation axis of the maser radiation (Trung, 2009).

To solve the matter-radiation interaction equations, the perturbative expansion consisting of solving the equations through a series expansion is used. Here, to first order, the populations are considered constant over time within a given realization. By taking the ensemble average of the equations, the standard radiative transfer equation for the average intensity of maser emission is recovered. This is possible given the postulation that the maser medium is in a steady state with fluctuations of the population inversion being independent of that of the average intensity $I(\omega)$.

It is noted that although population inversion is driven by the radiation field, Goldreich et al. (1973) propose that under small signal conditions, population inversion fluctuations

are minute with a narrow bandwidth, or the autocorrelation time is substantially longer than that of the radiation field. This rationale supports the assumption disregarding population inversion fluctuations relative to those of the radiation field (Trung, 2009). Following this, the standard equation describing the ensemble average intensity $\langle I(\omega)\rangle$ for the maser is obtained: [2]

$$\frac{d\langle I(\omega)\rangle}{d(r/L)} = \langle I(\omega)\rangle \frac{\tau_0(\nu)}{1 + \frac{3B/2\pi\Gamma}{\langle I(\omega)\rangle}} \tag{2.4}$$

Here, the ensemble average intensity $\langle I(\omega_n)\rangle$ is given in terms of angular frequency ω, where $\omega = 2\pi\nu$. The value r represents the propagation path of the radiation along the z-axis, and L is the length of the maser.

The optical depth for an unsaturated maser, $\tau_0(\nu)$ is given as follows:

$$\tau_0(\nu) = \left(\frac{h\nu}{4\pi} \cdot 3B \cdot \frac{c}{\nu}\right) L \frac{\Delta\lambda(\nu)}{\Gamma} \tag{2.5}$$

Where h is the Planck constant, B is the combined Einstein coefficient for stimulated emission (B_{ij}) and absorption (B_{ji}), c is the speed of light, and $\lambda(\nu)$ and Γ are the pumping and loss rates, respectively, for the upper and lower levels.

The rest of the paper deals with characterizing the deviation of the radiation field from Gaussian statistics, and simulations of radiation transport according to the formulations of Menegozzi and Lamb (1978). The simulations are conducted within the partially saturated regime, a scenario likely to be relevant for the majority of astronomical masers (Trung, 2009).

In the discussion, Trung reports that the comparison of the ensemble averaged intensity

[2] All equations have been given in notations that are consistent with what has already been defined within this thesis - the original notations of Trung vary slightly from what is presented here.

of the total electric field (taken over 18,000 realizations of the field) within the simulation closely matches that of the prediction of the standard radiative transfer equation (2.4). Thus, the conclusion is drawn that in the unsaturated and partially saturated regime, the classic theory of astronomical masers produces results in good agreement with that of the more realistic treatment of the simulations. However, in saturated masers where the radiation field deviates further from Gaussian statistics, the classic maser equations (Litvak, 1970) are no longer valid. Also worth mentioning is Trung's observation that a fully saturated maser is of purely theoretical interest. In actuality, the existence of such highly saturated masers in the real astronomical context is improbable, given several constraints including the pumping of masers (Trung, 2009).

2.3 M. D. Gray (2012)

This source is the most recently published, and only book among the three works. "Maser Sources in Astrophysics" (Gray, 2012) is a survey of the theory and observations of astrophysical masers sources and their use as astronomical tools. The book summarizes the history of the discovery of multiple maser molecules and lines. It also discusses maser observations on various scales. Both semi-classical and standard theories are discussed in detail. Models of the quantum-mechanical response of the molecules are included and linked to more general equations of radiative transfer. In later chapters, the radiation statistics of astrophysical masers and numerical methods of analysis are also discussed (Gray, 2012).

Chapter 3 of the book deals with the standard theory of masers and is what will be reviewed here (Gray, 2012, Chapter 3). Gray begins the chapter by dividing the theory of astrophysical maser into two interconnected problems: that of the transfer of radiation through the maser medium containing the active molecules, and that of the molecular

physics needed to calculate the population inversion. The population inversion is calculated locally at a position in space, dependent on the physical conditions of that point. However, these physical conditions are linked with the radiation field which relates to the non-local transfer of radiation. The problem of radiative transfer requires the populations of the molecular energy levels to be known across all points along the path of propagation, which means the molecular physics must also be taken into account along the ray (Gray, 2012).

As explained in Section 1.2.1, the processes responsible for the population inversion of masers are classified under non-local thermodynamic equilibrium (Non-LTE) physics. For gases that are not in LTE, the populations of energy levels cannot be described by Boltzmann's formula (1.6). Here it is assumed that the collisions are sufficient enough to maintain a Maxwell-Boltzmann distribution of molecular speeds, as well as that the molecular populations can be represented by a set of kinetic master equations (rate equations). Within these kinetic equations, it is said that in a steady state, the net population flow into any energy level from all others is zero (Gray, 2012). Thus, if a molecule has N available energy levels, where the population in the ith level is ρ_i, then the kinetic equation for the level can be given as: [3]

$$\rho_i \sum_{j=1, j\neq i}^{N} k_{ij} - \sum_{j=1, j\neq i}^{N} \rho_i k_{ji} = 0 \tag{2.6}$$

In the case of an equivalent two-level system, the transition ij represents a single transition between the upper and lower levels i and j. k_{ij} is an all-process rate coefficient for the transfer of population from level i to j.

The individual processes that contribute to k_{ij} are the physical means by which the population is transferred between levels i and j. For molecules in astronomical maser

[3] All equations have been given in notations that are consistent with what has already been defined within this thesis - the original notations of Gray vary slightly from what is presented here.

mediums, the processes can be described by the emission and absorption of radiation, alongside the collisions between neighbouring molecules of the same kind (Gray, 2012).

The downward population transfer is given by:

$$k_{ij} = A_{ij} + B_{ij}\bar{J}_{ij} + C_{ij} \tag{2.7}$$

where A_{ij} is the spontaneous emission rate, $B_{ij}\bar{J}_{ij}$ is the rate of stimulated emission. $\bar{J}_{ij}$ is the mean intensity, a solid angle average of the frequency-dependent specific intensity I_ν. There is also C_{ij}, the rate of collisional de-excitation.

The upward transitions have no spontaneous component, so the equation is written as:

$$k_{ij} = B_{ij}\bar{J}_{ij} + C_{ij} \tag{2.8}$$

The following relations for the Einstein B-coefficients (B_{ji}, B_{ij}) and collisional terms (C_{ji}, C_{ij}) are also given:

$$B_{ji} = \frac{g_i B_{ij}}{g_j} \tag{2.9}$$

$$C_{ji} = \frac{g_i}{g_j} C_{ij} e^{-\frac{h\nu_{0,ij}}{kT_k}} \tag{2.10}$$

where k is the Boltzmann constant, T_k is the kinetic temperature, and g_i and g_j are the statistical weights (degeneracies) of the levels (1.2.1).

The population inversion is then able to be described in terms of the statistical weights and mean intensity.

$$\Delta\rho_{ij} = \frac{\rho_i}{g_i} - \frac{\rho_j}{g_j} \tag{2.11}$$

$$\Delta\rho_{ij} = \frac{\Delta\rho_0}{1 + \bar{J}_{ij}/J_s} \tag{2.12}$$

In (2.12), $\Delta\rho_0$ is the inversion in the absence of maser radiation (when $\bar{J}_{ij} = 0$) and J_s is the saturation intensity. The saturation intensity is defined as the mean intensity of radiation that will reduce the inversion to half of its unsaturated value ($\bar{J}_{ij} = 0$). Here it should be noted that $\Delta\rho_{ij} \approx \Delta\rho_0$ when $\bar{J}_{ij} << J_s$

This equation for the inversion with average intensity in the denominator demonstrates that as the maser intensity increases, the population inversion decreases.

$$\bar{J}_{ij}/J_s = I_s \tag{2.13}$$

The ratio (2.13) is a measure of the saturation in terms of average intensity compared to the intensity at which the inversion is halved.

From here, the standard maser equations can be constructed using the equation of radiative transfer. The following definitions for the absorption $\alpha_{\nu,ij}$ and emission $\epsilon_{\nu,ij}$ coefficients are given for the transition ij:

$$\alpha_{\nu,ij} = \left(\frac{h\nu_{0,ij}}{4\pi}\right)[\rho_j B_{ji} - \rho_i B_{ij}]\phi_{\nu,ij} \tag{2.14}$$

$$\epsilon_{\nu,ij} = \left(\frac{h\nu_{0,ij}}{4\pi}\right)\rho_i A_{ij}\phi_{\nu,ij} \tag{2.15}$$

$\nu_{0,ij}$ is the rest frequency and $\phi_{\nu,ij}$ is the normalized lineshape function. $\phi_{\nu,ij}$ is given

by converting the Maxwell-Boltzmann distribution of particle velocities to a lineshape function in frequency via Doppler's formula.

Maxwell-Boltzmann distribution:

$$f(v) = \left(\frac{m}{2\pi k T_k}\right)^{3/2} e^{\frac{-m(v-\bar{v})^2}{2kT_k}} \tag{2.16}$$

Normalized lineshape function:

$$\phi_\nu = \left(\frac{mc^2}{2\pi\nu_0^2 k T_k}\right)^{1/2} e^{\frac{-mc^2(\nu-\nu_0)^2}{2\nu_0^2 kT_k}} \tag{2.17}$$

where m is the mass of a single molecule of the masing species, T_k is the kinetic temperature of the gas.

To simplify (2.17), frequency is denoted by variable u, a measure of the width of the lineshape:

$$u^2 = \frac{2\nu_0^2 kT_k}{(mc^2)} \tag{2.18}$$

with the substitution of u, (2.17) becomes:

$$\phi_\nu = (\pi^{1/2}u)^{-1} e^{-(\nu-\nu_0)^2/u^2} \tag{2.19}$$

The line transfer equation of maser radiation along the propagation path r is given by:

$$\frac{dI_\nu}{dr} = -\alpha_\nu(r) I_\nu(r) + \epsilon_\nu(r) \tag{2.20}$$

The assumption is then made that the term for spontaneous emission can be ignored,

and that the emission coefficient (ϵ_ν) can be excluded. The radiative transfer equation then looks like this:

$$\frac{dI_\nu(r)}{dr} = \beta_\nu(r) I_\nu(r) \tag{2.21}$$

where $\beta_\nu = -\alpha_\nu$ is the gain coefficient, which can be written as:

$$\beta_\nu = \frac{h\nu_0 B_{ij} g_i \phi_\nu}{4\pi} \frac{\Delta\rho_0}{1 + \bar{J}/J_s} \tag{2.22}$$

By substituting the simplified lineshape function (2.19), the maser equation (2.22) can be reduced to:

$$\frac{dI_\nu}{dr} = I_\nu \frac{\beta_0(r) e^{-(\nu-\nu_0)^2/u^2}}{1 + \bar{J}/J_s} \tag{2.23}$$

Following Litvak (1970), Trung (2009), and Gray (2012), we rewrite (2.23) as:

$$\frac{dI_\nu}{dr} = I_\nu \frac{\beta_0(r)\phi_\nu(r)}{1 + I_s} \tag{2.24}$$

where ϕ_ν is a form of Gaussian, $\beta_0(r)$ is the gain coefficient of the line center (where $\beta_0 = -\alpha_0$), and I_s is a term that represents the saturation state of the maser (2.13). Here, I_s is taken as a value between 0 and 1 that expresses the degree of saturation from unsaturated (0%) to fully saturated (100%).

As previously explained, the version of the radiative transfer equation used in the standard theory of masers is only applicable in the case of unsaturated and moderately saturated masers (Trung, 2009).

2.4 Solution to the Equation of radiative transfer

2.4.1 Low Saturation Maser

In this section, we investigate the standard maser theory in the case of a maser with very low saturation.

This concept was explored in the work of Goldreich and Keeley (1972), where the relation between the apparent and actual sizes of maser sources is investigated for models of homogeneous maser clouds of spherical and cylindrical geometries (Goldreich & Keeley, 1972). Here, the treatment of maser radiation uses the ordinary equation of transfer, and approximate analytic calculations are given for all degrees of saturation.

Starting from equation (2.24), by assuming that the maser is lowly saturated, it allows for the assumption that the term I_s is much less than 1 (Goldreich & Keeley, 1972; Watson, Sarma & Singleton, 2002). By incorporating these assumptions, the form of the standard maser equation is simplified even further to:

$$\frac{dI_\nu}{dr} = I_\nu \beta_0(r) \phi_\nu \tag{2.25}$$

where $\beta_0(r)$ is the gain coefficient (negative absorption coefficient) of the line center.

Further, dividing both sides of (2.25) by $\beta_0(r)$ and denoting $\beta_0(r)dr \equiv d\tau_0(r)$ gives

$$\frac{dI_\nu}{d\tau_0} = I_\nu \phi_\nu \tag{2.26}$$

where τ_0 is the optical depth of the line center.

Referring back to the equation of radiative transfer (1.12),

$$\frac{dI_\nu}{dr} = -\alpha_\nu I_\nu + \epsilon_\nu \tag{2.27}$$

optical depth is introduced through the following relation:

$$\tau_\nu = \alpha_\nu dr$$

It is noted that when using β_ν in lieu of the absorption coefficient α_ν, the physical sense of the optical depth changes from the measure of weakening radiation propagating through the light absorbing media, to a measure of the amplification of radiation in an "active" media.

In the case of absorbing media, the optical depth is determined by the sum of the optical depth of the continuum plus the optical depth of the spectral line. In the case of active media, the transition between discrete levels overwhelmingly dominates over the mechanisms of continuum radiation in gaseous media, so the latter can be neglected. Therefore, equation (2.26) contains the gain coefficient belonging to the spectral line alone.

Equation (2.25) is rewritten as

$$\frac{dI_\nu(r)}{I_\nu(r)} = \beta_0(r)\phi_\nu dr$$

Taking the integral of both sides gives the following:

$$\ln I_\nu = \int_0^R \beta_0(r)\phi_\nu dr + constant$$

The intensity of radiation is therefore

$$I_\nu(\tau) = I_\nu^0 e^{\int_0^R \beta_0(r)\phi_\nu dr} \tag{2.28}$$

The obtained equation of radiative transfer is valid for a "pencil" model where radiation propagates through a narrow cylinder (pencil). I_ν^0 is the incoming radiation intensity at the optical depth $\tau = 0$, and $r = 0$. $I_\nu(R)$ is the intensity that leaves the pencil at the optical depth τ, and $r = R$.

Figure 2.1: A "pencil" model used in the equation of radiative transfer.

2.4.2 Spherical Model of the Maser Source

The analysis is further limited by considering the case of a spherical masing molecular cloud.

Here, it is noted that the definition of "spherical" and "cylindrical" models differs between this work and that of Goldreich and Keeley (1972). The authors describe their spherical model as being a sequence of homogeneous, spherical masers of increasing radius; and the cylindrical model as a sequence of homogeneous, cylindrical masers of increasing length, and fixed cross-sectional area (Goldreich & Keeley, 1972). In this thesis, the spherical model being considered is one consisting of a globular cloud consisting of thin "pencil" sections of cylindrical pathing. Therefore, the spherical model presented in this work is closer to a combination of both geometries investigated by Goldreich and Keeley (1972).

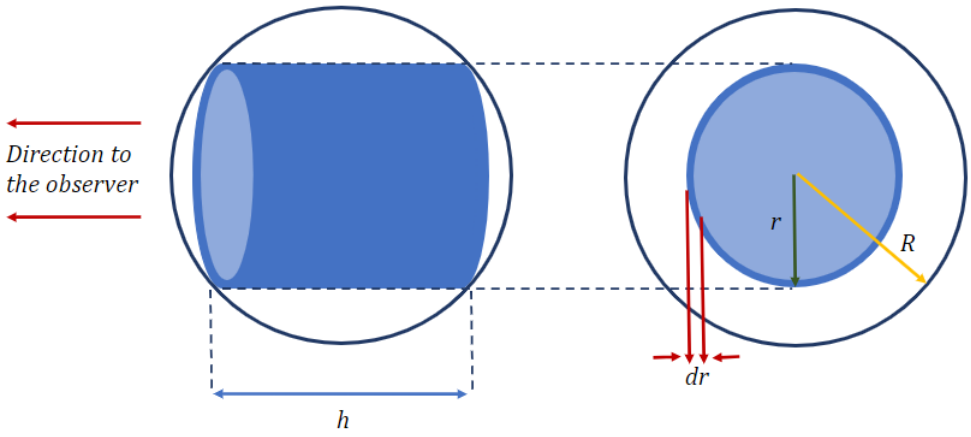

Figure 2.2: Model of the hypothetical cylindrical pathing of maser radiation through a globular cloud.

Figure 2.2 shows the masing sphere from two perspectives. In practice, it should be taken into consideration that this is a simple model that does not take into account radiation scattering.

The sphere can be considered as a collection of independent "pencils" of differing lengths, h, and corresponding optical depths, τ.

A cylinder at the distance r from the center of the sphere is considered. The lengths of the "pencils" that construct this cylinder are:

$$h_r = 2\sqrt{R^2 - r^2} \tag{2.29}$$

Using Pythagoras' theorem,

$$h_r = 2R\left(1 - \left(\frac{r}{R}\right)^2\right)^{\frac{1}{2}}$$

The area of a cylinder, at the distance r from the center, is given by

$$A_r = 2\pi r dr \tag{2.30}$$

The intensity of the radiation in relation to the area of the cylinder is proportional to the area A_r:

$$I_r \propto A_r e^{-\tau_r} \tag{2.31}$$

where

$$A_r e^{-\tau_r} = A_r e^{\beta_0 \phi_\nu h_r}$$

and

$$I_r \propto r\, dr\, e^{\beta_0 \phi_\nu (1-(\frac{r}{R})^2)^{\frac{1}{2}}}$$

Therefore, integration over $0 \leq r \leq R$ gives the total (integrated) intensity:

$$I_\nu \propto \int_0^R I_r = \int_0^R r e^{\beta_0 \phi_\nu (1-(\frac{r}{R})^2)^{\frac{1}{2}}} dr$$

Substituting in the following terms $x = \frac{r}{R}$ and $\phi_\nu \propto e^{-\Delta\nu^2}$ gives

$$I_\nu = \int_0^1 x e^{\beta_0 (1-x^2)^{\frac{1}{2}} e^{-\Delta\nu^2}} dx$$

Here, $\Delta\nu$ is given in Doppler widths.

Using a numerical integration approach, the above integral is presented as the sum of i

terms for x

$$I_\nu = \sum_i x_i e^{\beta_0 (1-x_i^2)^{\frac{1}{2}} e^{-\Delta\nu^2}} \tag{2.32}$$

2.4.3 Theoretical Model Implementation

Using MATLAB, the theoretical model presented in (2.32) can be programmed and visualized. MATLAB (**MAT**rix **LAB**oratory) is a programming language and environment developed by MathWorks, designed for numerical computing and data analysis. It provides a comprehensive set of tools and functions for a wide range of scientific and engineering applications (MathWorks, 2023).

The MATLAB code generates a spectrum using the theoretical model in (2.32), representing the sum of a specified number of cylindrical pencil sections of a spherical radiation source. Initially, it defines frequencies in Doppler widths (**Nu**) and generates a weight parameter (**w**) using the relative radius of the globule (**R**). The vector (**Nu**) contains 501 values within the interval $-2.5 \rightarrow 2.5$. The relative radius of the globule is given as a vector of values between 0 and 1 at (**n**) intervals. Here, (**n**) represents the number of integration steps, and is arbitrarily defined as 101. The weight parameter (**w**) is derived from Pythagoras' theorem as being $w = \sqrt{1 - R^2}$. A Gaussian parameter (**Gs**) is also defined in terms of the Doppler widths (**Nu**) as $Gs = e^{-Nu^2}$.

The code then iterates through a range of optical depths (**tau**) and calculates spectral intensities (**I**) by summing up weighted Gaussian functions. The range given for the optical depths (**tau**) is from $1 \rightarrow 20$. The range of optical depth values stems from relevant literature sources detailing specific optical depth measurements associated with methanol masers; Syzmczak et al. (2017) and Nesterenok (2016).

Szymczak et al. (2017) present a comprehensive study on the variability and behavior

of 6.7 GHz methanol masers across 139 star-forming sites, observed over a period from June 2009 to February 2013 using the Torun 32-meter radio telescope. While G9.62 + 0.19E is not included among the masers documented in this paper, optical depth values are estimated for the similarly highly variable source, G24.329 + 0.144. In the discussion on the causes of the variability, observations of G24.329 + 0.144 maser components are specifically mentioned, as they reveal significant changes in brightness temperature during flares. The increase in brightness temperature from $10^7 \rightarrow 2 \times 10^9$ K corresponds to a notable rise in optical depth, suggesting unsaturated amplification. The anti-correlation observed between intensity and line width aligns with the expected behavior for unsaturated amplification, as per theoretical predictions (Goldreich & Kwan, 1974). By estimating the background radiation contribution, and adopting continuum emission data, the derived optical depth of $\tau = 13.4$ during the quiescence phase increases to $\tau \approx 17.4$ at the flare maximum (Szymczak et al., 2017).

Nesterenok (2016) explores a one-dimensional model of methanol masers, employing two methods to calculate molecule level populations: the accelerated lambda iteration (ALI) method and the large velocity gradient (LVG) approximation. Additionally, the paper delves into the factors influencing the pumping of class I and class II methanol masers. In the section discussing the results of calculating the methanol level populations using the ALI method, maser gain dependencies on gas temperature and the external dust layer are examined. The author discusses the competitive nature of collisional and radiative pumping mechanisms, supporting the coexistence of different maser types within the same maser region. Here, the conditions required for robust maser lines are discussed, estimating the saturation point for methanol masers to occur at optical depths approximately between $15 \rightarrow 20$ (Nesterenok, 2016).

In a later publication, Nesterenok (2022), calculations of the optical depth in maser transitions of methanol and hydroxyl for a grid of C-type shock models are presented.

Here, the optical depth at which widespread methanol masers become saturated is given as being between τ = 12 and τ = 15. The methanol maser transition $5_1 - 6_0$ (corresponding to 6.7 GHz) is not included in this paper, however, the optical depth values provided for multiple other methanol emissions are on the scale of $10^{-2} \leq \tau \leq 10^{1}$ (Nesterenok, 2022).

Taking into account these sources, the upper limit for the optical depth input (**tau**) was set at τ = 20, and the lower limit at τ = 1. The rationale is that this range of values would provide enough variation in the line shape to observe the effect of different optical depths on the theoretical model.

For each value of optical depth ($1 \rightarrow 20$), the code produces a theoretical spectral line with intensity (**I**) equal to the sum of (**n**) weighted Gaussian terms.

2.4.3.1 Gaussian Approximations

The generated theoretical spectra are then used to find an appropriate model to emulate the maser spectral shape. Since the theoretical spectra are comprised of the sum of weighted Gaussians, it can be presumed that a simple way to fit the model would be to use Gaussians. The use of Gaussians to approximate spectral line profiles of masers has been documented in publications such as Watson et al. (2002) and Nesterenok (2016).

As previously introduced, Nesterenok (2016) deals with the calculation of molecular level populations of a one-dimensional model for methanol masers. Class II methanol masers at 6.7 and 12.2 GHz were extensively studied using VLBI, particularly focusing on observations towards the ultracompact HII region W3(OH). The maser emission is observed as distinct maser spots, varying in size from $1 \rightarrow 7$ astronomical units (au) with a mean size of 3 au. Spectra of these maser spots are well described by single Gaussian profiles, featuring Full Width at Half Maximum (FWHM) line widths typically ranging from $0.1 \rightarrow 0.3$ km/s. Analysis suggests these 12 GHz masers in W3(OH) are

unsaturated, showing significant narrowing compared to the emission coefficient line profile (narrowing by a factor of approximately $3 \rightarrow 4$) (Nesterenok, 2016).

A similar use of single Gaussian profiles is documented in Watson et al. (2002). This paper investigates the spectral line profiles of linear masers, demonstrating the deviations from Gaussian shapes due to the amplification process. In particular, near-Gaussian profiles are observed in bright interstellar 22 GHz water masers obtained via high-resolution Very Long Baseline Array (VLBA) observations of W3 IRS 5. The authors propose that maser spectra closely resembling Gaussian profiles indicate these masers' origin in hot gas environments surpassing 1200 K, likely associated with C-type shocks. Additionally, they imply a modest level of saturation and narrow beaming angles, suggesting these profiles could serve as valuable diagnostics to understand astrophysical maser environments (Nesterenok, 2016).

The spectral line profiles of astrophysical masers change their width as they move towards saturation: initially narrowing with increasing intensity and then broadening upon reaching saturation. When masers are highly saturated, their Doppler velocity profiles closely resemble the Gaussian (Maxwellian) velocity distribution of the molecules causing the maser effect. This behavior remains consistent whether masers are treated in a linear manner (Litvak, 1971) or considered as finite cross-sections like disks or spheres (Watson et al., 2002).

At lower intensities, where masers are unsaturated, Watson et al. (2002) indicate that spectral profiles may display insignificant deviations from the Gaussian shape. These deviations, alongside the width of the profile, offer essential insights into masers, particularly regarding the angle at which maser radiation is emitted - a critical factor for determining luminosity and energy density from observed radiative flux.

Observations made at low angular resolution may blend multiple spectral profiles due

to there being several masing components within the telescope beam. However, high-resolution observations with the VLBA reveal spectral profiles that closely resemble Gaussian shapes. These observed profiles likely represent the upper bounds of actual deviations seen in individual maser profiles (Watson et al., 2002).

In assessing the suitability of fitting the theoretical model using a single Gaussian function, the solution to the transfer equation (2.32) indicates the presence of a Gaussian within the exponential term of the intensity function. The Gaussian within the exponential, as opposed to the Gaussian on its own, produces a much sharper spectral peak. This means that compared to the theoretical maser spectrum, a singular Gaussian is likely to leave non-negligible residuals. Here, the possibility of fitting the model with the sum of more than one Gaussian is considered. This approach offers a comparably simple method for modelling the curve, allowing for more flexibility in fitting the wings and base of the spectrum while retaining the ability to replicate the high intensity of the peak.

This is implemented within the code during the iterative step for each optical depth. As the optical depths (**tau**) are cycled through, with the intensity (**I**) for each being calculated via the sum of (**n**) integration steps, Gaussian coefficients are also generated through the built-in MATLAB 'fit' function. Two separate Gaussian fits are done for the resultant intensity data of each optical depth. The first fits two Gaussians to the theoretical model, and the second fits the same data with three Gaussians. These fitted Gaussians are plotted against the data at every optical depth.

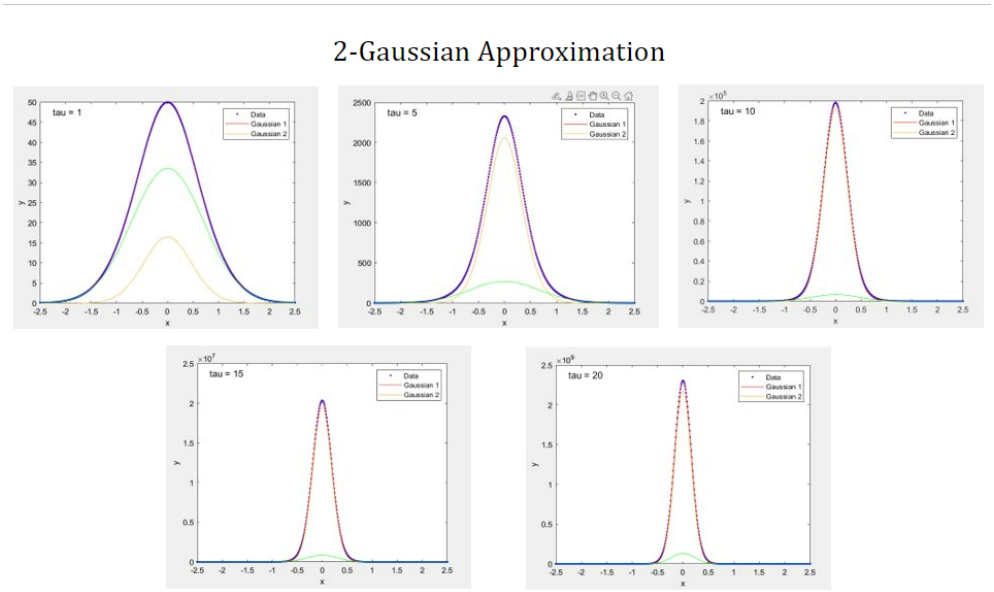

Figure 2.3: The spectra generated by the theoretical maser model MATLAB code for varying optical depths (1, 5, 10, 15, and 20), each spectrum fitted with two Gaussian curves.

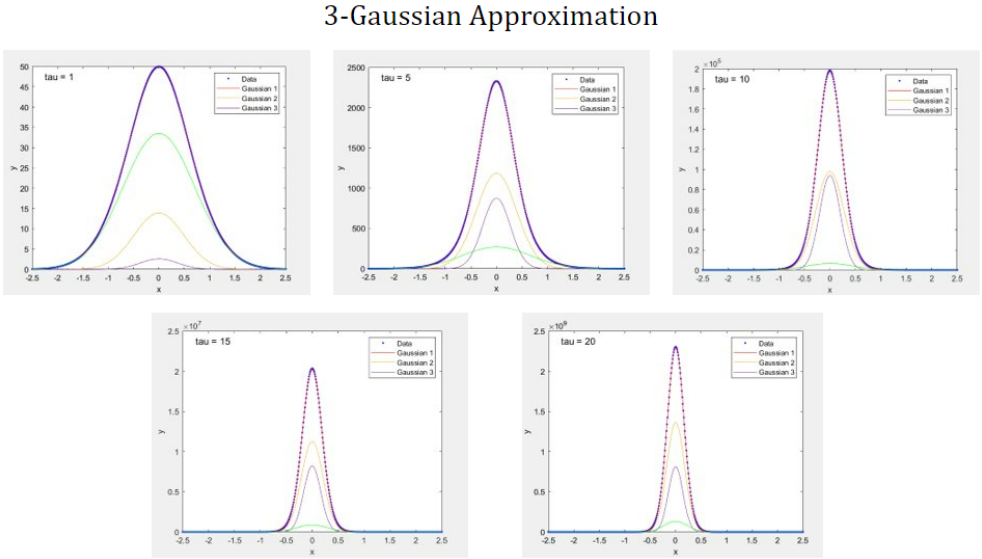

Figure 2.4: Graphs depicting the spectra from the theoretical maser model for optical depths 1, 5, 10, 15, and 20, each fitted with three Gaussian curves.

Here, it is seen that the natural best fit for the two Gaussian approximation is to have one narrow Gaussian with high amplitude and one wide Gaussian with low amplitude. For the three Gaussian approximation, two curves of similar amplitude and width are fit alongside the third low amplitude, wide Gaussian. The consistent appearance of the low amplitude, wide Gaussian across the range of optical depths indicates that it could be a potentially useful feature. In this work, this wide feature at the base of the spectrum will be referred to as the "pedestal" - a wide feature that sits beneath the high amplitude main feature, raising it above the baseline.

Subsequently, the code then computes and generates plots showing ratios between amplitudes and widths of the "pedestal" Gaussian to the overall sum of the Gaussians.

Additionally, it generates separate plots displaying the log amplitude and width of the fitted Gaussians against the optical depths, offering insights into the effect of optical depth on the Gaussian fits.

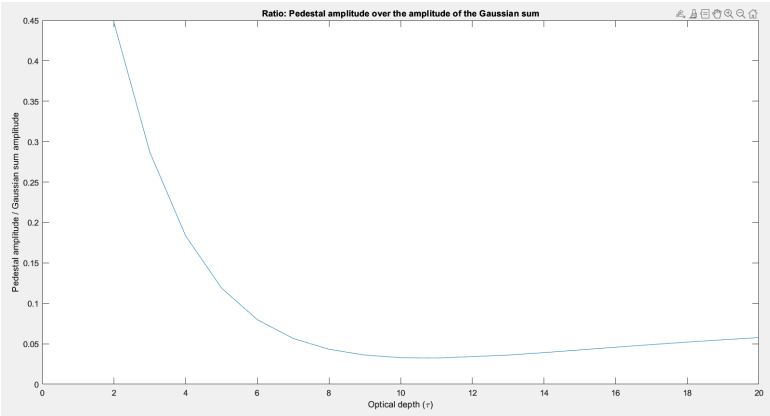

Figure 2.5: Graph showing the ratio of the pedestal amplitude to the amplitude of the sum of the Gaussians.

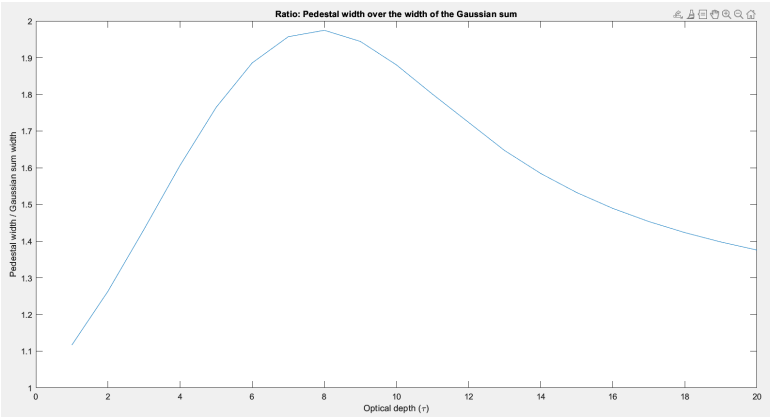

Figure 2.6: Graph showing the ratio of the pedestal width to the width of the summation of the Gaussians.

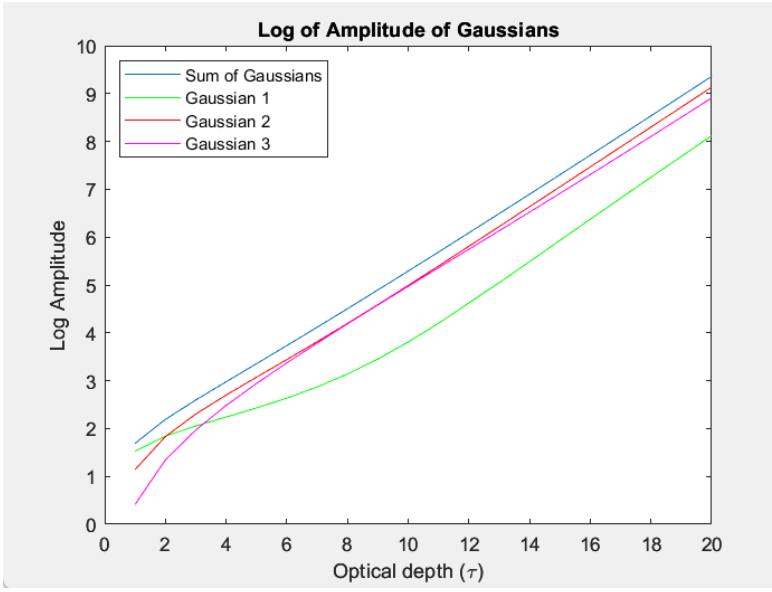

Figure 2.7: Plot of the log amplitudes of the fitted Gaussians against the corresponding optical depths for $\tau = 1 \rightarrow \tau = 20$.

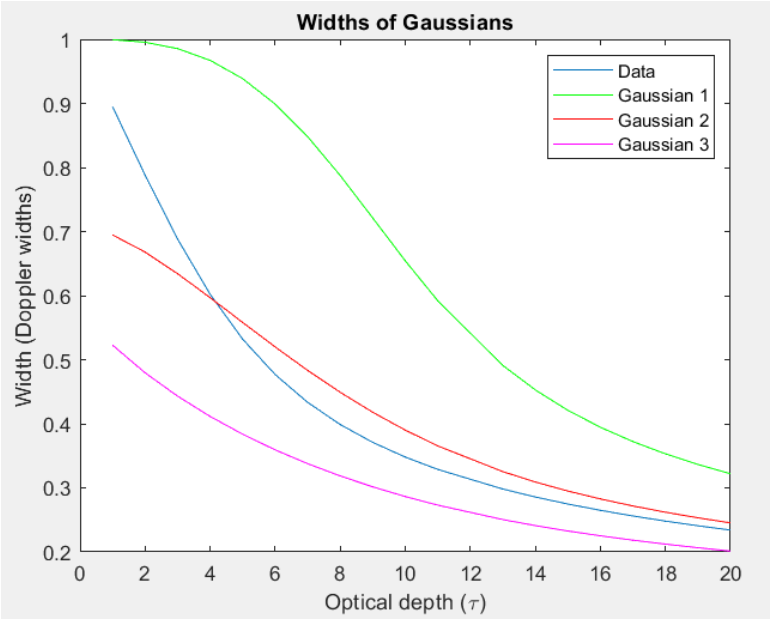

Figure 2.8: Plot of the Doppler widths of the fitted Gaussians against the respective optical depths for $\tau = 1 \rightarrow \tau = 20$.

The ratio of the amplitude, and width, of the pedestal to that of the overall sum of the Gaussians changes with different values of optical depth. The relationship is non-linear, which could be indicative of the characteristic narrowing and re-broadening of the spectrum as it approaches saturation. As previously mentioned, optical depths approximately > 12 are thought to coincide with a maser source that is mostly saturated (Nesterenok, 2016, 2022). According to this, we would predict that the width would approach the full Doppler width at optical depths within this range.

As such, there could be potential for the pedestal to be used as a tool for indicating the optical depth of the source, depending on its ratio to the sum of the Gaussian approximations. The appearance of the pedestal will be explored using observational data in Chapter 4.

Chapter 3

Observations and Data Processing

This chapter delineates the methodology, instrumentation, software, and analysis procedures employed for observing methanol maser G9.62 + 0.2E and processing the raw data. Section 3.1 describes the observation process undertaken, including details about the observational facilities, equipment, and operational software used. Section 3.2 will explain how the raw data was processed into the desired format for analysis. Finally, Section 3.3 will detail the multi-step process of data manipulation and analysis.

3.1 Observation Methodology

3.1.1 Warkworth Radio Astronomy Observatory

The maser observations conducted in this thesis were done using the facilities at the Warkworth Radio Astronomy Observatory (WRAO). At the time of the observation, the WRAO was operated by the Institute for Radio Astronomy and Space Research (IRASR) out of Auckland University of Technology (AUT). The WRAO has two major radio telescopes, the 12-meter fast slewing-shaped Cassegrain antenna, and the 30-meter Cassegrain antenna (an upgraded Telecom New Zealand telecommunication antenna,

operational since 2012).

Figure 3.1: Warkworth Radio Astronomy Observatory (WRAO). Photo / Dean Purcell / Getty Images.

The 30-m Warkworth 2 antenna was designed and constructed by Nippon Electric Corp (NEC) in July of 1984. Until its decommissioning, the Warkworth 2 antenna served as a means of satellite communication, facilitating a broad range of transmissions such as telephone calls, internet traffic, and television content in New Zealand (Institute for Radio Astronomy & Space Research (IRASR), 2022). In November 2010, AUT was formally granted a license to operate the Warkworth 2 antenna by Telecom New Zealand.

3.1.2 Warkworth 30-m Telescope

The Warkworth 30-m telescope is a Cassegrain wheel-on-track design with a 30.48-meter reflector and a Beam Waveguide feed. The dish itself has dimensions of 30.48 meters in diameter and 37 meters in height. Cassegrain telescopes are engineered so that the beam of radiation is focused via a primary concave mirror and a secondary convex mirror, such that the optical path folds back onto itself relative to the optical system's primary mirror entrance aperture. The large dish provides a greater surface

area for collecting radiation, meaning the accuracy at which low-strength radio waves can be observed is also higher.

Over its band of operation, the 30-m telescope has approximately six times greater collecting area and, therefore greater sensitivity than the 12-m antenna; it can provide (Institute for Radio Astronomy & Space Research (IRASR), 2022). The WRAO 30-m telescope can operate at both C-band (~ 5.8 → 6.8 GHz) and X-band (~ 8.1 → 9.1 GHz) frequencies. The telescope would be calibrated to record in the C-band to observe methanol masers that omit in the 6.7 GHz range.

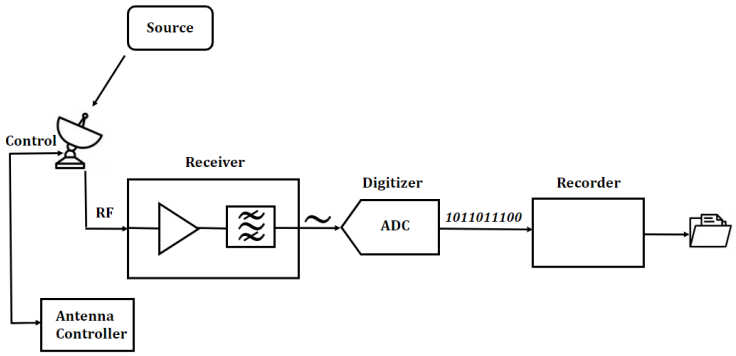

Figure 3.2: Generic layout of radio astronomy observation pipeline (Natusch, 2020).

The electromagnetic waves collected by the radio telescope are then processed by the receiver system. Often, radio telescopes use some type of superheterodyne receiver. A superheterodyne receiver is a type of radio receiver that uses frequency mixing to convert a received signal to a fixed intermediate frequency (IF) which can be more conveniently processed than the original carrier frequency. A frequency mixer is a non-linear element (diode) that combines an incoming radio frequency (RF) signal with a local oscillator (LO). The process is called heterodyning and involves taking two sinusoids (or cosinusoids) and multiplying them to produce a new signal with a new frequency at plus (high side injection) or minus (low side injection) the local oscillator (LO) frequency.

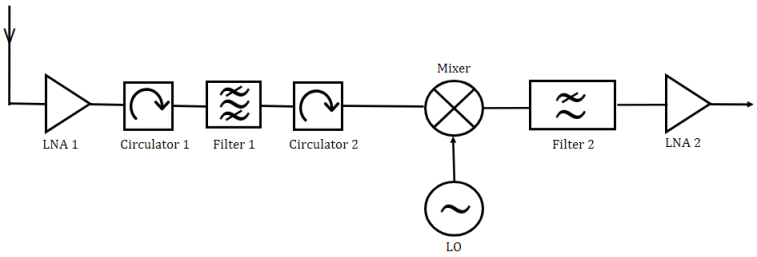

Figure 3.3: Generic components and layout of a superheterodyne receiver (Natusch, 2020).

The mixer is a key component of a superheterodyne receiver, as it is used to shift the incoming RF signal to a lower frequency that is both cheaper and easier to work with. Lower frequencies are favoured for their more achievable high levels of gain, and tendency to avoid stray coupling (unwanted voltage between components) (Natusch, 2020).

The superheterodyne receiver shown in Figure 3.3 uses a low-pass filter (Filter 2) that filters out the low-side injection frequency output of the mixer. The filtered low-pass frequency is the intermediate frequency (IF), which is then amplified via the low noise amplifier (LNA 2) before being processed. Once the data has been processed by the receiver, it is then digitalized where it can be appropriately formatted.

The digitizer machine at Warkworth is comprised of four digitizers, enabling it to ingest four separate streams of data. The 30-m telescope is sensitive to two types of polarizations, so measurements are recorded in two parts, the left-hand and right-hand circular polarizations. The digital base band converter (DBBC) allows for these two data streams to be digitized simultaneously, with the possibility of dual observations in another frequency band (i.e., X-band).

3.1.3 NASA Field System

The NASA field system (NSF) is a standardized computer-based interface used to communicate with the hardware of the radio telescope. The NSF is widely used by

the Very Long Baseline Interferometry (VLBI) community, as the commonality of the interface allows for participation in coordinated observations involving multiple telescopes. The observations conducted within this research only required the use of the single 30-m telescope, thus, no cross-coordination was necessary. However, the benefits of the NFS extend beyond its universality. Though the NSF appears visually and functionally antique, it facilitates many aspects of the observation process. The field system enables the user to "talk" to the telescope hardware through the execution of scripts.

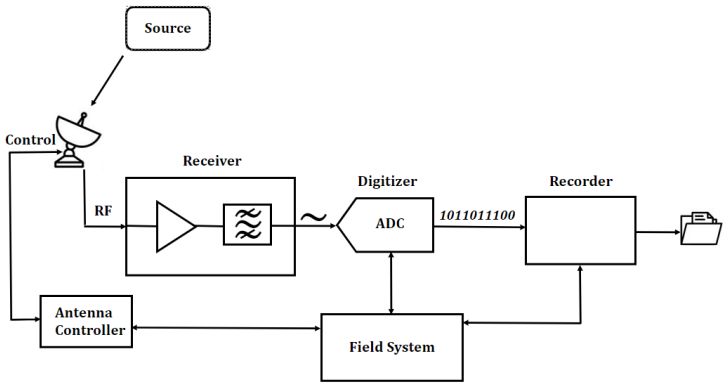

Figure 3.4: Radio astronomy observation pipeline in connection with the NASA Field System (Natusch, 2020).

These scripts are written in the control language of Standard Notation for Astronomical Procedures (SNAP) and are executed in a command line terminal via the Linux operating system (Himwich, 2000). SNAP scripts can be used to configure the hardware to the specifications required by a particular observation, command the telescope controller to slew to and track required celestial sources, trigger the recording of data at appropriate times, and log the operation of the system. Information that should be included in the SNAP file commands is the source name and epoch that you are referencing, as well as the right ascension and declination (RA and DEC) of the source. Other instructions include observation durations and periods between recordings (Himwich & Vandenberg, 2001).

The preparation of SNAP scripts is a multi-step process, completed using the National Radio Astronomy Observatory (NRAO) program SCHED (short for "Schedule"). SCHED is a program for planning and scheduling VLBI observations. Scheduling with SCHED involves creating an input file with a text editor, referred to as a ".key" file, which serves as the starting point for specifying what you want to observe and when. When the key file is run through SCHED, the program creates a variety of outputs in the form of VLBI Exchange Format (VEX) files that provide both summary and detailed information to the scheduler, along with telescope control data for the VLBI station (Walker, R. C., 2023). The VEX files created in SCHED are then processed using the field system.

When you input VEX files into the appropriate instrument's field system, they are then processed using DRUDG. DRUDG produces two types of output files, SNAP and PROC files. As previously described, SNAP files contain instructions on what sources are being observed, when they are to be observed, and how long to observe them. PROC files configure the local hardware of the telescope to set up components such as the receiver and recorder, ensuring data capture at the right times.

3.1.4 Observation

The original intent for this investigation was to observe multiple bright methanol maser sources to use as subjects for spectral line shape analysis. The methanol masers selected were G9.62 + 0.19, G323.74 - 0.26, G339.88 - 1.25, and G351.41 + 0.64, all of which emit in the 6.7 GHz range. These sources were chosen after consulting the General Catalogue of 6.7 GHz Methanol Masers (Pestalozzi, Minier & Booth, 2005), accessed via the CDS VizieR library of published astronomical catalogues, based on their intense radiation flux densities (within the range of ~ 1500 → 7000 Jy). These sources are all visible in the Southern Hemisphere, making them easily observable from the position

of the Warkworth Observatory.

After the selection of the four maser sources, attention turned towards formulating the key file for the observation. The key file template used was the G9.62 Master Copy employed by the IRASR for observations of methanol masers. Modifications were made to this template to accommodate the observation of the four maser sources. Details including the right ascension (RA) and declination (DEC) coordinates for each source, as well as the relevant equinox and epoch (J2000), were specified. The scan information included elements such as the observation's date, time, station, and scan configuration. To ensure comprehensive data acquisition, the scan configuration was designed to record each source in sets of two-minute observations, interspersed with 30-second interscans. This sequence was to be repeated five times for each of the four sources, resulting in a total recording time of ten minutes per methanol maser source. The observation was scheduled to commence on the 19^{th} of September 2022 at 4:30 pm, when all objects of interest would be readily visible.

The completed key file was then processed by SCHED, producing the VEX file that could then be run through the Warkworth 30-m telescope's field system. The key and VEX files have been included in Appendix C.

3.2 Data Processing

3.2.1 Autocorrelation

The brunt of the data processing is done in Mark5access, which is a software package equipped with tools used to decode and perform various types of analysis on data files recorded with Mark5 recorders (Natusch, 2015). Of particular interest is its ability to produce a spectrum from time series data through autocorrelation. m5spec is the built-in autocorrelator that has been specifically written to understand data that follows

the VLBI Data Interchange Format (VDIF). Though the observations done within this thesis do not involve VLBI, VDIF is still applicable to our uniformly time-sampled data. Thus, m5spec is the most accessible means of autocorrelation for the data format that we use.

The observational data for each source is recorded in scan subfiles. For a 10-minute scan of one maser source (600 seconds), the scan is divided into subfiles of 8-second increments of recorded data. This means that for each of the four sources, there are a total of 75 files $(0 \rightarrow 74)$ of 8-second data sections $\left(\frac{600}{75} = 8\right)$. To process all of the data, each subfile for each of the sources must be individually run through the m5spec autocorrelator. Before investing time in completing this process for all the sources, one subfile was autocorrelated from each source to examine the data quality. The data from each subfile was able to be visualized using a script file that invokes m5spec and runs a Gnuplot script that plots the generated spectra (Natusch, 2015). The generated spectra are by default plotted as four channels of data. The results of which look similar to the example below.

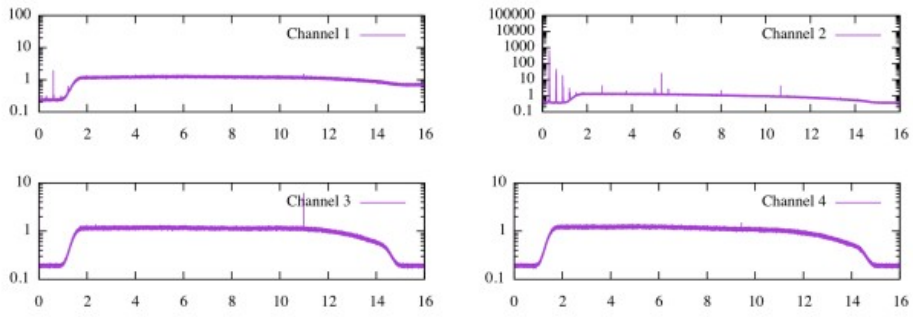

Figure 3.5: Example Gnuplot of an observation of methanol maser G9.62 + 0.19E. Source: (Natusch, 2015).

When looking at the spectra from each of the four sources, only the maser G9.62 + 0.19E contained a discernible signal for the peak at 6.7 GHz. The reason for this is not certain, though it may have been an error during the recording process or within

the instrumentation itself. Due to this, it was decided that only the observations from source G9.62 + 0.19E would be fully processed and used in this work. While not ideal, this is still an acceptable outcome - since historically, G9.62 + 0.19E has the brightest spectral peak of all of the methanol maser candidates, as well as having distinct spectral features.

Once all of the G9.62 + 0.19E files were autocorrelated (75 in total), the data was exported and combined into a single Excel spreadsheet. The autocorrelated data from each individual file was arranged into five columns; the first column is the frequency index relative to the reference frequency of 6660 MHz, the second is the Channel 1 data for right-hand circular polarization (RCP), and the fourth column is the equivalent Channel 3 data for left-hand circular polarization (LCP). Both columns three and five contain data from channels offset in frequency that can be used for calibration.

The frequency range is 16 MHz, therefore, the number of data points (rows) in each of the columns is:

$$2^{16} = 65536 \tag{3.1}$$

The spectral resolution of the data is then given by:

$$\frac{16MHz}{2^{16}} \simeq 244Hz \tag{3.2}$$

This corresponds to a velocity resolution of $d_v = 0.01$ km/s, which is sufficient when dealing with spectral lines of a few km/s widths.

3.3 MATLAB

MATLAB provides an extensive toolbox, efficient data handling, powerful visualization, and algorithm development flexibility, making it a valuable tool for spectral

processing. Therefore, it was the preferred language and interface for the analysis of the observational maser data.

3.3.1 Importing and Formatting Data

The initial step in MATLAB involved importing observational data from an Excel spreadsheet and converting it to a .mat file, which is a binary format used in MATLAB for storing and managing data. These files retain the data's structure, facilitating convenient retrieval and manipulation. The transition to .mat files preserves important attributes like variable names, sizes, and types. Additionally, the format supports efficient compression, aiding in reducing file size and code execution time.

As previously discussed, the data within the spreadsheet was split into 75 lots of five-column groups, of which, only the second and fourth columns (RCP and LCP, respectively) were of interest. Thus, when the spreadsheet was being converted, additional code was added to specify that only the columns containing RCP and LCP data would be moved into the .mat file. This meant that the final .mat file was a 65536×148 matrix.

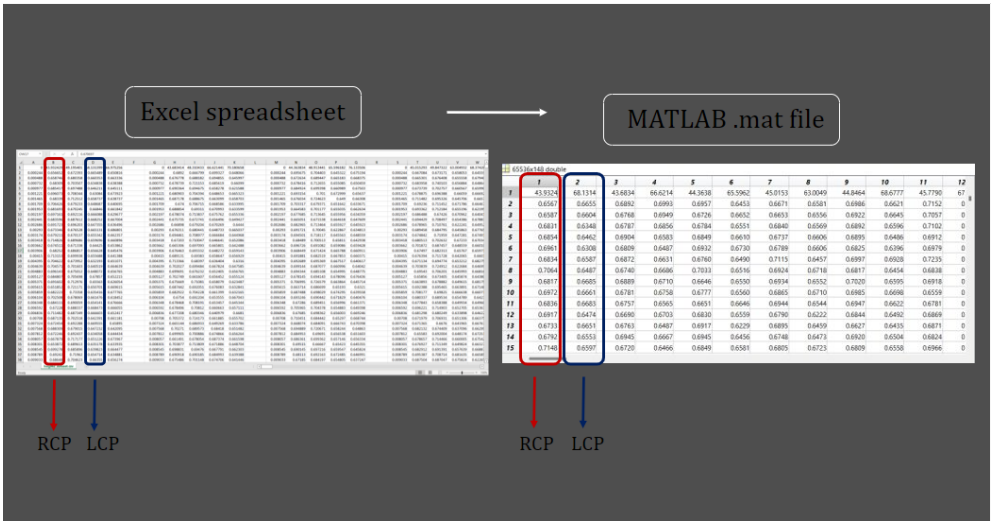

Figure 3.6

The raw data needed to then be processed to minimize the presence of noise and background continuum radiation, while still preserving the smaller, less intense spectral features. The noise reduction method used in this work is Software Frequency Switching (SFS).

3.3.2 Software Frequency Switching

Frequency switching (FS) is a data reduction technique used to systematically acquire information about weak spectral features in the presence of baseline fluctuations (Alexander & Gulyaev, 2012). Frequency switching can be done via a fixed frequency offset in the receiver hardware (Hardware Frequency Switching - HSF) (Robinson, 1964), or through recursive frequency switching in software (SFS). Both HSF and SFS can be used in conjunction, as introduced in the work of Bell (1997), where the dual use of the technique is referred to as 'SOFMOR' (Small-Offset Frequency Switching Multiple Overlap Reduction), and later as 'MFS' (Modified Frequency Switching) (Bell, 1997; Alexander & Gulyaev, 2012). In this thesis, SFS is utilized to reduce baseline fluctuations in the observed methanol maser data.

Frequency switching involves the subtraction of the original spectrum from a duplicated version that is adjusted by a specific number of channels (an offset). This process can be mathematically linked to a finite difference iteration(Alexander & Gulyaev, 2012).

Let h denote the offset, then

$$f_p = f(x + ph) \tag{3.3}$$

Formulae for the results of m frequency switching iterations are then

$$f^{(1)} = f_1 - f_0$$

$$f^{(2)} = f_2 - 2f_1 + f_0$$

$$f^{(3)} = f_3 - 3f_2 + 3f_1 - f_0$$

$$f^{(4)} = f_4 - 4f_3 + 6f_2 - 4f_1 + f_0$$

and so on, such that

$$f^{(m)} = \sum_{k=0}^{m} f_k \binom{m}{k} (-1)^{m+k} \tag{3.4}$$

m frequency switch overlaps generate a series of equidistant peaks with amplitudes $\binom{m}{k}(-1)^{m+k}$. The amplitude of each peak in the sequence can be illustrated using Pascal's triangle for six consecutive overlaps (three FS cycles) (Alexander & Gulyaev, 2012).

Every cycle of two consecutive overlaps produces a symmetric pattern with a pronounced central feature. The amplitude of this central feature, following i frequency switching cycles, corresponds to the central binomial coefficient (Alexander & Gulyaev, 2012).

overlap, m												cycle, *i*
0					1							0
1				−1		1						
2			1		−2		1					1
3		−1		3		−3		1				
4	1		−4		6		−4		1			2
5		−1		5		−10		10		−5	1	
6	1		−6		15		−20		15		−6	1 3

Figure 3.7: Pascal's triangle visualization of the binomial coefficients for overlaps *m* and cycles *i*. Source: (Alexander & Gulyaev, 2012).

$|A| = \binom{2i}{1} = (2, 6, 20)$ where $i = (1, 2, 3, ...)$

In this work, the observational data from G9.62 + 0.19E undergoes two frequency switch cycles (four consecutive overlaps). The final result is a symmetric pattern consisting of 5 spectra, with amplitudes of the following distribution: [1,-4,6,-4,1], relative to the original spectrum. Figure 3.8 is a theoretical representation of the pattern.

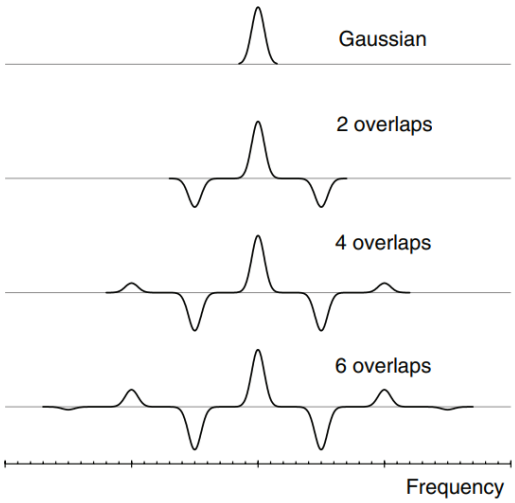

Figure 3.8: Transformation of a Gaussian shape after 2, 4, and 6 frequency switch overlaps. Source: (Alexander & Gulyaev, 2012).

The MATLAB code used to implement the frequency switches and smoothing procedures on the observational data has been broken down into steps and explained below. The full code is provided in Appendix B.

The first line of code loads the contents of the .mat file and assigns it to a data variable, with dimensions 65536×148. From the 65536 channels, we select the rows that contain the spectral features around the 6.7 GHz region of the 16 MHz frequency range recorded. The estimated location of these features was between rows 32500 and 34000, meaning there was an interval of 1500 rows containing the main spectrum.

Having defined the interval containing the spectrum, the code then loops through the data set separating the columns containing RCP and LCP values. Once divided, the RCP and LCP columns are then fed through a nested loop that applies the frequency switching. The mechanism used to implement the frequency switch, in this case, is a circular shift function that performs a cyclic shift of values by n positions within a data set. Here, our n value is defined as the 1500-row interval mentioned previously. The spectrum is shifted circularly by 1500 positions and then subtracted from the original spectrum.

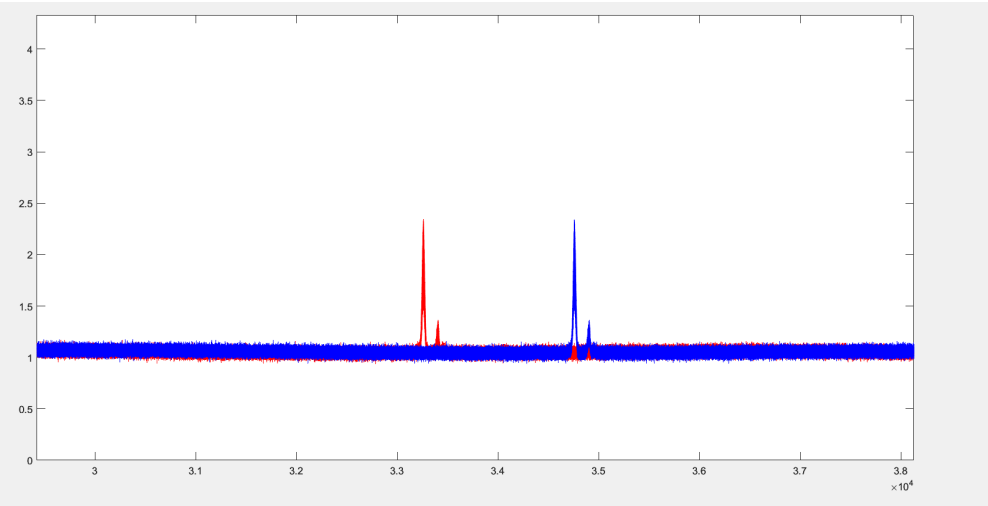

Figure 3.9: Original spectrum (in red) plotted next to the shifted spectrum (in blue).

This nested loop is repeated four times, for both of the RCP and LCP data sets. The result of the four overlaps (two frequency switch cycles), is a symmetric pattern of spectra with amplitudes of the distribution [1,-4,6,-4,1].

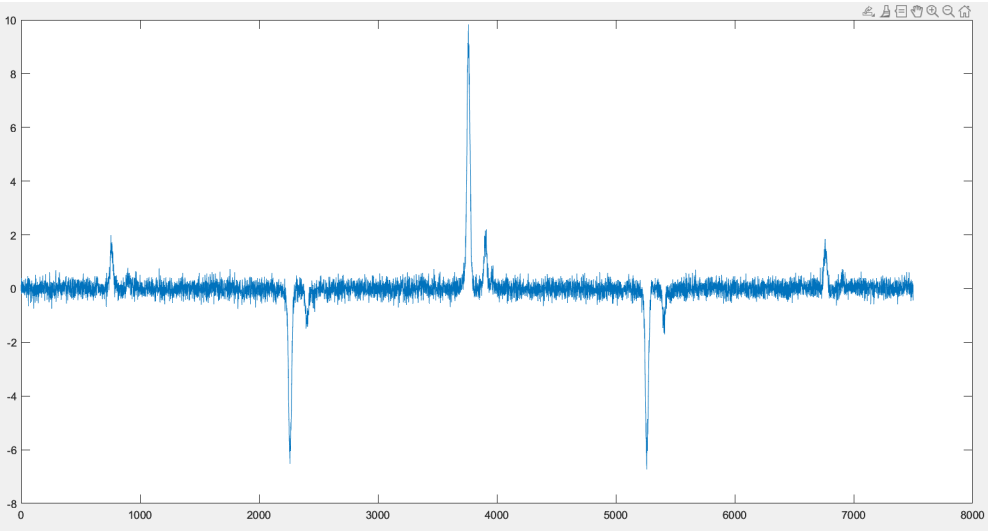

Figure 3.10: Symmetric pattern of five spectra resulting from two cycles (four overlaps) of frequency switching.

From the pattern of five spectra, the central feature is extracted and saved. The central features from both the frequency-shifted RCP and LCP columns are then recombined to create a new data set with the dimensions 1500×74.

The 1500×74 data set is then normalized so that it only contains values between 0 and 1. All of the RCP and LCP columns are then summed to create a 1500×1 matrix. The vector is then transposed to give a 1×1500 matrix.

The spectrum is then smoothed using a linear moving average filter of window size five. A moving average filter works by averaging a window of adjacent data points (in this case, five). Starting from the beginning of the signal, the window is moved across the data points. At each position, the window encompasses the set of five adjacent data points and calculates the average. The average value computed at each position becomes the output value of the filter at that position. The moving average filter acts as a low-pass filter, smoothing the data by attenuating high-frequency variations and emphasizing broader features of the spectrum. Through trial and error, the window size of five decidedly gave the desired degree of smoothing while still maintaining smaller details.

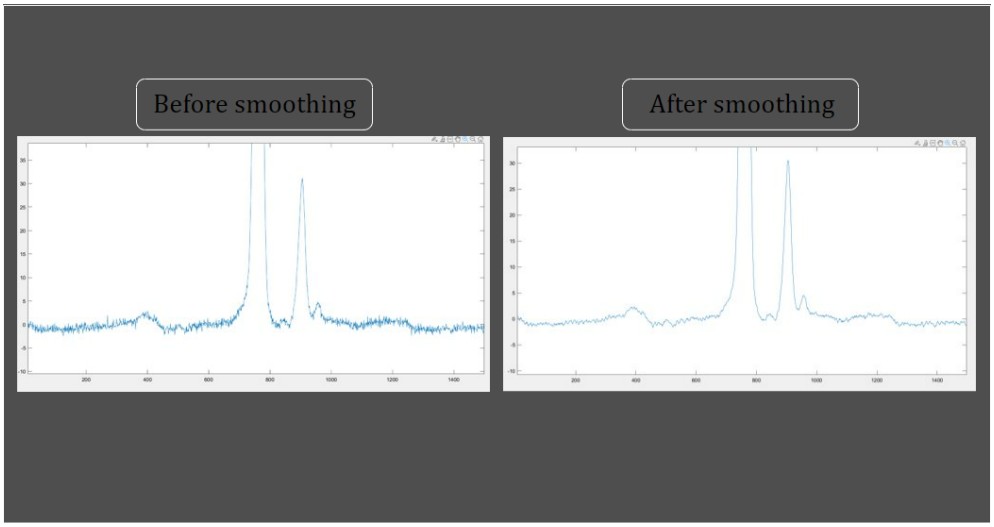

Figure 3.11: Symmetric pattern of five spectra resulting from two cycles (four overlaps) of frequency switching.

Next, the scales were set for the *x* and *y* axes. On the *x*-axis, the scale was converted to represent the frequency in megahertz (MHz), and the *y*-axis was converted to show the spectral flux density in Janskys (Jy). The *y*-axis was scaled according to the maximum

peak being 7000 Jy, this value was selected based on historical data for the spectral flux density of the maser source G9.62 + 0.19E (see Section 5.1.2 for the full explanation of the selection of this value).

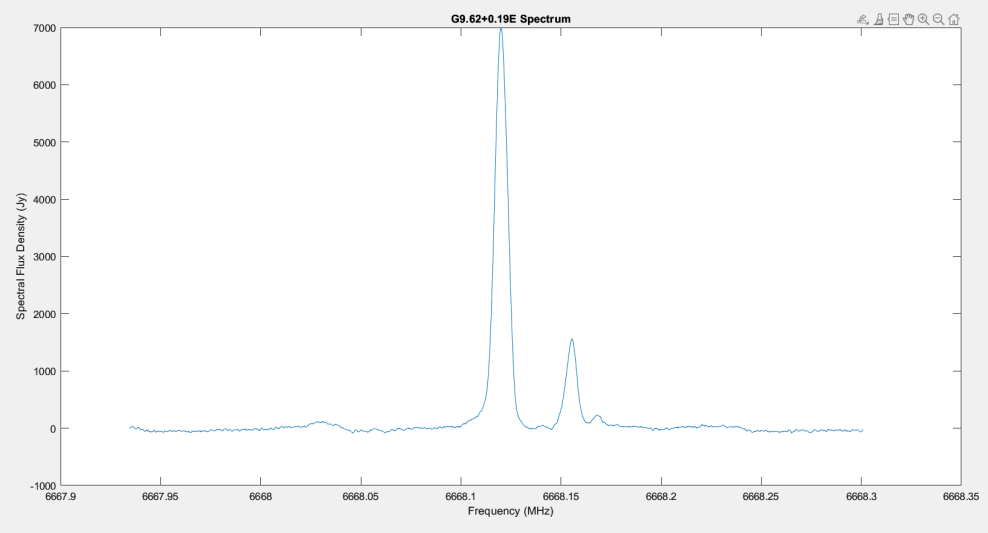

Figure 3.12: Smoothed G9.62 + 0.19E maser spectrum with scaled axes.

The implementation of the multiple frequency switching technique yields a significant reduction in the amplitudes of broad baseline variations, presenting an effective means of systematically "leveling out" baselines. In contrast to the standard approach of spline/polynomial baseline fitting, which often entails subjective judgments of the zero level of the spectrum, the employment of the frequency switching technique objectively removes gain variations (Alexander & Gulyaev, 2012).

3.3.3 Isolating the Main Spectral Features

An additional step is done to isolate the main spectral features. The spectrum becomes easier to analyze and extract information from the simpler it is. Since fewer features are present, the line shape is less complicated to model. The isolation is done by selecting the rows in the data that contain the main spectral features and plotting them separately. The x-axis is also converted from frequency (MHz) to velocity (km/s) by scaling the

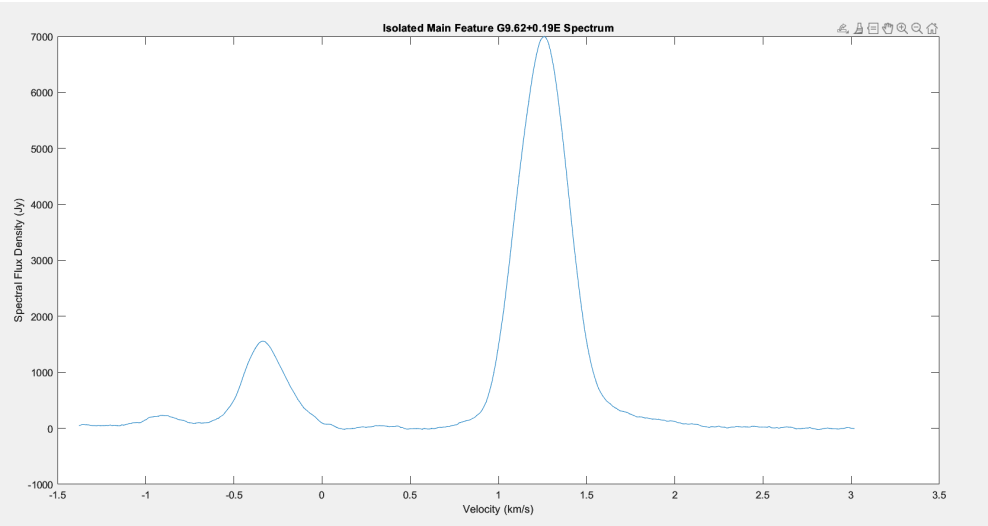

Figure 3.13: Isolated main features of the G9.62 + 0.19E methanol maser spectrum, with the x-axis converted to velocity (km/s).

values such that the maximum component at 6668.148 MHz corresponds to a radial velocity of 1.25 km/s (see Section 5.1.2 for the full explanation of the selection of this value).

3.3.4 Polynomial Fit Removal Comparison

Here, a comparison is made between the frequency-switched spectrum and the spectrum having been modified using the polynomial removal technique. The goal is to show the difference in objectivity between the two methods of data reduction. Below is an example of the procedure for polynomial removal. The fitting and removal of the polynomials are also carried out in MATLAB, on the same raw data obtained from the observation of G9.62 + 0.19E.

Starting with plotting the raw data to see the full spectrum of recorded information (Figure 3.14).

The main spectrum is then located, and the main features are isolated. This is done using the same boundaries from the frequency-switched spectrum isolation (Figure

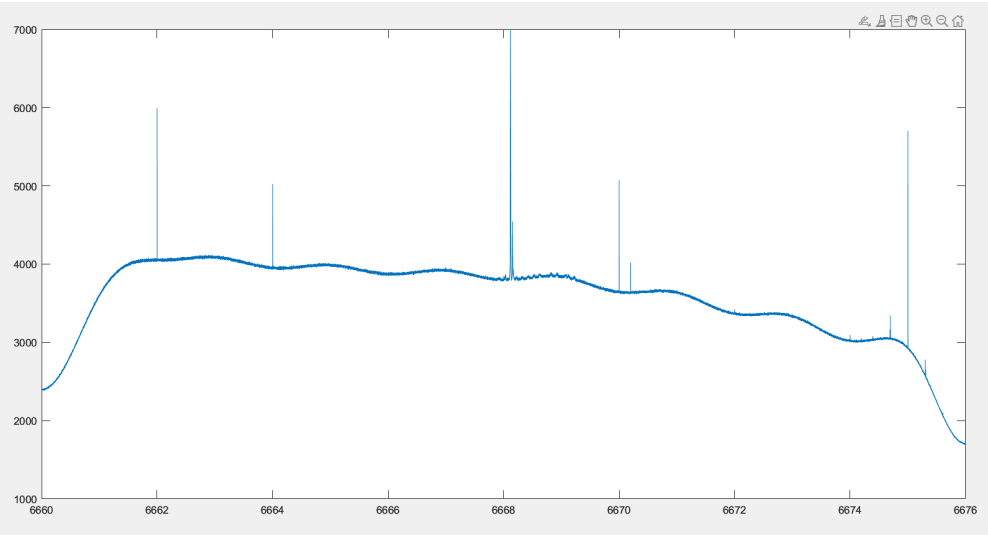

Figure 3.14: Raw data spectrum converted to Janskys (y-axis) and MHz (x-axis).

3.15).

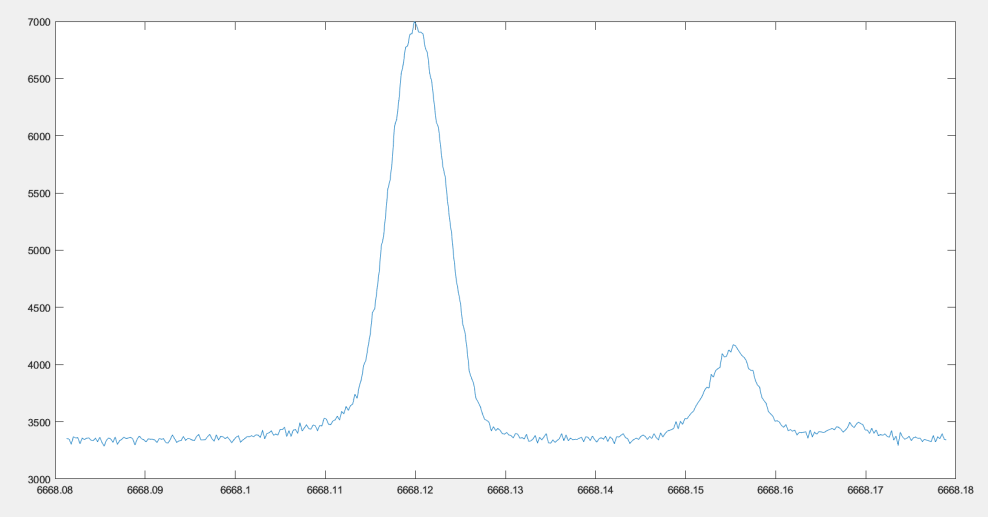

Figure 3.15: Raw data spectrum showing only the isolated main features.

The spectrum is then smoothed using a moving average with window size four, via the same procedure used during the frequency switching sequence (Figure 3.16).

Using the MATLAB built-in getpts function, one can manually select points on the spectrum for a polynomial of n^{th} degree to be fit to. In this case, a 5^{th} degree polynomial is fit along the perceived zero-baseline of the spectrum (Figure 3.17).

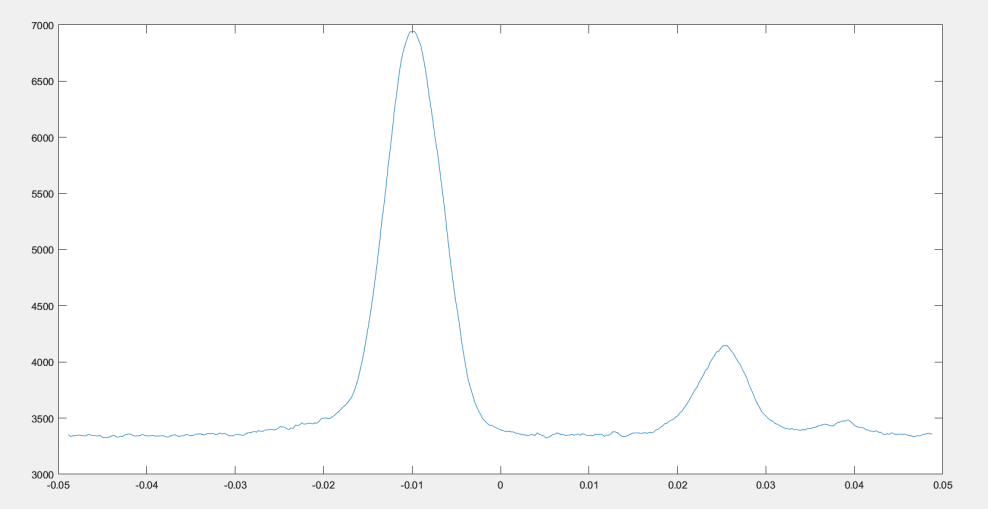

Figure 3.16: The spectrum smoothed with a moving average and the x-axis centered on zero.

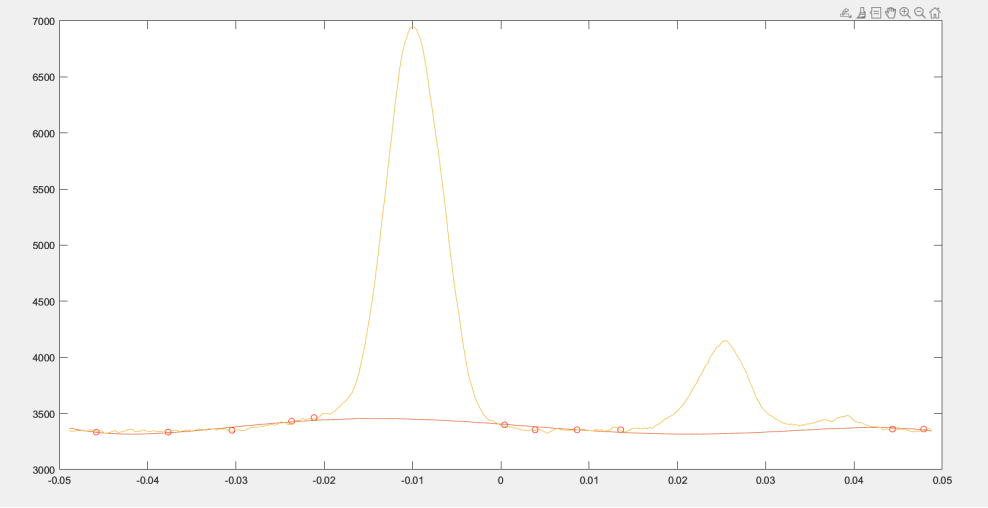

Figure 3.17: Using MATLAB function "getpts" a 5^{th} degree polynomial is fit to the selected points (circled in red).

The shading of the area under the selected polynomial points highlights the data being removed below the perceived zero-baseline of the spectrum (Figure 3.18).

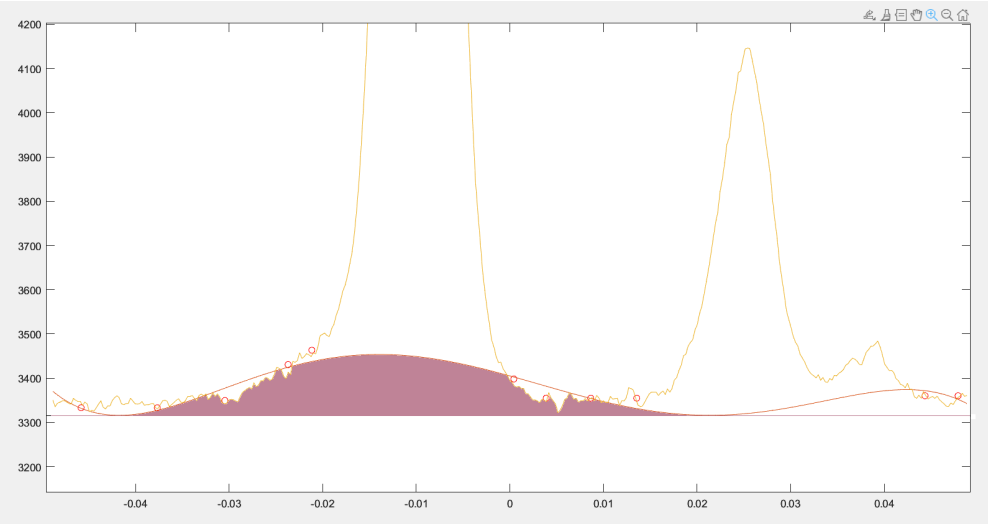

Figure 3.18: The shaded area beneath the getpts polynomial that is to be removed from below the perceived zero-baseline of the main spectral feature.

After the points for the polynomial fit have been manually selected along the baseline, the polynomial can then be subtracted from the original spectrum (Figure 3.19).

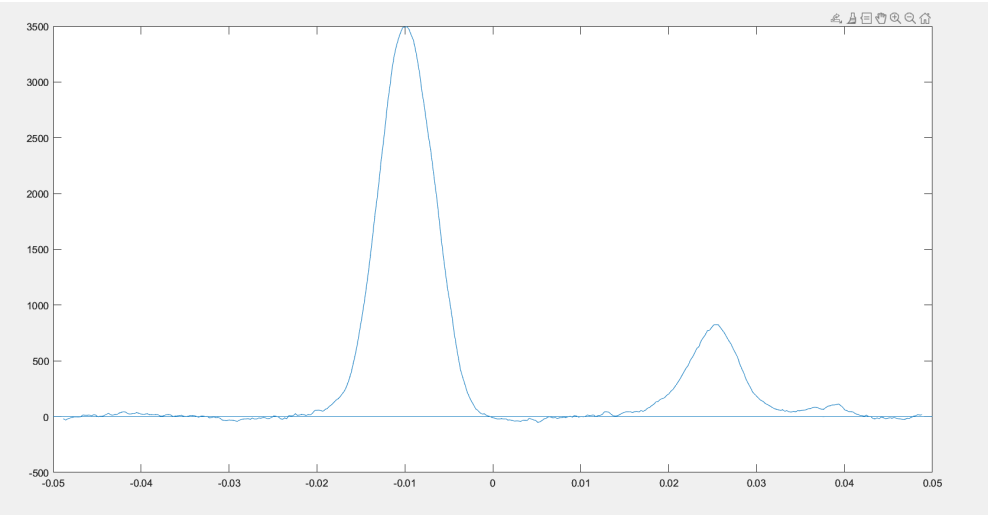

Figure 3.19: The spectrum after the selected points have been fit with a 5^{th}-degree polynomial and subtracted from the spectrum.

The *x*-axis is then converted back into frequencies (MHz), and then into radial velocities (km/s) via the same scale used in the frequency switching method. The *y*-axis is then

re-normalized such that the maximum value is back at 7000 Jy (Figure 3.20).

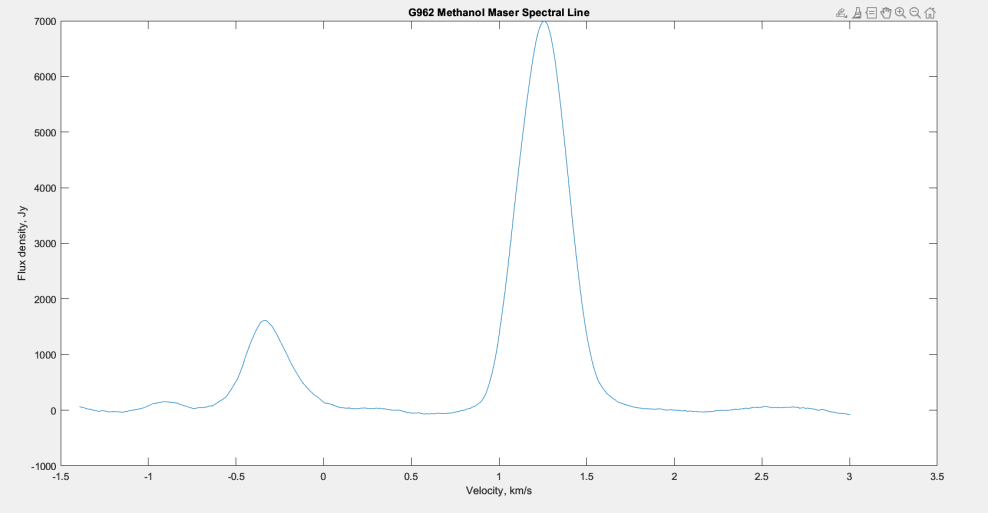

Figure 3.20: Polynomial has been removed and the spectrum has been re-normalized to 7000 Jy on the *y*-axis, and converted to radial velocity (km/s) along the *x*-axis.

When using the frequency switching method, what we are calling a "pedestal" feature at the base of the main spectral peak, should remain present above the zero-baseline. The appearance of this pedestal, which can be modeled by a Gaussian curve with a low amplitude and wide base, is predicted in our theoretical derivations (Section 2.4.1). Through the objective baseline removal of frequency switching, the pedestal feature can be better preserved. This elevation of the main feature is often removed during polynomial baseline fitting and has the potential to provide valuable insights into the physical properties of the maser source.

In Chapter 4, Gaussian curves will be fitted to the frequency-switched G9.62 + 0.19E data, and the presence of the pedestal feature will be investigated further.

Chapter 4

Results

In this chapter, observational maser data from G9.62 + 0.19E is fit with Gaussian approximations. In doing so, the presence of a theoretically predicted "pedestal" feature within the natural maser spectrum is investigated. The aim is to be able to deduce information about the physical characteristics of the maser source using the Gaussian approximations.

The theoretical model introduced in Chapter 2 (Equation 2.32), is designed to simulate the main feature of a maser spectrum. In reality, maser spectra often have multiple features aside from the main peak. This is the case for the observed spectrum of methanol maser G9.62 + 0.19E. Referring back to Figure 3.12, it is seen that there are smaller features closely surrounding the main feature at ~ 6668.148 MHz. As explained in Nesterenok (2016), The class II methanol masers at 6.7 observed via VLBI had displayed maser emissions indicative of the source consisting of multiple maser emission centres (referred to as 'maser spots'). The maser spots are often clustered in groups, corresponding to the maser features emitting in contiguous frequency channels, as observable in the spectrum of G9.62 + 0.19E (Nesterenok, 2016).

In Nesterenok (2016), it is also reported that the maser spot spectra are very well reproduced by single Gaussian profiles (as discussed in Chapter 2, Section 2.4.3.1). As an extension of this logic, an attempt was made to approximate the theoretical spectrum generated by the radiative transfer solution presented in Equation (2.32) using the sum of multiple Gaussians. Here, it was found that both the sum of the two and three Gaussians fits could well approximate the quasi-Gaussian theoretical model. Following on from this result, in this chapter, the possibility of fitting multiple Gaussians to the observed maser spectrum of G9.62 + 0.19E is explored. First, Gaussians will be fit to the multiple main features of the spectrum, then separately to the isolated central peak.

4.1 Fitting the Main Features

Looking at the plots of the main features of the spectrum (Figure 3.13), there are two comparatively large, distinct features, alongside a much smaller feature.

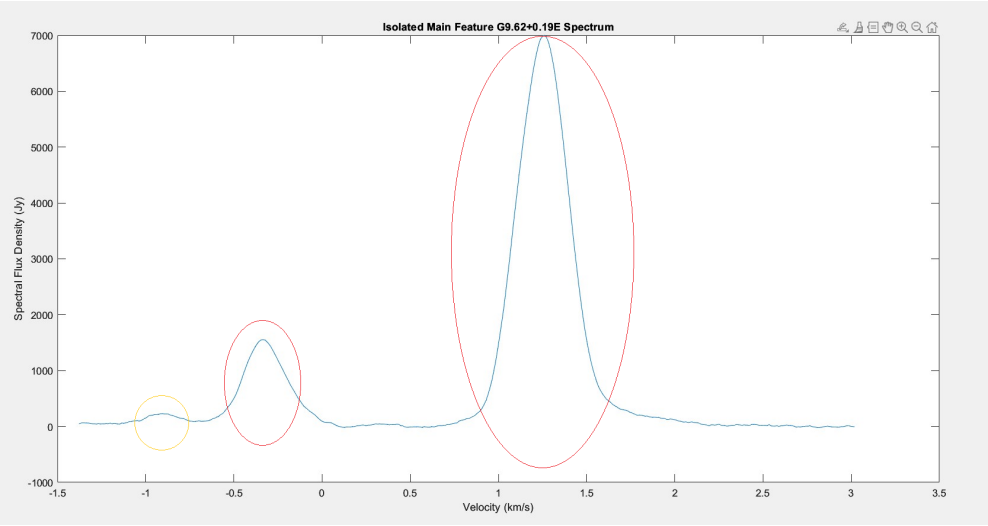

Figure 4.1: Two main features of the observed spectrum from methanol maser G9.62 + 0.19E (circled in red), and the small additional feature (circled in yellow).

Using the MATLAB 'lsqcurvefit' function, a specified number of Gaussians can be fit

to the spectrum. The 'lsqcurvefit' function is an optimization tool used for nonlinear least-squares curve fitting. Here, it fits a number of Gaussians to the observed spectral data by adjusting the model parameters (amplitude, mean, and standard deviation) to minimize the difference between the model's output and the observed data. The code employs the use of 'StartPoints', a vector that contains the initial parameter estimates for each of the Gaussians that are to be fit (three per Gaussian). These values act as a starting point for the optimization process performed by the 'lsqcurvefit' function. The 'StartPoints' are chosen subjectively by visually analyzing the spectrum.

The first implementation of this code used five Gaussians to fit the data - with the starting points prompting the algorithm to fit three of the Gaussians to the largest main feature, and the two remaining Gaussians to the second largest feature (seen on the left). See the results below in Figures 4.2 and 4.3:

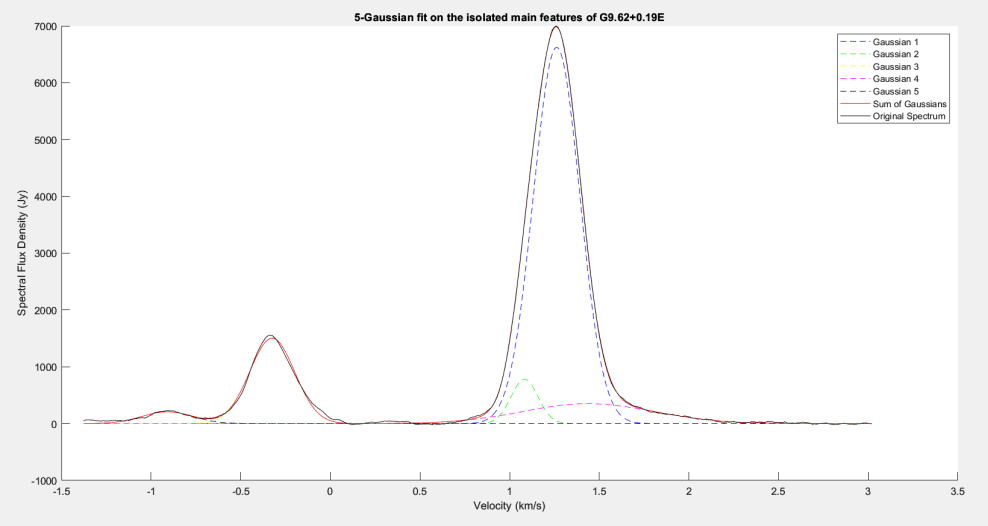

Figure 4.2: Result of fitting five Gaussians to the multiple main features of the observed spectrum for methanol maser G9.62 + 0.19E.

	Amplitude (Jy)	Width (km/s)	Line Centre (km/s)
Gaussian 1	6.6251e+03	0.1295	1.2619
Gaussian 2	782.3304	0.0751	1.0830
Gaussian 3	1.5038e+03	0.1253	-0.3247
Gaussian 4	350.4368	0.3667	1.4383
Gaussian 5	208.0159	0.1427	-0.9088

Table 4.1: Table of the five-Gaussian fit parameter coefficients.

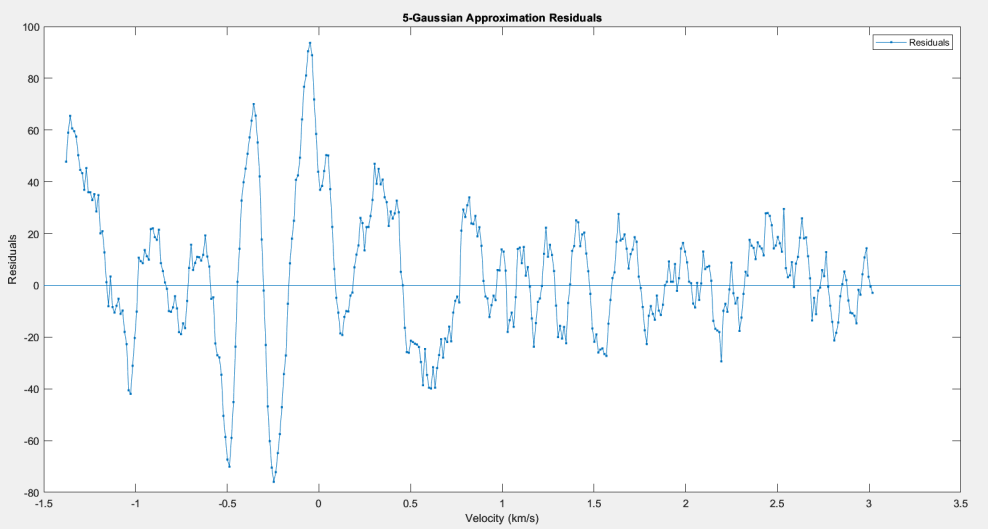

Figure 4.3: Residuals from subtracting the sum of the five-Gaussian approximation from the original data.

In Figure 4.2, the results of the 'lsqcurvefit' code for five Gaussians are presented. Taking into account the start point inputs, the fit function optimized the Gaussian fits such that three were fit to the central peak, and one was fit to each of the two other smaller features.

4.2 Fitting of the Isolated Central Peak

For the next iteration of the code, the maser spectrum was further isolated to just the largest main feature. As the 'lsqcurvefit' function had previously identified an optimal fit by employing three Gaussians for the central feature, this iteration similarly used three Gaussians to fit this particular feature once more. The purpose of isolating the

central feature in the maser spectrum was to closely align the observed data with the theoretical maser model spectrum (Section 2.4.3). Focusing on this central feature allows the observed spectrum to more accurately reflect the assumptions embedded in the theoretical model. This alignment enables the analysis of the observed data using the framework provided by the theoretical approximations, aiding in the extraction of information from the spectrum. This isolation is done by further restricting the x-axis values to only include the part of the spectrum containing the velocities applicable to the main feature (Section 3.3.3).

After making minor changes, the same code from the five-Gaussian version was able to be used for fitting three Gaussians. The fit specifications for the 'lsqcurvefit' tool were changed from five to three Gaussians, the number of start point inputs was reduced, and the isolated central peak was substituted as the original data.

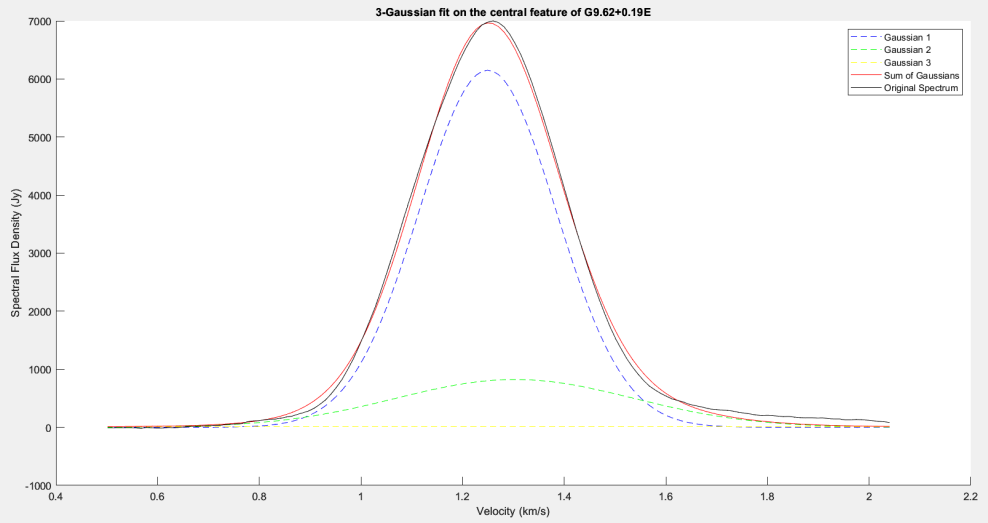

Figure 4.4: Result of fitting three Gaussians to the isolated main feature of the observed spectrum for methanol maser G9.62 + 0.19E.

Looking at the plot for the three Gaussian fit, a pedestal feature is visible, displayed as a green dashed-line Gaussian (Gaussian 2). The pedestal itself is slightly skewed to the right, which may be due to another small spectral feature residing within the right wing

	Amplitude (Jy)	Width (km/s)	Line Centre (km/s)
Gaussian 1	6.1515e+03	0.13565	1.2504
Gaussian 2	824.349	0.21808	1.286
Gaussian 3	36.8499	1.9568e+03	-3.1523e+03

Table 4.2: Table of the three-Gaussian fit parameter coefficients.

of the main peak. The first Gaussian (Gaussian 1) has an amplitude close to that of the original data, whereas the second and third Gaussians have much lower amplitudes. The three Gaussian approximations for the theoretical maser model predict that two of the Gaussians should be of similar width and amplitude (Figures 2.7 and 2.8), with the third Gaussian (the pedestal) being a fraction of the amplitude and observably wider. In this instance, the first Gaussian and pedestal features appear mostly as predicted, while the last Gaussian is of almost negligible amplitude and has the greatest width (Gaussian 3) (Figure 4.4).

Regardless, the residuals for the three-Gaussian fit are of the same magnitude as those from the broader-spectrum five-Gaussian fit, though distributed differently.

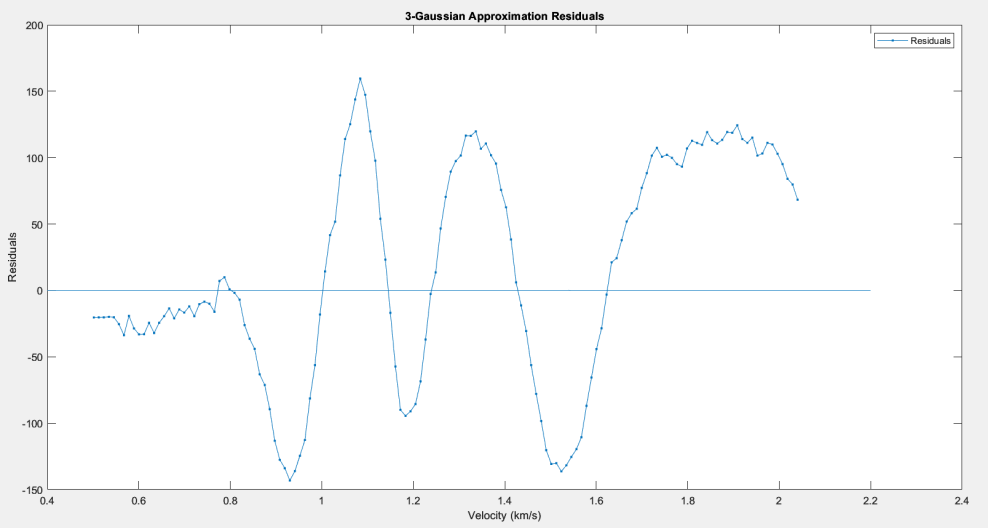

Figure 4.5: Residuals from subtracting the sum of the three-Gaussian approximation from the central spectral feature.

4.3 Optical Depth Estimations

As discussed in Chapter 2, Section 2.4.3, when fitting Gaussian approximations to the theoretical maser model, the ratio of the pedestal feature to the overall sum of the Gaussian fits varied alongside changes in optical depth. Based on this correlation, it should be theoretically possible to make an estimate for the optical depth of the observed maser source, based on the ratio of the amplitude and width of the pedestal Gaussian to that of the sum of the Gaussian approximations.

	Amplitude ± errors (Jy)	Width ± errors (km/s)
pedestal Gaussian	824 ± 304	0.22 ± 0.02
Sum of Gaussians	6975 ± 609	0.15 ± 0.03

Table 4.3: Table of the amplitude and width parameter coefficients for the pedestal feature and the sum of the Gaussians, with errors.

In the above table, the parameter coefficients for the Gaussian terms used in the ratio calculations are presented with their respective errors. These errors, as with the coefficients, are generated using MATLAB. The function 'lsqcurvefit,' used to fit the three Gaussians, returns various outputs for the fitted parameters, including the residuals and Jacobian matrix. The function 'nlparci' was then employed to estimate the confidence intervals (CI's) for the fitted parameters using these outputs. The standard error for each parameter was calculated using the CI values generated by 'nlparci.' The standard error is computed as half of the width of the confidence interval, which was initially given as 95%. The calculated errors were then divided by two to convert from a 2-sigma error (95% CI) to a 1-sigma error (~ 68% CI).

To obtain the optical depth estimate, the ratios for the amplitude and width of the pedestal to the sum of the Gaussians were then calculated.

$$\frac{A_{\mathrm{Pedestal}}}{A_{\mathrm{Sum}}} \propto \tau \tag{4.1}$$

$$\frac{W_{\mathrm{Pedestal}}}{W_{\mathrm{Sum}}} \propto \tau \tag{4.2}$$

The values for A_{Pedestal}, A_{Sum}, W_{Pedestal}, and W_{Sum} are taken from the table of parameter coefficients (Table 4.3).

First, the ratio of the amplitudes was calculated

$$\frac{824}{6975} = 0.12$$

Then the ratio of the widths was obtained in the same way

$$\frac{0.22}{0.15} = 1.47$$

The error of the ratios (σ_{Ratio}) was then calculated using the formula for the propagation of uncertainties

$$\sigma_{\mathrm{Ratio}} = \mathrm{Ratio} \times \sqrt{\frac{\sigma_A}{A}^2 + \frac{\sigma_B}{B}^2} \tag{4.3}$$

The error for the ratio of the amplitudes ($\sigma_{\mathrm{Ap/As}}$) was then given as

$$\sigma_{\mathrm{Ap/As}} = 0.12 \times \sqrt{\frac{304}{824}^2 + \frac{609}{6975}^2} = 0.04$$

Similarly, the error for the ratio of the widths ($\sigma_{\mathrm{Wp/Ws}}$) was calculated as

$$\sigma_{\mathrm{Wp/Ws}} = 1.47 \times \sqrt{\frac{0.02}{0.22}^2 + \frac{0.03}{0.15}} = 0.34$$

The ratios and their errors were then used to determine the corresponding range of optical depth values, using the graphs showing the ratios of the widths and amplitudes against optical depth (Figures 2.5 and 2.6).

	Ratio of the pedestal to the sum of the Gaussians ± errors
Amplitude	0.12 ± 0.04
Width	1.47 ± 0.34

Table 4.4: Table of the amplitude and width ratios with errors.

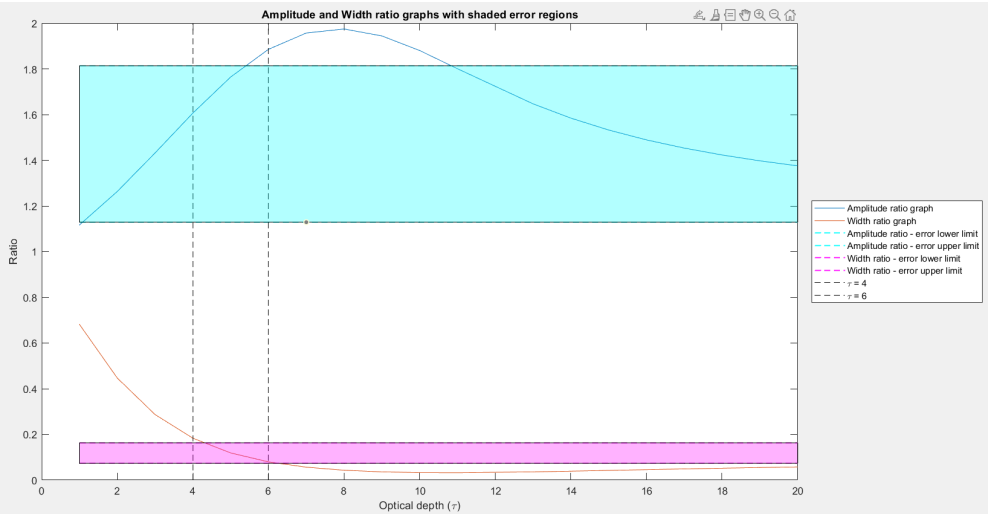

Figure 4.6: This plot depicts the ratios of the pedestal amplitude and width with respect to those of the sum of the Gaussian fits, plotted against the optical depth on the x-axis, with the y-axis representing the ratio values. The upper graph shows the ratio of the amplitude of the pedestal Gaussian to the amplitude of the sum of the Gaussians (as seen in Figure 2.5). The cyan-shaded area gives the error region for the amplitude ratio. The lower graph is the ratio of the widths of the pedestal Gaussians to the width of the sum of the Gaussians. The pink shaded area indicates the error region for the width ratio. The two vertical black lines at $\tau = 4$ and $\tau = 6$ correspond to the area of intersection of the error regions from both ratios, highlighting the range of agreeable optical depth values.

In Figure 4.6, it is seen that the region where both error regions intersect their respective graphs corresponds to an optical depth range approximately between $4 \leq \tau \leq 6$. This range serves as the optical depth estimate for the observed maser source, based on the

theoretical modelling framework proposed in Chapter 2. In Chapter 5, the results will be discussed alongside suggestions for improvements and future work.

Chapter 5

Discussion and Future Work

In this chapter, the results presented in Chapter 4 will be discussed in full. Integrated throughout will be recommendations for improvements that could be made to the presented work to make the results more robust. This will be carried out per the chapter structure, categorized as being related to the observation process or the theory. These proposed improvements can serve as suggestions to be accounted for in future work. In addition, steps that could be taken to further the work carried out in this study will also be presented.

5.1 Results

The results being discussed here will include both the three and five-Gaussian fits on the observed data from G9.62 + 0.19E, through to the final estimate for the optical depth range.

5.1.1 Five-Gaussian Fit

The five-Gaussian fit (Figure 4.2) on the observational data produced residuals (Figure 4.3) that were less than $\pm 2\%$ of the overall spectral flux density of the spectrum (both the observed data and the resulting sum of the Gaussians). Though the results were not included in this thesis, an eight-Gaussian fit was done on the same spectrum (Appendix A) and produced residuals that were almost identical in size (though distributed differently). A possible conclusion that can be drawn from this is that there are diminishing returns on the number of Gaussians being fit to a spectrum after a certain number. The number of Gaussians that would serve as the upper threshold for the accuracy one could achieve using this technique would depend on the complexity of the spectrum - more specifically, the number of features.

In both the case of the five-Gaussian and eight-Gaussian fit, the algorithm deemed it optimal to fit three Gaussians to the main feature that is centered near 1.25 km/s. This coincides with what was predicted theoretically in Chapter 2, though the presence of the pedestal feature was not as obvious or well formed as in the theoretical simulations (Figure 2.4). The altered appearance of the pedestal feature, in this instance, was postulated to be due to the Gaussians trying to fit the broader spectrum and not just the main peak. Thus, the three Gaussian fit on the largest main feature was carried out.

5.1.2 Three-Gaussian Fit

For the three-Gaussian fit, the spectrum was isolated further to include only the main central feature (Figure 4.4). This was done to try and better emulate the conditions of the theoretical maser model presented in Equation 2.32. The aim in doing so was to better investigate the presence of the pedestal feature in observed data that was as visually close to the model as it could be. The results of the three-Gaussian fit produced residuals (Figure 4.5) that were less than $\pm 3.5\%$ of the overall spectral flux density of

the spectrum (both the observed data and the resulting sum of the Gaussians). While the residuals showed slightly less accuracy in the three-Gaussian fit compared to the five-Gaussian, the pedestal feature was clearly present and of a similar form to that predicted by the theoretical Gaussian approximations. The main difference between the theoretical three-Gaussian approximations and the three-Gaussian fit of G9.62 + 0.19E was in the individual amplitudes of each Gaussian.

When fitting three Gaussians to the theoretical maser model, the general trend showed that two of the Gaussians were close in amplitude (Figure 2.7) and in width (Figure 2.8), with the third having a lower amplitude and greater width. However, in the plot showing the three Gaussians fit to the main feature of G9.62 + 0.19E (Figure 4.4), it is seen that most of the data points are accounted for by the first Gaussian of high amplitude (close to that of the maximum spectral flux density of the spectrum) and the second pedestal Gaussian. The third Gaussian, in this case, is of negligible amplitude but is very wide (Table 4.2). The first two Gaussians of this fit more closely resemble the theoretical two-Gaussian approximations than the theoretical three-Gaussian fits. The third Gaussian could be interpreted as the fit algorithm accounting for baseline variations still present after the digital frequency switching process (Chapter 3, Section 3.3.2).

The errors were calculated for the parameter coefficient estimates for the sum of the Gaussians and the pedestal Gaussian. The errors were given for these two fit components since they would be used in the ratio calculations when estimating the optical depth. Here, the decision to use 1-sigma errors (~ 68% CI) instead of 2-sigma errors (95% CI), was made to provide a more conservative estimate, considering the level of variability beyond the model's scope. The resulting error percentages for the amplitude parameters of the sum of the Gaussians and pedestal Gaussian were ± 8.7% and ± 36.8%, respectively. For the width coefficients, the error percentages were ±

21.1% for the sum of the Gaussians and ± 9.7% for the pedestal.

In the context of the methanol maser source G9.62 + 0.19E, the parameter estimates for the amplitude, and the corresponding errors, are within the expected range of values for the flux density. Since its discovery in 1991 (Menten, 1991), the spectral flux density of G9.62 + 0.19E has been consistently reported as being of magnitude 10^3 (Jy). The historical range of values for the spectral flux density of this source is generally between $5000 \rightarrow 7000$ Jy (Caswell, Vaile, Ellingsen & Norris, 1995; Green et al., 2010; MacLeod et al., 2020). However, cases of more extreme values ranging from 4500 Jy (Goedhart et al., 2003) up to 8624 Jy (MacLeod et al., 2020) have been reported. In Chapter 3, a spectral flux density value of 7000 Jy was chosen as the maximum used to scale the rest of the y-axis data. The selection of a spectral flux density value at the high end of the range for the historical values of the source was done to reflect the tendency of the spectral flux density to increase in the more recent observations. This may be suggestive of the maximum spectral flux density of maser flares increasing over time, or simply be a result of the high variability of the source.

The parameter values for the sum of the three-Gaussian approximations (Table 4.2) are agreeable with both the scale of the 7000 Jy spectral flux density assigned to the data, as well as historical accounts of observations done of G9.62 + 0.19E.

In early 2020, another observation of G9.62 + 0.19E was done on the Warkworth 30-m telescope (Natusch, 2020). The spectral flux density recorded for this observation was 6280 Jy, with a radial velocity of 1.27 km/s, and a line-width velocity of 0.2 km/s. Since this observation was conducted similarly to the one in this thesis, using the same equipment, it provides a good point of comparison. These observed values are very close to the parameter coefficient values, indicating that the sum of the Gaussian fits can effectively approximate the parameters of the spectral features.

In terms of statistically analyzing the fit of the Gaussian approximations to the data, using an AIC (Akaike Information Criterion) or RMSE (Root Mean Square Error) to evaluate the parameter estimations could be beneficial. However, this may be difficult given the complexity of variables contributing to the model. If one were to get accurate results from these approaches, estimations would need to be made for the degrees of freedom of each parameter. Both AIC and RMSE methods are more commonly used to analyze regression models, which means the results for calculating either value for the spectral approximations would require more subjective interpretations.

5.1.3 Optical Depth Estimation

Looking at the results of the ratio graphs with error regions, we can see that there are two sections on the top graph where the region intersects the graph. Based on this, it is likely that there would be another point of intersection on the bottom graph as well, though it would seemingly occur at optical depths > 20.

As it stands, with this model there is no way to discern the true optical depth out of the two regions of intersection. However, there are likely contextual clues based on other physical properties of the maser source. Other techniques may be used in conjunction to help predict a reasonable range for the optical depth values. This is assuming that the relationship between the parameters of the pedestal feature and the sum of the Gaussian fits is an effective indicator of optical depth. Another aspect to note is that the optical depth estimate does not account for the possibility of varying densities between masing spots within the source.

Using the method proposed in this thesis, the accuracy of the optical depth estimate is limited by the constraints of the model. The compounding errors accumulated during each step of the process presented in this work culminate in the difficult task of determining how reliable the results are. It would negate the simplicity of using

the multiple-Gaussian model to fit the observational data if one needed to quantify the potential error sources at each step. For instance, measurement errors, modelling errors, residual errors, parameter estimation errors, and extrapolation errors. Given this, the best way to substantiate the validity of the results (for the optical depth estimates) would be to conduct the same experiment on a source with known, or predicted, optical depth values. This would help ascertain if the parameter ratios of the Gaussian fits are effective predictors of optical depth.

Conducting the same set of observational and modelling procedures on an alternate maser source would probably emphasize the necessity for refinements in the theoretical model. A recreation encompassing the observation, data processing, modelling stages, and parameter estimations, would likely demonstrate the need for modifications in the theoretical framework. The assumptions incorporated into the theoretical model for the sake of simplicity are likely to the detriment of the versatility of the model in accounting for the varied physical conditions of diverse cosmic masers. In saying this, the model presented here serves as a baseline that can be built upon to improve adaptability and robustness.

The assumptions integrated into the theoretical model, while intended for simplicity, might limit the model's adaptability to address the diverse physical conditions found in various cosmic masers. Nonetheless, this model serves as a foundational framework that can be refined and expanded upon to enhance its adaptability and robustness.

5.2 Improving the Theoretical Model

The theoretical model introduced in Chapter 2 was derived with the goal of it being relatively simple to implement while being able to effectively emulate the shape of the main feature of a maser emission spectrum. Using the theoretical model as a baseline to

represent an individual spectral feature, the possibility of describing the feature using multiple Gaussian curves was explored. Based on the ability of the multiple Gaussians to fit the theoretical model of the spectral feature, it was decided to test the Gaussian fits on a real observed maser spectrum. The results of the Gaussian fits on the observed data, and subsequent insights obtained, are limited in accuracy by the level of complexity in the theoretical model. While the simplicity of the theoretical model makes it easier to use, the model's ability to account for the large physical variance of real cosmic masers is compromised.

The multitude of variables and unknowns that contribute to each aspect of maser emission and its resulting spectra is immense. This makes the task of modelling maser emission difficult and involved. Sobolev and Gray (2012) break down the modelling process in their work "Modelling of Cosmic Molecular Masers: Introduction to a Computation Cookbook" (Sobolev & Gray, 2012).

The authors begin by explaining that maser models should be numerical, as analytical estimates are typically only of qualitative value. Analytical maser models are less applicable due to the complex nature of astrophysical maser sources and their environments. The pumping mechanisms and saturation regimes dictating the population inversion of masing molecules are incredibly involved, with the number of associated levels and transitions being in the hundreds (Sobolev & Gray, 2012).

Cosmic maser environments consist of interactions between different elements of matter, radiation, magnetic fields, and velocity fields. The interplay of these various components suggests that simple geometric models can only offer limited approximations (Sobolev & Gray, 2012).

The complexities of astrophysical masers limit the model's level of detail and accuracy, constrained by both the available computing power and the author(s)' experience

(Sobolev & Gray, 2012).

In this work, both analytical and numerical estimates are used in conjunction, with numerical substitutions being made as necessary to reduce the scale of the research needed to construct the model. Due to the inherent complexity of maser sources and the scope limitations of a master's level thesis, it wasn't possible to fully delve into all four suggested areas of research. However, future iterations of this work could benefit significantly from incorporating as many of these areas as feasible. The objective of deriving the model in this manner was to incorporate assumptions and approximations that would enable the model to generate a theoretical maser spectrum with a prominent main feature. This theoretical spectrum could serve as a basis for modelling a real observed maser spectrum, aiming to extract valuable information regarding the physical conditions of the observed maser source.

5.2.1 Molecular Level Scheme

The model presented in this thesis is based on an idealized two-level system, as seen in Litvak (1970), Trung (2009), and Gray (2012). Here, the level scheme of the methanol maser is simplified to that of one upper and one lower level. This is a frequently adopted approach that reduces the amount of background molecular spectroscopy information needed to formulate the model. However, the two-level approximation does not account for the litany of less populated level transitions that may be connected to the highly populated transitions. In most instances, this process involves the collective action of multiple pumping cycles. These cycles are connections between energy levels within the molecule, forming quantum-mechanical transitions primarily driven by radiative or collisional processes (Sobolev & Gray, 2012).

Methanol molecules exist in two symmetry states, denoted A and E, which differ in the alignment of the nuclear spins. The A-symmetry species has close pairing of levels,

which are labeled by a ± symmetry label (related to the parity quantum number). In the case of class II methanol maser, G9.62 + 0.19E, the most prevalent line is the $5_1 - 6_0$ A^+ transition at 6.668 GHz. However, radiative transitions between different torsional states are also strongly allowed due to the large degree of torsion–rotation interaction in methanol (Section 1.2.4). It has been shown that sparsely populated torsionally excited levels play the role of important transients in the pumping of class II methanol masers (Sobolev & Deguchi, 1994; Sobolev et al., 2007).

The best-case scenario is that the levels that are essential to the pumping mechanism are known. In situations where sufficient molecular spectroscopy data is available, it is recommended by Sobolev and Gray (2012) that one follows the level scheming approach presented in Sobolev and Deguchi (1994).

5.2.2 Rate Coefficients

Following on from the level scheme is the problem of defining the rate coefficients. In the theoretical works referenced in this paper, the rate coefficients are defined for the emission, absorption, and collisional processes of a two-level molecular system. These analytical rate coefficient formulae were used in the derivation of our theoretical maser model, but at no point were numerical estimates incorporated. In order for the model to best describe the behaviour of the maser source, numerical values should be obtained from existing molecular data. These values should incorporate estimates for the energies of the various accessible quantum states, Einstein coefficients (or line strengths governing radiative transition rates), and collisional rate coefficients (Cragg et al., 2005).

If one were to design a model beyond the scope of the two-level idealization, the coefficients for collisional transitions between every pair of energy levels being considered would need to be included in the calculation. Since methanol has a huge number of

levels which may be populated under interstellar conditions, it would be exceedingly difficult to access molecular data for an all-encompassing level scheme. Thus, it is suggested that data is provided for the most essential transitions and that other supplementary rates are approximated where necessary (Sobolev & Gray, 2012). In Cragg et al. (2005), these 'missing' rates are approximated by extrapolating the known rates according to existing propensity rules (Cragg et al., 2005).

The process of substituting specific numerical estimates for the rate coefficients particular to the molecular species responsible for the maser emission would enhance the model's ability to depict real-world phenomena. However, the steps involved in acquiring the necessary molecular data to do so would complicate the model development (Sobolev & Gray, 2012).

5.2.3 Conditions of the Masing Region

The next part of the input consists of a description of the physical parameters in and around the masing region. The internal conditions include the kinetic temperature, abundance of the maser molecule and number density of the medium, the velocity field, and the dust temperature. External conditions are typically limited to radiation fields, usually that of nearby protostellar objects (in the case of masers in star-forming regions). Population transfer rates are usually represented as products of a (first-order) rate coefficient and a fractional-level population. The functional forms of collisional rates are relatively well-known and are usually determined by the kinetic temperatures of collisional partners. The functions of physical parameters associated with the radiative rates are much more complicated, as they require a solution to the radiative transfer problem (Sobolev & Gray, 2012).

Radiative rates are determined by internal and external emission sources, as well as the extinction (absorption and scattering) of the emission within the masing region.

Most frequently, the pumping of the maser source comes from the collisional excitation and radiative decay of the masing molecules, before the photons escape the masing region. It has also been established that absorption by internal dust can produce maser activity, even when the large optical depth prevents the escape of photons. In some instances, internal dust can also serve as a source of energy in the pumping of the maser region (Voronkov, Sobolev, Ellingsen, Ostrovskii & Alakoz, 2005). The same is true for external dust emissions from the surrounding environment contributing to the pumping mechanism (Sobolev & Gray, 2012).

Molecular abundances are also important to consider, as high abundances can result in restrictions on the physical state and evolution of the masing region. The brightness of the maser is related to the molecular abundance through the number of masing molecules along the line of sight (Sobolev & Gray, 2012).

The geometry of the masing region is an essential component in the solution of the radiative transfer problem. For stellar masers, the most commonly considered geometry is spherical, since these masers form in shells in the circumstellar envelope (Sobolev & Gray, 2012). In this work, the maser model is one dimensional along the z-axis with cylindrical pathing through a spherical masing cloud. In reality, the propagation of radiation happens in three dimensions, and the shape of the masing region is likely to have a degree of asymmetry as a result of anisotropic background radiation or from the elongation of the cloud (Alcock & Ross, 1985).

Within the overall shape of the masing region, there is the question of the internal distribution of maser spots. The two main scenarios describe maser spots as discrete clumps, or as correlations in extended regions. The discrete clumps are assumed to be concentrated regions (density inhomogeneities) within the maser source, with sizes comparable to the observed maser spots. Whereas the potentially extended regions are thought to be forming maser spots due to connections or alignments in certain

physical parameters, such as velocity fields or structural alignments along the line of sight. It is likely that cosmic maser spots exist as some combination of the two, and their images, spectra, and evolution are determined by both. Though a decisive computational solution to the problem has yet to be devised to fully replicate observational data, it is still beneficial to keep these maser spot configurations in mind when dealing with maser geometries (Sobolev & Gray, 2012).

The general approach to solving a model for a particular parameter is to calculate the population numbers for the masing molecule at discretized positions within the model geometry. For instance, Goldreich and Keeley (1972) describe the integral solution for the intensity of a uniform spherical maser model as the set of population numbers at each modeled radius. A similar approach is adopted in this thesis, via the sum of cylindrical 'pencil' models within a larger spherical shell.

5.2.4 Radiative Transfer

To solve the parameter model described, it is necessary to solve both the radiative transfer and kinetic master equations simultaneously. In this thesis, formulations of the standard, and semi-classical (where molecular response is treated quantum-mechanically through density-matrix theory), maser radiative transfer equation are examined (Chapter 2). The generalized form of these equations is given in Equation 2.24. Sobolev and Gray (2012) highlight that even in basic models with unsaturated maser radiation and unresolved radiative transfer problems, a substantial computational effort is necessary. The case of low maser saturation is considered in this thesis, which helps to simplify the radiative transfer equation and enable the non-numerical solution (Sobolev & Gray, 2012). However, this approximation comes at the cost of the accuracy of the model, as the lack of saturation term means a significant physical characteristic of the maser source is unaccounted for. Though the saturation of the source was not known in this

case, a better approach may have been to solve the radiative transfer equation using a range of numerical substitutions for the degree of saturation (I_s).

Sobolev and Gray (2012) highlight the multiple factors that require consideration in numerical computations of the radiative transfer equation for maser emission propagation. It is explained that specific challenges arise in modelling maser radiation propagation, as opposed to with non-maser radiation. Most radiative transfer codes are not designed to handle negative optical depths and source functions, as is the case with masers. Additionally, maser radiation has tightly focused beams, necessitating finer angular resolution compared to non-maser rays. The coherent nature of maser radiation deviates from Gaussian statistics, demanding consideration of maser saturation in the semi-classical approximation (Trung, 2009; Gray, 2012). Full numerical solutions accounting for frequency-dependent radiative transport and molecular thermal motion of molecules have only been applied to simple geometries (see Watson and Wyld (2003)). The presence of magnetic fields further complicates computations by causing splitting and polarization of the maser lines (Sobolev & Gray, 2012).

Considering the aforementioned points, the non-numerical solution to the radiative transfer equation presented in this thesis evidently lacks optimal precision. However, it was the most computationally and time-efficient approach to derive a theoretical model for use in this work. Having acknowledged this, more compromises could have been made to incorporate numerical elements into the solution, though it would have required more time spent researching relevant data.

The main takeaway from this discussion of theoretical modelling can be summarized as encouraging further works to seek numerical solutions using semi-classical maser theory - adopting as many elements from the fully quantum-mechanical model as possible. In an instance where the sole purpose of the research is to create the theoretical model, it would be more viable to incorporate all of the points of improvement discussed in this

section. The theoretical modelling process presented in this thesis is a very simplified model designed to be easily implemented. Due to the scope of this work, it was not feasible to attempt a full-scale modelling endeavour that would incorporate all the optimized suggestions. Instead, a stripped-back version of the modelling recommended by Sobolev and Gray (2012) was attempted. The main facets of model input were considered in an elementary way, using generalized assumptions about the physical conditions of the maser source. However, to improve the robustness and accuracy of the model (and of the subsequent data fitting and results) it is recommended that as much detail is included in the theoretical formulation as possible; reliant upon time and computational constrictions.

5.3 Improving the Observations

Regarding the observations carried out in this work, there are a few suggestions that could improve the quality and versatility of the observational data. The first is that the observation be taken over a longer exposure time. A longer exposure time would increase the signal-to-noise ratio (SNR), allowing for improved sensitivity when detecting the lower-intensity spectral features. In doing so, the wide, low-amplitude pedestal feature may be better recorded (if it is truly present) in the observation.

In the same vein, VLBI (Very Long Baseline Interferometry) could potentially be incorporated as a means of increasing the SNR and angular resolution, as well as studying the kinematics and dynamics of maser-emitting regions. By analyzing Doppler shifts in various parts of a maser, we can extract information about the movements and structures within these regions. This data can potentially enhance the understanding of the maser source's geometry (such as the distribution of masing spots), which can then be integrated into the theoretical model.

Another major improvement would be obtaining observations of multiple maser sources. Attempts to do so were made in this work but were not fruitful due to unknown (likely technical) reasons. In an ideal situation, these observations would have been redone, but due to time constraints and limited observatory access at the time, this was not possible in this instance. It is recommended, however, that if one were to undertake a similar research project, completing the analysis on multiple maser sources would be valuable in testing the proposed methodology.

When selecting additional sources, it would be beneficial to choose sources with historically simple spectra. Specifically, sources with maser spectra that have at least one prominent main feature. Maser sources with documented parameter data values (such as optical depth) would also be highly valuable in validating the results of the spectral analysis.

5.4 Future Work

For future research, whether as a continuation or departure from this thesis, the following recommendations are proposed. Building upon this thesis, the next phase involves revisiting the entire process and integrating as many of the suggested improvements as possible. This thesis forms the foundation for the research to be strengthened and expanded upon.

A more numerical approach should be taken in the theoretical modelling process. While adhering closely to semi-classical maser theory, molecular data, and parameter value estimates should be incorporated when attempting to solve the maser radiative transfer equation. This approach aims to facilitate the calculation of numerical solutions for the radiative transfer equation, avoiding the need for extra assumptions and simplifications required for an analytical solution. Here, reference should be made to Trung (2009),

Gray (2012), Cragg et al. (2005), Sobolev and Deguchi (1994), Sobolev and Gray (2012), and the works cited within.

Using the improved theoretical model, the fit of the Gaussian approximations can be tested on the new theoretical maser spectra. If the results show that the theoretical data is still well described by the sum of a number of Gaussians, then no revisions will need to be made to the observational data fitting approach. If the altered theoretical model produces a spectrum that is not well fit by Gaussians, then other curve-fitting avenues will need to be explored, for example, a Gaussian/Lorentzian hybrid (Voigt profile). Ideally, the Gaussian approximations will still be applicable, and they can be used to highlight the presence (or lack thereof) of the pedestal feature.

When undertaking the observations, a variety of sources should be observed with longer exposure times, and the possible addition of VLBI to enable kinematic measurements. Extra processing steps should be taken to calculate the true spectral flux density values of the maser sources, as opposed to normalizing the data to an estimated average. The same applies to the radial and line-width velocities.

The analysis of the observed data can largely remain unchanged. This includes fitting Gaussians or any chosen approximation, determining the presence of a pedestal feature, calculating ratios of Gaussian amplitude and width parameters along with their respective errors, and finally, estimating optical depth and potentially other relevant physical parameters. Other statistical measures should be employed in evaluating the validity of the Gaussian fit approximations against the observed data, as well as exploring other error statistics for the parameter extractions.

There an element of asymmetry, seen in both the main features of the G9.62 + 0.19E spectrum, that has not been fully explored in this work. The two profiles are asymmetric towards the low frequency side (Figure 3.15). The asymmetry being present in both

main features indicates that this is intrinsic to the maser. Spectral asymmetry has been documented predominantly within OH (Szymczak, 1989) and H_2O masers (Maoz & McKee, 1998; Nesterenok & Varshalovich, 2010), though the conditions that effect the asymmetry in these maser species may also be present on methanol masers. A very simple summary of these sources is that the asymmetry of the maser profiles seem to arise due to density fluctuations within circumstellar envelopes (Szymczak, 1989), rapidly rotating circumnuclear disks (Maoz & McKee, 1998), and the hyperfine splitting of signal levels (Nesterenok & Varshalovich, 2010). While it appears that asymmetry in maser spectra across multiple features is not uncommon, and may be a general phenomenon (Maoz & McKee, 1998), there does not seem to be a single cause that has been identified across multiple maser species.

In future work it would be a worthwhile endeavour to dive deeper into the topic of maser asymmetry by looking closely at the literature referenced above, as well as searching for more reported instances of asymmetry. The asymmetry of the spectrum of G9.62 + 0.19E could be better defined by folding the main spectral features and subtracting it from the data. The analysis process could then be carried out on the folded profile and compared against the original spectrum.

Chapter 6

Conclusion

In this thesis, we present a case study of class II methanol maser source G9.62 + 0.19E, involving theoretical modelling, observations of the source, data processing, and spectral analysis. This was done with the intent of extracting information about the physical conditions of the maser source from its spectrum.

Both standard (classical) and semi-classical variations of maser theory were investigated in the process of constructing a model to produce a theoretical maser spectrum. We derived a simplified form of the radiative transfer equation of an unsaturated maser. Using this equation, we numerically generated maser spectral lines for a range of optical depth values.

The main feature of this spectrum would be used to represent the spectral peak at 6.668 GHz for the methanol maser emission. Using the theoretical model spectra as a guide, Gaussian curves were fit to the spectra based on the works of Watson (2002) and Nesterenok (2016) citing that maser spectra were well approximated by a single Gaussian. Here, iterations of two and three Gaussians were fit to the theoretical spectra of varying optical depths, where the sum of the Gaussians serves as the overall line

approximation. In both instances of the two and three-Gaussian fits, what we have called a "pedestal" feature is visible. The pedestal feature is a Gaussian of relatively low amplitude and broad width when compared to the other Gaussian counterparts.

The appearance of the pedestal feature seemingly changed alongside the different values for optical depth, indicating that there may be some relationship between the two. To further investigate the potential correlation, the ratios of the width and amplitudes of the pedestal feature to that of the sum of the Gaussians were calculated and plotted against the range of optical depth values. This was done for both the two and three-Gaussian fits, and the plots showed that there seemed to be an observable non-linear relationship between the behaviour of the parameters of the pedestal Gaussian and the increase in optical depth.

To further investigate the legitimacy of the pedestal feature, the multiple-Gaussian approximations were used to fit the observed maser spectrum of G9.62 + 0.19E. We conducted these observations using the 30-meter radio telescope at Warkworth, New Zealand. The observed data was then processed within MATLAB, using a multiple frequency switching technique to reduce the baseline fluctuations of the spectrum.

The observed spectrum represents the sum of the spectral lines of the maser source, sitting on top of the instrumental continuum (telescope SEFD plus telescope gain as the function of frequency). We investigated two methods for the removal of the instrumental continuum. One was a widely used subjective method of polynomial removal. The second method, the multiple frequency switching (MFS), was earlier investigated with respect to radio recombination lines by Alexander and Gulyaev (2012).

Here we demonstrated that the MFS method is more objective, and in contrast to the standard polynomial removal it allows for preserving a feature that otherwise would be completely lost – the wide pedestal predicted by our theoretical modelling.

After using the MFS method, the main spectral feature in the observed spectrum of G9.62 + 0.19E was isolated and investigated. Gaussian fitting was applied which demonstrated the presence of a wide pedestal. We calculated the ratios between the amplitudes and widths of both the strong, narrow line and the weak, wide pedestal in the case of G9.62 + 0.19E. Using the plots of the theoretical ratios against the optical depths we pre-calculated earlier, we estimated the optical depth of the main (1.27 km/s) feature of the G9.62 + 0.19E spectrum being formed in the molecular cloud to be within the range of optical depth $\tau = 4 \rightarrow 6$.

Finally, the effectiveness of this research design was discussed, with potential improvements and recommendations for future work being outlined. The concept of fitting multiple Gaussians to the observed spectrum of a cosmic maser source appears to be a useful means of simple approximation. However, the existence and means of identification of the "pedestal" feature remain largely unsubstantiated. This, however, serves as the basis for the continuation of the work presented in this thesis. The usefulness of the pedestal feature in extracting information about the physical conditions of the maser source would be interesting to explore further. The optical depth estimates provided in this work are crude but could act as inspiration for the possible use cases of multiple-Gaussian modelling.

In summary, a novel, independent method has been proposed for the determination of the optical depth of maser sources, and a case study was conducted. To verify the method proposed here, further study should include more refined numerical modelling as well as observations of other maser sources.

References

Alcock, C. & Ross, R. R. (1985). Saturation and beaming in astrophysical masers. *The Astrophysical Journal*, *290*, 433-444. doi: 10.1086/163001

Alexander, J. & Gulyaev, S. (2012). On the apparent narrowing of radio recombination lines at high principal quantum numbers. *The Astrophysical Journal*, *745*, 6. doi: 10.1088/0004-637X/745/2/194

Anderson, N. & Watson, W. (1993). *Line profiles in masers: Velocity relaxation* (Vol. 412). Springer. doi: \url{https://doi.org/10.1007/3-540-56343-1_205}

Araya, E. D., Hofner, P., Goss, W. M., Kurtz, S., Richards, A. M. S., Linz, H., ... Sewiło, M. (2010). Quasi-periodic formaldehyde maser flares in the massive protostellar object iras 18566+0408. *The Astrophysical Journal Letters*, *717*, L133-L137. doi: 10.1088/2041-8205/717/2/L133

Bell, B. M. (1997). A technique for removing strong continuum-related baseline structure from single-dish spectra without fitting sinusoids or polynomials. *Publications of the Astronomical Society of the Pacific*, *109*, 609-613. doi: 10.1086/133919

Boyd, R. (2015). Charles h. townes (1915–2015). *Nature*, *519*, 292. doi: 10.1038/519292a

Carraro, G. (2021). *Astrophysics of the interstellar medium*. Springer Cham. doi: \url{https://doi.org/10.1007/978-3-030-75293-4}

Caswell, J. L., Vaile, R. A., Ellingsen, S. P. & Norris, R. P. (1995). Galactic methanol masers at 12 ghz. *Monthly Notices of the Royal Astronomical Society*, *274*, 1126-1152. doi: 10.1093/mnras/274.4.1126

Cheung, A. C., Rank, D. M., Townes, C. H., Thornton, D. D., Welch, W. J. & Crowther, J. H. (1969). Detection of water in interstellar regions by its microwave radiation. *Nature*, *221*, 626-628. doi: 10.1038/221626a0

Cragg, D. M., Sobolev, A. M. & Godfrey, P. D. (2002). Modelling methanol and hydroxyl masers in star-forming regions. *Monthly Notices of the Royal Astronomical Society*, *331*, 521–536. doi: 10.1046/j.1365-8711.2002.05226.x

Cragg, D. M., Sobolev, A. M. & Godfrey, P. D. (2005). Models of class ii methanol masers based on improved molecular data. *Monthly Notices of the Royal Astronomical Society*, *360*, 533–545. doi: \url{https://doi.org/10.1111/j.1365-2966.2005.09077.x}

Deguchi, S. & Watson, W. D. (1990). Linearly polarized radiation from astrophysical

masers due to magnetic fields when the rate for stimulated emission exceeds the zeeman frequency. *The Astrophysical Journal*, *354*, 649. doi: 10.1086/168722

Dirac, P. A. M. (1927). The quantum theory of the emission and absorption of radiation. *The Royal Society*, *114*, 243–265. doi: \url{https://doi.org/10.1098/rspa.1927.0039}

Einstein, A. (1917). Zur quantentheorie der strahlung (on the quantum theory of radiation). *Physikalische Zeitschrift*, *18*, 121-128.

Garay, G., Rodriguez, L. F., Moran, J. M. & Churchwell, E. (1993). Vla observations of strong iras point sources associated with compact h ii regions. *The Astrophysical Journal Letters*, *418*, 368. doi: 10.1086/173396

Ginsburg, A. & Goddi, C. (2019). First detection of cs masers around a high-mass young stellar object w51 e2e. *The Astronomical Journal*, *158*, 208. doi: 10.3847/1538-3881/ab4790

Goddi, C., Moscadelli, L. & Sanna, A. (2011). Infall and outflow within 400 au from a high-mass protostar. 3d velocity fields from methanol and water masers in aflg 5142. *Astronomy & Astrophysics*, *535*, L8. doi: 10.1051/0004-6361/201117854

Goedhart, S., Gaylard, M. J. & van der Walt, D. J. (2003). Periodic flares in the methanol maser source g9.62+0.20e. *Monthly Notices of the Royal Astronomical Society*, *339*, L33-L36. doi: \url{https://doi.org/10.1046/j.1365-8711.2003.06426.x}

Goedhart, S., Maswanganye, J. P., Gaylard, M. J. & van der Walt, D. J. (2014). Periodicity in class ii methanol masers in high-mass star-forming regions. *Monthly Notices of the Royal Astronomical Society*, *437*, 1808-1820. doi: 10.1093/mnras/stt2009

Goldreich, P. & Keeley, D. A. (1972). Astrophysical masers. i. source size and saturation. *The Astrophysical Journal*, *174*, 517-525. doi: 10.1086/151514

Goldreich, P., Keeley, D. A. & Kwan, J. Y. (1973). Astrophysical masers. 11. polarization properties. *The Astrophysical Journal*, *179*, 111-134. doi: 10.1086/151852

Goldreich, P. & Kwan, J. Y. (1974). Astrophysical masers. iv. line widths. *The Astrophysical Journal*, *190*, 27-34. doi: 10.1086/152843

Gray, M. D. (2012). *Maser sources in astrophysics*. New York, NY: Cambridge University.

Green, J. A., Caswell, J. L., Fuller, G. A., Avison, A., Breen, S. L., Ellingsen, S. P., ... Voronkov, M. A. (2010). The 6-ghz methanol multibeam maser catalogue – ii. galactic longitudes $6^o \breve{}\, 20^o$. *Monthly Notices of the Royal Astronomical Society*, *409*, 913-935. doi: \url{https://doi.org/10.1111/j.1365-2966.2010.17376.x}

Hecht, J. (2021). *Laser*. `https://www.britannica.com/technology/laser`.

Hilborn, R. C. (1982). Einstein coefficients, cross sections, f values, dipole moments, and all that. *American Journal of Physics*, *50*, 982-986.

Himwich, E. (2000). Introduction to the field system for non-ssers. *International VLBI Services (IVS) 2000 General Meeting Proceedings*, 86-90. https://ivscc.gsfc.nasa.gov/publications/gm2000/himwich2.pdf.

Himwich, E. & Vandenberg, N. R. (2001). *Snap commands - operation manual (version 9.5)*. NASA/Goddard Space Flight Center Space Geodesy Program.

Houghton, S. & Whiteoak, J. B. (1995). The small-scale distribution of emission from the 6.7-ghz transition of methanol in sgr b2. *Monthly Notices of the Royal Astronomical Society*, *273*, 1033-1040. doi: 10.1093/mnras/273.4.1033

Inayoshi, K., Sugiyama, K., Hosokawa, T., Motogi, K. & Tanaka, K. E. I. (2013). Direct diagnostics of forming massive stars: Stellar pulsation and periodic variability of maser sources. *The Astrophysical Journal Letters*, *769*, L20. doi: 10.1088/2041-8205/769/2/L20

Institute for Radio Astronomy & Space Research (IRASR). (2022). *Radio telescopes.* `https://irasr.aut.ac.nz/radio-telescopes`.

Kaplan, S. A. & Pikelner, S. B. (1970). *The interstellar medium*. Harvard University Press.

Kwok, S. (2007). *Physics and chemistry of the interstellar medium*. University Science Books.

Ladeyschikov, D. A., Bayandina, O. S. & Sobolev, A. M. (2019). Online database of class i methanol masers. *The Astronomical Journal*, *158*, 233. doi: 10.3847/1538-3881/ab4b4c

Lankhaar, B. & Vlemmings, W. (2019). Characterizing maser polarization: Effects of saturation, anisotropic pumping, and hyperfine structure. *Astronomy & Astrophysics*, *628*. doi: \url{https://doi.org/10.1051/0004-6361/201935064}

Litvak, M. M. (1970). Linewidths of a gaussian broadband signal in a saturated two-level system. *Physical Review. A, General physics*, *2*, 2107.

Litvak, M. M. (1971). The meaning of the $oh - h_2o$ maser maps. *The Astrophysical Journal*, *170*, 71-80. doi: 10.1086/151189

Litvak, M. M. (1973). Radiative transport in interstellar masers. *The Astrophysical Journal*, *182*, 711-730. doi: 10.1086/152179

MacLeod, G. C., Chibueze, J. O., Sanna, A., Paulsen, J. D., Houde, M., van den Heever, S. P. & Goedhart, S. (2020). Systematic velocity drifts of methanol masers associated with g9.62+0.20e. *Monthly Notices of the Royal Astronomical Society*, *500*, 3425-3437. doi: \url{https://doi.org/10.1093/mnras/staa3467}

Maoz, E. & McKee, C. F. (1998). Doppler shift asymmetry in high-velocity maser emission from shocks in circumnuclear disks. *The Astrophysical Journal*, *494*, 218-235. doi: 10.1086/305186

MathWorks. (2023). *Matlab.* `https://au.mathworks.com/products/matlab.html?s_tid=hp_products_matlab`.

Matthews, L. D., Greenhill, L. J., Goddi, C., Chandler, C. J., Humphreys, E. M. L. & Kunz, M. W. (2010). A feature movie of sio emission 20-100 au from the massive young stellar object orion source i. *The Astrophysical Journal*, *708*, 80-92. doi: 10.1088/0004-637X/708/1/80

McQuarrie, D. A. (2000). *Statistical mechanics*. Sausalito, CA: University Science Books.

Menegozzi, L. N. & Lamb, J., W. E. (1978). Intensity fluctuations in a two-mode ring laser. *Physical Review A (General Physics)*, *17*, 694-700. doi: 10.1103/PhysRevA.17.701

Morgan, G. G. & Kühne, I. A. (2020). *Chapter 3 - molecular magnetochemistry*. Elsevier. doi: \url{https://doi.org/10.1016/B978-0-444-64225-7.00003-1}

National Radio Astronomy Observatory. (2023). *Grote reber's first radio telescope.* `https://public.nrao.edu/gallery/grote-rebers-first-radio-telescope/`.

Natusch, T. S. L. (2015). *Autocorrelating mark5 recorded data using m5spec.* Auckland, New Zealand.

Natusch, T. S. L. (2020). *Lecture on radio receiving systems.* Auckland, New Zealand.

Nesterenok, A. V. (2016). Modelling ch_3oh masers: Sobolev approximation and accelerated lambda iteration method. *Monthly Notices of the Royal Astronomical Society*, *455*, 3978–3985. doi: doi:10.1093/mnras/stv2594

Nesterenok, A. V. (2022). Modelling cosmic masers in c-type shock waves – the coexistence of class i ch_3oh and 1720 mhz oh masers. *Monthly Notices of the Royal Astronomical Society*, *509*, 4555-4572. doi: 10.1093/mnras/stab3303

Nesterenok, A. V. & Varshalovich, D. A. (2010). Asymmetry in the spectrum of high-velocity h2o maser emission features in active galactic nuclei. *Astronomy Letters*, *36*, 1-6. doi: \url{https://doi.org/10.1134/S1063773710010019}

NobelPrize.org. (2023). *The nobel prize in physics 1964.* `https://www.nobelprize.org/prizes/physics/1964/summary/`.

Parfenov, S. Y. & Sobolev, A. M. (2014). On the class ii methanol maser periodic variability due to the rotating spiral shocks in the gaps of discs around young binary stars. *Monthly Notices of the Royal Astronomical Society*, *444*, 620-628. doi: \url{https://doi.org/10.1093/mnras/stu1481}

Paschotta, R. (2008). Four-level and three-level gain media. *RP Photonics Encyclopedia*. `https://www.rp-photonics.com/four_level_and_three_level_laser_gain_media.html`.

Pestalozzi, M. R., Minier, V. & Booth, R. S. (2005). A general catalogue of 6.7-ghz methanol masers - i. data. *Astronomy & Astrophysics*, *432*, 737-742. doi: \url{https://doi.org/10.1051/0004-6361:20035855}

Petasis, D. T. & Hendrich, M. P. (2015). *Chapter eight - quantitative interpretation of multifrequency multimode epr spectra of metal containing proteins, enzymes, and biomimetic complexes* (Vol. 563). Academic Press. doi: \url{https://doi.org/10.1016/bs.mie.2015.06.025}

Rabli, D. & Flower, D. R. (2010). The rotational structure of methanol and its excitation by helium. *Monthly Notices of the Royal Astronomical Society*, *403*, 2033-2040. doi: 10.1111/j.1365-2966.2010.16240.x

Reid, M. J., Haschick, A. D., Burke, B. F., Moran, J. M., Johnston, K. J., Swenson, G. W. & Jr. (1980). The structure of interstellar hydroxyl masers - vlbi synthesis observations of $w_3(oh)$. *The Astrophysical Journal*, *239*, 89-99. doi: 10.1086/158092

Reid, M. J., Muhleman, D. O., Moran, J. M., Johnston, K. J. & Schwartz, P. R. (1977). The structure of stellar hydroxyl masers. *The Astrophysical Journal*, *214*, 60-77. doi: 10.1086/155230

Robinson, B. J. (1964). Receivers for cosmic radio waves. *Annual Review of Astronomy and Astrophysics*, *2*, 401. doi: 10.1146/annurev.aa.02.090164.002153

Sanna, A., Menten, K. M., Carrasco-González, C., Reid, M. J., Ellingsen, S. P., Brunthaler, A., ... Krishnan, V. (2015). The environment of the strongest galactic methanol maser. *The Astrophysical Journal Letters*, *804*, L2. doi: 10.1088/2041-8205/804/1/L2

Schawlow, A. L. & Townes, C. H. (1958). Infrared and optical masers. *Physical Review Journals Archive*, *112*, 1940-1949. doi: 10.1103/PhysRev.112.1940

Sobolev, A. M., Cragg, D. M., Ellingsen, S. P., Gaylard, M. J., Goedhart, S., Henkel, C., ... Voronkov, M. A. (2007). Astrophysical masers and their environments: How do methanol masers manage to appear in the youngest star vicinities and isolated molecular clumps. *International Astronomical Union Symposia*, *242*, 81-88. doi: 10.1017/S1743921307012616

Sobolev, A. M. & Deguchi, S. (1994). Pumping of class ii methanol masers. *Astronomy & Astrophysics*, *291*, 569-576.

Sobolev, A. M. & Gray, M. D. (2012). Modelling of cosmic molecular masers: Introduction to a computation cookbook. *Cosmic Masers - from OH to H0*, *287*, 13-22. doi: 10.1017/S1743921312006588

Strel'nitskii, V. S. (1977). The role of dust in the pumping of cosmic masers. *Soviet Astronomy*, *21*, 381-385.

Strel'nitskii, V. S. (1981). An interpretation of the 1.2-cm methanol emission in orion. *Soviet Astronomy Letters*, *7*, 223-228.

Sugiyama, K., Yonekura, Y., Motogi, K., Saito, Y., Fujisawa, K., Ishii, S., ... Inayoshi, K. (2015). Flux monitoring of 6.7 ghz methanol maser to systematically research periodic variations using the hitachi 32-m. *Publications of the Korean Astronomical Society*, *30*, 129-131. doi: 10.5303/PKAS.2015.30.2.129

Svelto, O. (1998). *Principles of lasers*. New York, NY: Springer.

Szymczak, M. (1989). Asymmetric circumstellar oh maser emission: effect of density fluctuations. *Monthly Notices of the Royal Astronomical Society*, *237*, 561-568. doi: \url{https://doi.org/10.1093/mnras/237.3.561}

Szymczak, M., Olech, M., Sarniak, R., Wolak, P. & Bartkiewicz, A. (2017). Monitoring observations of 6.7 ghz methanol masers. *Monthly Notices of the Royal Astronomical Society*, *474*, 219-253. doi: 10.1093/mnras/stx2693

Tielens, A. G. G. M. (2005). *The physics and chemistry of the interstellar medium*. Cambridge: Cambridge University Press. doi: 10.1017/CBO9780511819056

Trung, D. V. (2009). On the theory of astronomical masers – i. statistics of maser radiation. *Monthly Notices of the Royal Astronomical Society*, *396*, 2319-2331. doi: 10.1111/j.1365-2966.2009.14901.x

van den Heever, S. P., van der Walt, D. J., Pittard, J. M. & Hoare, M. G. (2019). Periodic methanol masers: from a colliding wind binary (cwb) perspective. *Monthly Notices of the Royal Astronomical Society*, *485*, 2759–2771. doi: \url{https://doi.org/10.1093/mnras/stz576}

van der Walt, D. J. (2011). On the methanol masers in g9.62+0.20e and g188.95+0.89. *The Astronomical Journal*, *141*, 6. doi: 10.1088/0004-6256/141/5/152

van der Walt, D. J., Goedhart, S. & Gaylard, M. J. (2009). Periodic class ii methanol masers in g9.62+0.20e. *Monthly Notices of the Royal Astronomical Society*, *398*, 961-970. doi: \url{https://doi.org/10.1111/j.1365-2966.2009.15147.x}

van der Walt, D. J., Maswanganye, J. P., Etoka, S., Goedhart, S. & van den Heever, S. P. (2016). Periodic methanol masers in g9.62+0.20e. *Astronomy & Astrophysics*, *588*, 5. doi: 10.1051/0004-6361/201527611

Vlemmings, W. H. T., Torres, R. M. & Dodson, R. (2011). Zeeman splitting of 6.7 ghz methanol masers on the uncertainty of magnetic field strength determinations. *Astronomy & Astrophysics*, *529*. doi: 10.1051/0004-6361/201116648

Voronkov, M. A., Brooks, K. J., Sobolev, A. M., Ellingsen, S. P., Ostrovskii, A. B. & Caswell, J. L. (2006). Class i methanol masers in the outflow of iras16547-4247. *Monthly Notices of the Royal Astronomical Society*, *373*, 411-424. doi: 10.1111/j.1365-2966.2006.11047.x

Voronkov, M. A., Sobolev, A. M., Ellingsen, S. P., Ostrovskii, A. B. & Alakoz, A. (2005). Maser action in methanol transitions. *Astrophysics and Space Science*, *295*, 217-223. doi: 10.1007/s10509-005-3692-z

Walker, R. C. (2023). *The sched user manual.* `https://www.aoc.nrao.edu/software/sched/`.

Watson, W. D., Sarma, A. P. & Singleton, M. S. (2002). Gaussian spectral line profiles of astrophysical masers. *The Astrophysical Journal*, *570*, L37-L40. doi: 10.1086/340833

Watson, W. D. & Wyld, H. W. (2003). Apparent sizes and spectral line profiles for spherical and disk masers: Solutions to the full equations. *The Astrophysical Journal*, *598*, 357–368. doi: 10.1086/378718

Weaver, H., Williams, D. R. W., Dieter, N. H., & Lum, W. T. (1965). Observations of a strong unidentified microwave line and of emission from the oh molecule. *Nature*, *208*, 29-31. doi: 10.1038/208029a0

Williams, M. (2015). *Nebulae: What are they and where do they come from?* `https://www.universetoday.com/61103/what-is-a-nebula/#:~:text=History%20of%20Nebula%20Observation%3A,appeared%20nebulous%20in%20his%20book`.

Appendix A

Additional Eight-Gaussian Fit

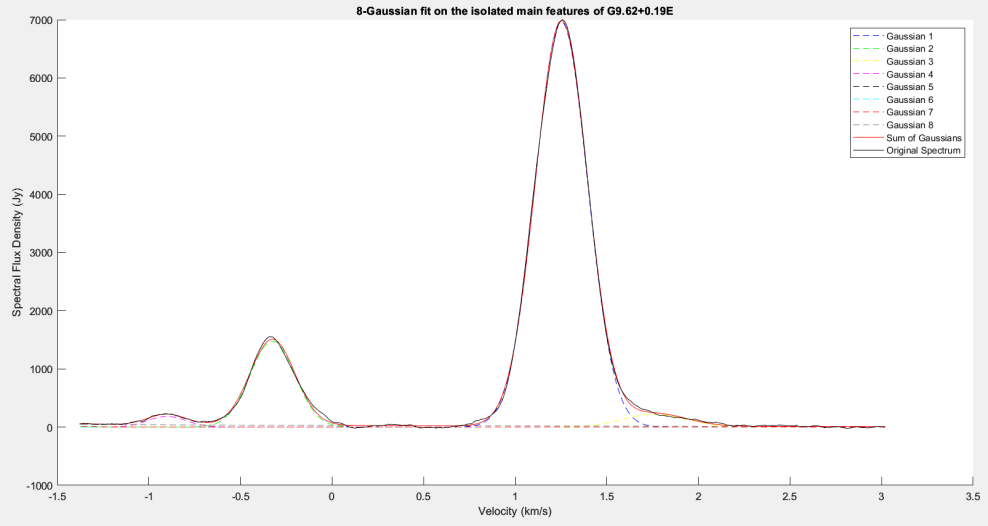

Figure A.1: Result of fitting eight Gaussians to the observed spectrum for methanol maser G9.62 + 0.19E.

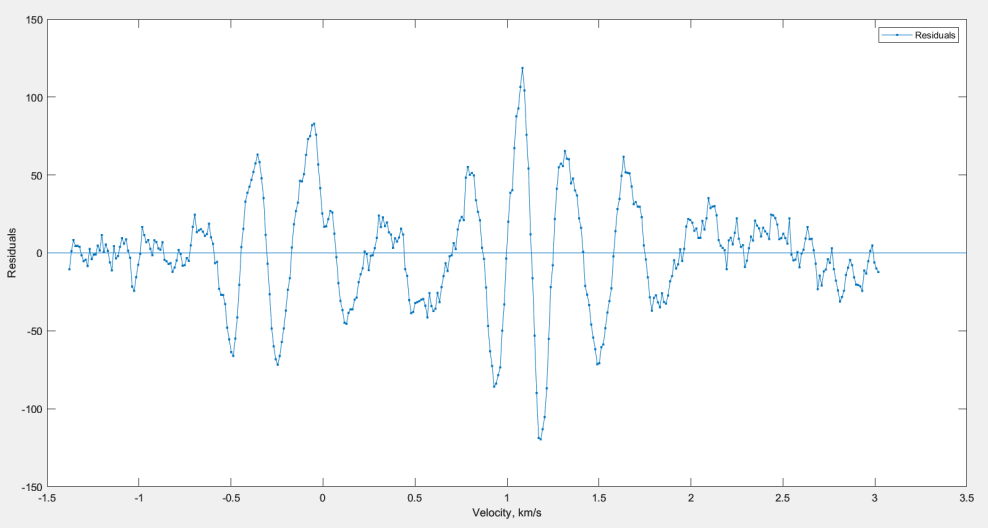

Figure A.2: Residuals from the eight Gaussian approximation of the observed spectrum of G9.62 + 0.19E

Appendix B

MATLAB Code

B.1 Theoretical modelling

B.1.1 Maser Line Model + Ratio Plots

```
clear all
Nu=linspace(-2.5,2.5,501); % Frequencies in Doppler widths
Gs=exp(-Nu.^2);
n=101; %integration steps
R=linspace(0,1,n); % Relative radius of the globule
w=sqrt(1-R.^2); % weight from Pythagoras

j1=1;
j2=20;
m=1;
for j=j1:1:j2
    tau=j*m; % Optical depth through the centre (negative abs coeff
```

```
    I=0;
for i=1:1:n
    I=I+R(i)*exp(tau*w(i).*Gs);
end
I=I-n/2;

% One Gaussian fit. Output: Amplitude, Width
f1 = fit(Nu',I','gauss1');
cValues1 = coeffvalues(f1);
Amplitude(j)=cValues1(1);
width(j)=cValues1(3);

% Three Gaussians fitting. Amplitude1,2,3; Width1,2,3
f3 = fit(Nu',I','gauss3');
cValues3 = coeffvalues(f3);
Amplitude1(j)=cValues3(1);
width1(j)=cValues3(3);
Amplitude2(j)=cValues3(4);
width2(j)=cValues3(6);
Amplitude3(j)=cValues3(7);
width3(j)=cValues3(9);

if j == j2
    hold off
end

a1=cValues3(1);
```

```
b1=cValues3(2);
c1=cValues3(3);

a2=cValues3(4);
b2=cValues3(5);
c2=cValues3(6);

a3=cValues3(7);
b3=cValues3(8);
c3=cValues3(9);

coefficients = [a1, b1, c1; a2, b2, c2; a3, b3, c3];

% Extract and sort coefficients based on the first column (amplitude
[sortedAmplitudes, sortIndex] = sort(coefficients(:, 3), 'descend')
sortedCoefficients = coefficients(sortIndex, :);

% Extract sorted coefficients
a1 = sortedCoefficients(1, 1);
b1 = sortedCoefficients(1, 2);
c1 = sortedCoefficients(1, 3);
gauss_1=a1.*exp(-((Nu-b1)./c1).^2);
a2 = sortedCoefficients(2, 1);
b2 = sortedCoefficients(2, 2);
c2 = sortedCoefficients(2, 3);
gauss_2=a2.*exp(-((Nu-b2)./c2).^2);
a3 = sortedCoefficients(3, 1);
```

```
b3 = sortedCoefficients(3, 2);
c3 = sortedCoefficients(3, 3);
gauss_3=a3.*exp(-((Nu-b3)./c3).^2);

A1(j)=a1;
A2(j)=a2;
A3(j)=a3;
W1(j)=c1;
W2(j)=c2;
W3(j)=c3;

% Plot result of two-Gauss fitting
figure
plot(f3,Nu,I)
hold on
plot(Nu,gauss_2+gauss_3, Nu, gauss_1,'g-')
legend('Data', 'Gaussian 1', 'Gaussian 2');
text(0.05, 0.95, ['tau = ' num2str(tau)], 'Units', 'normalized', 'F

% Plot result of three-Gauss fitting
figure;
plot(f3,Nu,I)
hold on
plot(Nu,gauss_2,Nu,gauss_3,Nu,gauss_1,'g-')
legend('Data', 'Gaussian 1', 'Gaussian 2', 'Gaussian 3');
text(0.05, 0.95, ['tau = ' num2str(tau)], 'Units', 'normalized', 'F
end
```

```
hold off


x = j1:j2;
x = m*x;
Y=A1./Amplitude;
y=W1./width;

% Indices to exclude
indices_to_exclude = [12];

% Exclude specified points from x and y
x_modified = x(~ismember(x, indices_to_exclude));
y_modified = y(~ismember(x, indices_to_exclude));
Y_modified = Y(~ismember(x, indices_to_exclude));

width_modified = width([1:indices_to_exclude-1, indices_to_exclude+
Amplitude_modified = Amplitude([1:indices_to_exclude-1, indices_to_

W1_modified = W1([1:indices_to_exclude-1, indices_to_exclude+1:end]
W2_modified = W2([1:indices_to_exclude-1, indices_to_exclude+1:end]
W3_modified = W3([1:indices_to_exclude-1, indices_to_exclude+1:end]
A1_modified = A1([1:indices_to_exclude-1, indices_to_exclude+1:end]
A2_modified = A2([1:indices_to_exclude-1, indices_to_exclude+1:end]
A3_modified = A3([1:indices_to_exclude-1, indices_to_exclude+1:end]


figure
```

```
plot(x_modified,log10(Amplitude_modified))
hold on
plot(x_modified,log10(A1_modified),'g')
plot(x_modified,log10(A2_modified), 'r')
plot(x_modified,log10(A3_modified), 'm')
legend('Sum of Gaussians', 'Gaussian 1', 'Gaussian 2', 'Gaussian 3'
xlabel('Optical depth (\tau)');
ylabel('Log Amplitude');
title('Log of Amplitude of Gaussians');
hold off

figure
plot(x_modified,width_modified)
hold on
plot(x_modified,W1_modified,'g')
plot(x_modified,W2_modified,'r')
plot(x_modified,W3_modified,'m')
legend('Data', 'Gaussian 1', 'Gaussian 2', 'Gaussian 3');
xlabel('Optical depth (\tau)');
ylabel('Width (Doppler widths)');
title('Widths of Gaussians');
hold off

% Plot the modified data
figure
plot(x_modified, Y_modified);
xlabel('Optical depth (\tau)');
```

```
ylabel('Pedestal amplitude / Gaussian sum amplitude');
title('Ratio: Pedestal amplitude over the amplitude of the Gaussian
ylim([0 .45]);

% Plot the modified data
figure
plot(x_modified, y_modified);
xlabel('Optical depth (\tau)');
ylabel('Pedestal width / Gaussian sum width');
title('Ratio: Pedestal width over the width of the Gaussian sum');
ylim([1 2]);

figure
plot(x_modified, y_modified);
hold on
plot(x_modified, Y_modified);

% Define upper and lower error limits along the x-axis for the first
lower_limit_1 = 1.4710 - 0.3423;
upper_limit_1 = 1.4710 + 0.3423;

% Define upper and lower error limits along the x-axis for the secon
lower_limit_2 = 0.1182 - 0.0447;
upper_limit_2 = 0.1182 + 0.0447;

% Plot the first set of upper and lower limit lines
plot(x, lower_limit_1*ones(size(x)), 'c--', 'LineWidth', 1);
```

```
plot(x, upper_limit_1*ones(size(x)), 'c--', 'LineWidth', 1);

% Plot the second set of upper and lower limit lines
plot(x, lower_limit_2*ones(size(x)), 'm--', 'LineWidth', 1);
plot(x, upper_limit_2*ones(size(x)), 'm--', 'LineWidth', 1);

% Add vertical lines at x = 4 and x = 6
line([4 4], ylim, 'Color', 'k', 'LineStyle', '--', 'DisplayName', '
line([6 6], ylim, 'Color', 'k', 'LineStyle', '--', 'DisplayName', '



% Shade the area between the first set of lines
fill([x, fliplr(x)], [lower_limit_1*ones(size(x)), fliplr(upper_lim

% Shade the area between the second set of lines
fill([x, fliplr(x)], [lower_limit_2*ones(size(x)), fliplr(upper_lim

xlabel('Optical depth (\tau)');
ylabel('Ratio');
title('Amplitude and Width ratio graphs with shaded error regions')
legend('Amplitude ratio graph', 'Width ratio graph', 'Amplitude rat
hold off;
```

B.2 Data Processing

B.2.1 Loading Data

```
clear data
% Read data from Excel file
[num,~,~] = xlsread('hwg962.xlsx');

% Define the column indices to extract
cols = [2 4]; % initialize with the first two columns
for i = 1:ceil((size(num, 2)-4)/6)
    next_cols = [8+6*(i-1) 10+6*(i-1)]; % compute next pair of colu
    next_cols = next_cols(next_cols <= size(num, 2)); % filter out
    cols = [cols next_cols]; % add next pair of columns to list
end

% Extract the specified columns and save to .mat file
data = num(:, cols);
save('g962_scans.mat', 'data');
```

B.2.2 Frequency Switching

```
clear data;
data=load('g962_scans.mat');
N1 = 32500;
N2 = 34000;
n = N2 - N1;
k1 = 4;
```

```
k2 = (k1 == 3 || k1 == 4) * 2;
total_FF_L_plus_R = zeros(1, n);

for j = 1:2
    FS = data.data(:,j:2:(j+146));
    for k = 1:k1
        FS = FS - circshift(FS, n);
    end
    Freqsw = FS(N1:N2+k1*n-1);
    plot(Freqsw)
    F = FS(N1+k2*n : N2+k2*n-1,:);
    F = F./max(F);
    total_FF = sum(F,2);
    total_FF_L_plus_R = total_FF_L_plus_R + total_FF';
end

figure
plot(total_FF_L_plus_R); % Before smoothing

filter = ones(1,5)/5; % Moving average with window 5
smoothed_total_FF = conv(total_FF_L_plus_R, filter, 'same');

figure
plot(smoothed_total_FF);

% Change to frequency
nu_MHz_0 = 6660;
```

```
nu_N1 = 6660 + N1*16/2^16;
nu_N2 = 6660 + N2*16/2^16;
xaxis = linspace(nu_N1,nu_N2,n);

figure
plot(xaxis,smoothed_total_FF)
xlim([nu_N1 nu_N2]);

% Jansky conversion
max_value = max(smoothed_total_FF(:));  % Find the maximum value in
jansky = (smoothed_total_FF / max_value) * 7000;  % Normalize the d

X_val = xaxis;
Y_val = jansky;

figure
plot(xaxis,jansky);
xlabel('Frequency (MHz)');
ylabel('Spectral Flux Density (Jy)');
title('G9.62+0.19E Spectrum');

% Combine X and Y to form a 2x1500 matrix
whole_spectra_freq = [X_val; Y_val];
save('whole_spectra_freq.mat','whole_spectra_freq');

% Isolate the main features
isolated_spectra = whole_spectra_freq(:, 600:1000);
```

```
figure
plot(isolated_spectra(1,:), isolated_spectra(2,:));
xlabel('Frequency (MHz)');
ylabel('Spectral Flux Density (Jy)');
title('Isolated Main Feature G9.62+0.19E Spectrum');

% Convert to velocity
v_0=6668.148; % We chose it so that the max component has v = 1.25 k
v1 = (v_0-isolated_spectra(1,:))/(v_0)*3e5;

figure
plot(v1,isolated_spectra(2,:));
xlabel('Velocity (km/s)');
ylabel('Spectral Flux Density (Jy)');
title('Isolated Main Feature G9.62+0.19E Spectrum');

% Saving isolated spectra with velocity x-axis values
isolated_spectra_velocity = [v1; isolated_spectra(2,:)];
save('isolated_spectra_velocity.mat','isolated_spectra_velocity');
```

B.2.3 Polynomial Removal

```
% Load the .mat file
clear data;
data=load('g962_scans.mat');
```

```
% Exclude first row
data_subset = data.data(2:65536, :);

% Normalize the data
normalized_data = data_subset/max(data_subset);

% Sum the columns
column_sum = sum(normalized_data, 2);

% Transpose
result_vector = column_sum';

% x axis
N1 = 2;
N2 = 65536;
nu_MHz_0 = 6660;
nu_N1 = 6660 + N1*16/2^16;
nu_N2 = 6660 + N2*16/2^16;
xaxis = linspace(nu_N1,nu_N2,65535);

% Jansky conversion
max_value = max(result_vector(:));  % Find the maximum value in the
jansky = (result_vector/ max_value) * 7000;  % Normalize the dataset

figure;
plot(xaxis,jansky)
```

```
xx = xaxis(33100:33500);
yy = jansky(33100:33500);
mean_xx = mean(xx);

% Centering: Subtract the mean value from all x-axis values:
xx_centered = xx - mean_xx;
% We need "centering", otherwise the polynomial will be "badly condi

% Spectrum
figure
plot(xx,yy)

% Define the window size (e.g., 4 points) and type of smoothing (e.g
window_size = 4;
smoothing_type = 'movmean';

% Apply the smoothing:
smoothed_yy = smoothdata(yy, smoothing_type, window_size);
yy = smoothed_yy;

figure
plot(xx_centered,yy)
[X,Y]=getpts;  % chose points on the continuum spectrum

[p,S1]=polyfit(X,Y,5);
Y1=polyval(p,xx_centered);
figure
```

```
plot(X,Y,'ro')
hold on
plot(xx_centered,Y1)
plot(xx_centered,yy);

yy=yy-Y1;
figure
plot(xx_centered,yy)
hold on
refline(0,0);

% Back to our original x-axis
figure
plot(xx,yy)
hold on
refline(0,0);

% Change to velocity
v_0=6668.148; % We chose it so that the max component has v = 1.25 l
v1 = (v_0-xx)/(v_0)*3e5;
figure
plot(v1,yy)
```

B.3 Gaussian Fits

B.3.1 Eight-Gaussian Approximation

```
function fitEightGaussians()

    load('isolated_spectra_velocity.mat');
    x = isolated_spectra_velocity(1, :);
    y = isolated_spectra_velocity(2, :);

    startPoints = [7000, 1.3, 0.2, 1300, -0.3, 0.2, 240, 1.8, 0.2,

    % Define options for lsqcurvefit
    options = optimoptions('lsqcurvefit', 'MaxFunctionEvaluations',

    % Fit 8 Gaussians
    fittedParams = lsqcurvefit(@eightGaussians, startPoints, x, y,

    % Calculate individual Gaussian components
    numGaussians = 8;
    gaussComponents = zeros(size(x));
    colors = {'b', 'g', 'y', 'm', 'k', 'c', 'r', [0.5 0.5 0.5]};

    figure;
    hold on;

    legendInfo = cell(numGaussians + 1, 1);
```

```
for i = 1:numGaussians
    A = fittedParams(i * 3 - 2);
    mu = fittedParams(i * 3 - 1);
    sigma = fittedParams(i * 3);
    individualGaussian = A * exp(-(x - mu).^2 / (2 * sigma^2));

    % Plot individual Gaussian
    plot(x, individualGaussian, 'Color', colors{i}, 'LineStyle'
    legendInfo{i} = ['Gaussian ', num2str(i)];

    gaussComponents = gaussComponents + individualGaussian;
end

% Plot the sum of all Gaussians
plot(x, gaussComponents, 'r');
plot(x, y, 'k')
xlabel('Velocity (km/s)');
ylabel('Spectral Flux Density (Jy)');
title('8-Gaussian fit on the isolated main features of G9.62+0.

legendInfo{numGaussians + 1} = 'Sum of Gaussians';
legendInfo{numGaussians + 2} = 'Original Spectrum';
legend(legendInfo);
hold off;

% Plot residuals
```

```
    figure;
    plot(x, y - gaussComponents, '.-');
    hold on;
    refline(0, 0);
    ylabel('Residuals');
    xlabel('Velocity (km/s)');
    legend('Residuals');
end

function y = eightGaussians(params, x)
    numGaussians = 8;
    y = zeros(size(x));

    for i = 1:numGaussians
        A = params(i * 3 - 2);
        mu = params(i * 3 - 1);
        sigma = params(i * 3);
        y = y + A * exp(-(x - mu).^2 / (2 * sigma^2));
    end
end
```

B.3.2 Five-Gaussian Approximation

```
function fitFiveGaussians()

    load('isolated_spectra_velocity.mat');
    x = isolated_spectra_velocity(1, :);
```

```
y = isolated_spectra_velocity(2, :);

% Startpoints for 5 Gaussians
startPoints = [5000, 1.25, 0.2, 4500, 1.25, 0.2, 1300, -0.75, 0

% Define options for lsqcurvefit
options = optimoptions('lsqcurvefit', 'MaxFunctionEvaluations',

% Fit 5 Gaussians
fittedParams = lsqcurvefit(@fiveGaussians, startPoints, x, y, [

% Calculate individual Gaussian components
numGaussians = 5;
gaussComponents = zeros(size(x));
colors = {'b', 'g', 'y', 'm', 'k'};

figure;
hold on;

legendInfo = cell(numGaussians + 2, 1);

for i = 1:numGaussians
    A = fittedParams(i * 3 - 2)
    mu = fittedParams(i * 3 - 1)
    sigma = fittedParams(i * 3)
    individualGaussian = A * exp(-(x - mu).^2 / (2 * sigma^2));
```

```
    % Plot individual Gaussian
    plot(x, individualGaussian, '--', 'Color', colors{i});
    xlabel('Velocity (km/s)');
    ylabel('Spectral Flux Density (Jy)');
    title('5-Gaussian fit on the isolated main features of G9.6

    legendInfo{i} = ['Gaussian ', num2str(i)];

    gaussComponents = gaussComponents + individualGaussian;
end

% Plot the sum of the 5 Gaussians
plot(x, gaussComponents, 'r-', 'LineWidth', 0.5);

% Plot the original spectrum
plot(x, y, 'k-', 'LineWidth', 0.5);

legendInfo{numGaussians + 1} = 'Sum of Gaussians';
legendInfo{numGaussians + 2} = 'Original Spectrum';

legend(legendInfo);
hold off;

% Plot residuals
figure;
plot(x, y - gaussComponents, '.-');
hold on;
```

```
    refline(0, 0);
    ylabel('Residuals');
    xlabel('Velocity (km/s)');
    legend('Residuals');
    title('5-Gaussian Approximation Residuals')
end

function y = fiveGaussians(params, x)
    numGaussians = 5;
    y = zeros(size(x));

    for i = 1:numGaussians
        A = params(i * 3 - 2);
        mu = params(i * 3 - 1);
        sigma = params(i * 3);
        y = y + A * exp(-(x - mu).^2 / (2 * sigma^2));
    end
end
```

B.3.3 Three-Gaussian Approximation

```
function fitThreeGaussians()

    load('isolated_spectra_velocity.mat');
    main_feature = isolated_spectra_velocity(:,90:230);
    x = main_feature(1, :);
    y = main_feature(2, :);
```

```
% Startpoints for the 3 Gaussians
startPoints = [4000, 1.25, 0.2, 2500, 1.25, 0.2, 500, 1.25, 0.2

% Define options for lsqcurvefit
options = optimoptions('lsqcurvefit', 'MaxFunctionEvaluations',

% Fit 3 Gaussians
fittedParams = lsqcurvefit(@threeGaussians, startPoints, x, y,

% Calculate individual Gaussian components
numGaussians = 3;
gaussComponents = zeros(size(x));
colors = {'b', 'g', 'y'};

figure;
hold on;

legendInfo = cell(numGaussians + 2, 1);

for i = 1:numGaussians
    A = fittedParams(i * 3 - 2)
    mu = fittedParams(i * 3 - 1)
    sigma = fittedParams(i * 3)
    individualGaussian = A * exp(-(x - mu).^2 / (2 * sigma^2));

    % Plot individual Gaussians
```

```
    plot(x, individualGaussian, '--', 'Color', colors{i});
    xlabel('Velocity (km/s)');
    ylabel('Spectral Flux Density (Jy)');
    title('3-Gaussian fit on the central feature of G9.62+0.19E

    legendInfo{i} = ['Gaussian ', num2str(i)];

    gaussComponents = gaussComponents + individualGaussian;
end

% Plot the sum of the 3 Gaussians
plot(x, gaussComponents, 'r-', 'LineWidth', 0.5);

% Plot the original spectrum
plot(x, y, 'k-', 'LineWidth', 0.5);
legendInfo{numGaussians + 1} = 'Sum of Gaussians';
legendInfo{numGaussians + 2} = 'Original Spectrum';

legend(legendInfo);
hold off;

% Plot residuals
figure;
plot(x, y - gaussComponents, '.-');
hold on;
refline(0, 0);
ylabel('Residuals');
```

```
xlabel('Velocity (km/s)');
legend('Residuals');
title('3-Gaussian Approximation Residuals')

figure;
hold on;

% Plot the original spectrum
plot(x, y, 'k-', 'LineWidth', 0.5);

% Plot the sum of all three Gaussians
plot(x, gaussComponents, 'r-', 'LineWidth', 0.5);

% Sum of 'Gaussian 1' and 'Gaussian 2'
sum12 = fittedParams(1 * 3 - 2) * exp(-(x - fittedParams(1 * 3
        fittedParams(2 * 3 - 2) * exp(-(x - fittedParams(2 * 3
plot(x, sum12, '--', 'Color', colors{1});

% 'Gaussian 3' on its own
A3 = fittedParams(3 * 3 - 2);
mu3 = fittedParams(3 * 3 - 1);
sigma3 = fittedParams(3 * 3);
gaussian3 = A3 * exp(-(x - mu3).^2 / (2 * sigma3^2));
plot(x, gaussian3, '--', 'Color', colors{3});

legend('Original Spectrum', 'Sum of Gaussians', 'Sum of Gaussia
hold off;
```

```
end

function y = threeGaussians(params, x)
    numGaussians = 3;
    y = zeros(size(x));

    for i = 1:numGaussians
        A = params(i * 3 - 2);
        mu = params(i * 3 - 1);
        sigma = params(i * 3);
        y = y + A * exp(-(x - mu).^2 / (2 * sigma^2));
    end
end
```

B.4 Error Calculations

B.4.1 Three-Gaussian Fit Errors

```
function fitThreeGaussiansWithError()

    load('isolated_spectra_velocity.mat');
    main_feature = isolated_spectra_velocity(:,90:230);
    x = main_feature(1, :);
    y = main_feature(2, :);

    % Startpoints for the 3 Gaussians
    startPoints = [4000, 1.25, 0.2, 2500, 1.25, 0.2, 500, 1.25, 0.2
```

```
    % Fit 3 Gaussians
    [fittedParams,resnorm,residual,exitflag,output,lambda,Jacobian]

    % Calculate the standard errors for the fitted parameters
    ci = nlparci(fittedParams, residual, 'jacobian', Jacobian);

    % Extract the standard errors for each Gaussian parameter
    errors = (ci(:,2) - ci(:,1)) / (2 * 1.96); % Assuming 95% confi
    errors = errors/2; %1 sigma error

    % Calculate individual Gaussian components
    numGaussians = 3;
    gaussComponents = zeros(size(x));
    colors = {'b', 'g', 'y'};

    % Display the coefficients and their errors for each Gaussian
    for i = 1:numGaussians
        disp(['Gaussian ', num2str(i)]);
        disp(['Amplitude: ', num2str(fittedParams(i * 3 - 2)), ' ±
        disp(['Mean: ', num2str(fittedParams(i * 3 - 1)), ' ± ', nu
        disp(['Standard Deviation: ', num2str(fittedParams(i * 3)),
    end
end

function y = threeGaussians(params, x)
    numGaussians = 3;
```

```
    y = zeros(size(x));

    for i = 1:numGaussians
        A = params(i * 3 - 2);
        mu = params(i * 3 - 1);
        sigma = params(i * 3);
        y = y + A * exp(-(x - mu).^2 / (2 * sigma^2));
    end
end
```

B.4.2 Ratio Errors

```
%Parameter Coefficients
A1 = 6151.0223;
mu1 = 1.2504;
sigma1 = 0.13565;
A2 = 824.349;
mu2 = 1.2862;
sigma2 = 0.21808;

%Errors
error_A1 = 305.8492;
error_mu1 = 0.00089668;
error_sigma1 = 0.0019205;
error_A2 = 303.5615;
error_mu2 = 0.01262;
error_sigma2 = 0.02126;
```

```
ampsum = A1 + A2
ampsum_error = error_A1 + error_A2
amp_ratio = A2/ampsum
% Calculate the error of the ratio using the formula for propagatio
amp_ratio_error = amp_ratio * sqrt((error_A2 / A2)^2 + (ampsum_erro

mu_sum = calculate_mu_sum(A1, mu1, A2, mu2);
sigma_sum = calculate_sigma_sum(A1, mu1, sigma1, A2, mu2, sigma2);
error_sigma_sum = calculate_error_sigma_sum(sigma_sum, sigma1, erro

widthsum = sigma_sum
widthsum_error = error_sigma_sum
width_ratio = sigma2/widthsum
% Calculate the error of the ratio using the formula for propagatio
width_ratio_error = width_ratio * sqrt((error_sigma2 / sigma2)^2 +

%Sigma (Width parameter sum)
function sigma_sum = calculate_sigma_sum(A1, mu1, sigma1, A2, mu2,
    % Calculate sigma_sum
    numerator = A1 * sigma1^2 + A2 * sigma2^2 + A1 * (mu1 - calcula
    denominator = A1 + A2;
    sigma_sum = sqrt(numerator / denominator);
end

function mu_sum = calculate_mu_sum(A1, mu1, A2, mu2)
    % Calculate mu_sum
```

```
    mu_sum = (A1 * mu1 + A2 * mu2) / (A1 + A2);
end

%Sigma (Width parameter sum) Error
function error_sigma_sum = calculate_error_sigma_sum(sigma_sum, sig
    % Calculate the error in the resulting standard deviation
    error_sigma_sum = sqrt((sigma1 / sigma_sum * error_sigma1)^2 +
end
```

Appendix C

Observation Files

C.1 Key File

```
================================================================
================  Cover Information  ===========================
================================================================

version  = 1
expt     = 'LBA example including Mark5 stations'
expcode  = AUTLive
piname   = 'TN'
address1 = 'AUT University'
address2 = ''
address3 = ''
phone    = 'xxxx'
obsphone = ''
email    = 'tim.natusch@aut.ac.nz'
```

```
 fax      = ''
 obsmode  = 'LBA, 6.7 GHz continuum. 4X16 MHz band, dual pol'
 obstype  = VLBI
 note1    = ''

 ============================================================
 ==============  Correlator Information  ==================
 ============================================================

correl    = LBA
coravg    = 1
corchan   = 32
cornant   = 4
corpol    = 'on'
corwtfn   = 'uniform'
corsrcs   = 'standard'
cortape   = DAT
corship1  =  'Cormac'
corship2  =  'Curtin University'
corship3  =  ''
corship4  =  ''

 ============================================================
 ==================  Program control  =====================
 ============================================================

overwrit
```

```
sumitem = el1, el2, slew, dwell


 ============================================================
 ======= Standard Source and Station Catalogs  ============
 ============================================================

stafile  = \$SCHED/catalogs/stations$_$lba.dat
stafile = \$SCHED/catalogs/stations.cddbbc.dat
stafile = \$SCHED/catalogs/stations.dat
freqfile = \$SCHED/catalogs/freq.dat
srcfile  = \$SCHED/catalogs/sources.vlba

 ============================================================
 ====================  Source Catalog  ======================
 ============================================================

 Methanol Maser G9.62+0.19
srccat /
  source= 'G962'  ra= 18:06:14.659  dec=  -20:31:31.57  equinox= 'J
  source= 'G188'  ra= 06:08:53.35    dec= 21:38:28.7     equinox= '
  source= 'G213'  ra= 06:07:47.87   dec= -06:22:57.0    equinox= 'J
  source= 'G309'  ra= 13:50:41.85    dec= -61:35:11.0    equinox= '
  source= 'G232'  ra= 07:32:09.79    dec= -16:58:12.5    equinox= '
  source= 'G323'  ra= 15:31:45.41    dec= -56:30:50.0    equinox= '
  source= 'G339'  ra= 16:52:04.67    dec= -46:08:34.0    equinox= '
  source= 'G351'  ra= 17:20:53.37    dec= -35:47:02.0    equinox= '
```

```
endcat /

 ============================================================
 ================  Initial Scan Information  ================
 ============================================================

setup = \$SCHED/setups/lba5cm-2p-4IF.set

 LCP and RCP x 4 Chs (i.e 8 Chs of 16 MHz in total)

 ============================================================
 ========================  The Scans  =======================
 ============================================================

year     = 2022
day      = 19
month    = 9
start    = 04:30:00

stations = WARK30M

repeat 2 min observations with 30s interscan a number of times
group 4 repeat 5
source = 'G962'  dur    10:00  gap = 30 intent 'observe' /
source = 'G323'  dur    10:00  gap = 30  intent 'observe' /
source = 'G339'  dur    10:00  gap = 30  intent 'observe' /
source = 'G351'  dur    10:00  gap = 30  intent 'observe' /
```

C.2 VEX File

```
    VEX_rev = 1.5;
*    SCHED vers: Version 11.3 update 1.  April 14, 2014
*    VEX/SCHED:  1.5.87
*    Other versions: Sched:  11.3  Plot: 1.06  JPL-ephem: 1.01
*-----------------------------------------------------------------
$GLOBAL;
     ref $EXPER = HWmaser;
*                                                    +-----------
*                          PI revision number:       |    1.0000
*                                                    +-----------
*    mode:       LBA, 6.7 GHz continuum. 4X16 MHz band, dual pol
*-----------------------------------------------------------------
$EXPER;
*
def HWmaser;
     exper_name = HWmaser;
     exper_description = "LBA example including Mark5 stations";
     PI_name = HW;
     PI_email = tim.natusch@aut.ac.nz;
*    address:   AUT University
*
*
*
*    phone:     xxxx
*    during obs:
```

```
*     fax:
*
*     year, doy: 2022, 262
*     date      : Mon 19 Sep 2022
*     MJD       : 59841
      exper_nominal_start=2022y262d04h50m00s;
      exper_nominal_stop=2022y262d08h41m40s;
*
      target_correlator = LBA;
*
*     integr_time    :     1.000 s
*     number_channels:    32
*     number_antenna :  4
*     cross_polarize : Yes
*     weight_func    : UNIFORM
*     distrib_medium : DAT
*     distrib_format : FITS
*     source_pos_cat : STANDARD
*     distribute_to  :
*                      Cormac
*                      Curtin University
*
enddef;
*----------------------------------------------------------------------
$MODE;
*
def lba5cm-2p-4IF;
```

```
     ref $PROCEDURES = Mode_01;
     ref $FREQ = 6660.00MHz4x16MHz:Wa;
     ref $IF = LO@5843MHzDPolNoTone:Wa;
     ref $BBC = 4BBCs:Wa;
     ref $TRACKS = MARK5B.4Ch2bit1to1:Wa;
*    ref $HEAD_POS = DiskVoid <= obsolete definition
     ref $ROLL = NoRoll:Wa;
*    ref $PASS_ORDER = DiskVoid <= obsolete definition
     ref $PHASE_CAL_DETECT = NoDetect:Wa;
enddef;
*----------------------------------------------------------------------
$STATION;
*
def Wa;
     ref $SITE = WARK30M;
     ref $ANTENNA = WARK30M;
     ref $DAS = 2DBBC+NONE<;
enddef;
*----------------------------------------------------------------------
$PROCEDURES;
*
def Mode_01;
     procedure_name_prefix =  "01";
     tape_change =  420 sec;
     headstack_motion =    6 sec;
     new_source_command =    5 sec;
     new_tape_setup =   20 sec;
```

```
     setup_always = on :  20 sec;
     parity_check = off : 100 sec;
     tape_prepass = off : 600 sec;
     preob_cal  = on :  10 sec : preob;
     midob_cal  = on :  15 sec : midob;
     postob_cal = on :   0 sec : postob;
enddef;
*----------------------------------------------------------------------
$SITE;
*
def WARK30M;
     site_type = fixed;
     site_name = WARK30M;
     site_ID = Wa;
*    elev=  117.37 long=-174:39:46. lat=-36:25:59.4
     site_position =-5115421.01200 m:  477880.25300 m:-3767040.1550
     site_velocity =  0.000000   m/yr:  0.000000   m/yr:  0.000000
*    First line below is VEX standard format.  Use only when readers
*    site_position_epoch = 1858y322d;
     site_position_epoch =       0;
enddef;
*----------------------------------------------------------------------
$ANTENNA;
*
def WARK30M;
     axis_type = az : el;
     antenna_motion = el :  21.6 deg/min :  2 sec;  *    0.250 deg/
```

```
     antenna_motion = az :  22.2 deg/min :  2 sec;  *    0.200 deg/
     axis_offset =    2.50000 m;
enddef;
*----------------------------------------------------------------------
$DAS;
*
def 2DBBC+NONE<;
     record_transport_type = Mark5B;
     electronics_rack_type = DBBC;
     number_drives = 2;
     headstack = 1 :            : 0 ;
     headstack = 2 :            : 1 ;
     tape_motion = adaptive : 0 min: 0 min: 10 sec;
enddef;
*----------------------------------------------------------------------
$SOURCE;
*
def G962;
     source_name = G962;
*    this source had calibrator code:
     ra = 18h06m14.6590000s; dec = -20d31'31.570000"; ref_coord_fra
*    ra = 18h03m15.8587229s; dec = -20d31'52.362691"; ref_coord_fra
*    ra = 18h07m35.1285308s; dec = -20d31'23.812060"; ref_coord_fra
enddef;
*
def G323;
     source_name = G323;
```

```
*    this source had calibrator code:
     ra = 15h31m45.4100000s; dec = -56d30'50.000000"; ref_coord_fra
*    ra = 15h27m51.8047317s; dec = -56d20'39.080334"; ref_coord_fra
*    ra = 15h33m29.2354493s; dec = -56d35'34.168537"; ref_coord_fra
enddef;
*
def G339;
     source_name = G339;
*    this source had calibrator code:
     ra = 16h52m04.6700000s; dec = -46d08'34.000000"; ref_coord_fra
*    ra = 16h48m24.6398160s; dec = -46d03'33.571317"; ref_coord_fra
*    ra = 16h53m43.1663465s; dec = -46d10'58.115508"; ref_coord_fra
enddef;
*
def G351;
     source_name = G351;
*    this source had calibrator code:
     ra = 17h20m53.3700000s; dec = -35d47'02.000000"; ref_coord_fra
*    ra = 17h17m32.2266662s; dec = -35d44'04.543867"; ref_coord_fra
*    ra = 17h22m23.6092977s; dec = -35d48'28.137643"; ref_coord_fra
enddef;
*----------------------------------------------------------------
$FREQ;
*
def 6660.00MHz4x16MHz;
* mode =  1    stations =Wa
     sample_rate =  32.000 Ms/sec;  * (2bits/sample)
```

```
     chan_def = :  6660.00 MHz : U :  16.00 MHz : &CH01 : &BBC01 : &
     chan_def = :  6660.00 MHz : U :  16.00 MHz : &CH02 : &BBC05 : &
     chan_def = :  6676.00 MHz : U :  16.00 MHz : &CH03 : &BBC02 : &
     chan_def = :  6676.00 MHz : U :  16.00 MHz : &CH04 : &BBC06 : &
enddef;
*----------------------------------------------------------------------
$IF;
*
def LO@5843MHzDPolNoTone;
* mode =  1    stations =Wa
     if_def = &IF_A1 : A1 : R :  5843.00 MHz : U ; * PCall off!   0
     if_def = &IF_B2 : B2 : L :  5843.00 MHz : U ; * PCall off!   0
enddef;
*----------------------------------------------------------------------
$BBC;
*
def 4BBCs;
* mode =  1    stations =Wa
     BBC_assign = &BBC01 :  1 : &IF_A1;
     BBC_assign = &BBC05 :  5 : &IF_B2;
     BBC_assign = &BBC02 :  2 : &IF_A1;
     BBC_assign = &BBC06 :  6 : &IF_B2;
enddef;
*----------------------------------------------------------------------
$PHASE_CAL_DETECT;
*
def NoDetect;
```

```
* mode =  1    stations =Wa
     phase_cal_detect = &NoCal;
enddef;
*-------------------------------------------------------------------
$TRACKS;
*
def MARK5B.4Ch2bit1to1;
* mode =  1    stations =Wa
*    firmware_type = DBBC_DDC;
*    format = MARK5B, and fan-out = 1
*    mode requires  32.00Mb/s/tr; stations using disks
     track_frame_format = MARK5B;
     fanout_def =   : &CH01 : sign : 1:  2;
     fanout_def =   : &CH01 :  mag : 1:  3;
     fanout_def =   : &CH02 : sign : 1:  6;
     fanout_def =   : &CH02 :  mag : 1:  7;
     fanout_def =   : &CH03 : sign : 1:  4;
     fanout_def =   : &CH03 :  mag : 1:  5;
     fanout_def =   : &CH04 : sign : 1:  8;
     fanout_def =   : &CH04 :  mag : 1:  9;
enddef;
*-------------------------------------------------------------------
$HEAD_POS;
def DiskVoid;
* mode =  1    stations =Wa
*     Head positions irrelevant for Disk: empty def
enddef;
```

```
*------------------------------------------------------------------
$PASS_ORDER;
*
def DiskVoid;
* mode =  1    stations =Wa
*     Pass orders irrelevant for Disk: empty def
enddef;
*------------------------------------------------------------------
$ROLL;
*
def NoRoll;
* mode =  1    stations =Wa
*    barrel-roll set to 'roll_off', so reverse-roll by  0 (1 head)
     roll = off;
enddef;
*------------------------------------------------------------------
$SCHED;
* schedule section for experiment HWmaser
* LBA example including Mark5 stations
scan No0001;
* intent = "observe"
     start=2022y262d04h50m00s; mode=lba5cm-2p-4IF; source=G962;
*              :data_good:data_stop:goto_foot: pass:  wrap :driv:tap
     station=Wa:    0 sec:  600 sec:    0.000 GB:   :       : 1;
endscan;
scan No0002;
* intent = "observe"
```

```
     start=2022y262d05h01m40s; mode=lba5cm-2p-4IF; source=G323;
     station=Wa:  292 sec:  600 sec:   19.231 GB:   :       : 1;
endscan;
scan No0003;
* intent = "observe"
     start=2022y262d05h13m20s; mode=lba5cm-2p-4IF; source=G339;
     station=Wa:    0 sec:  600 sec:   38.461 GB:   :       : 1;
endscan;
scan No0004;
* intent = "observe"
     start=2022y262d05h25m00s; mode=lba5cm-2p-4IF; source=G351;
     station=Wa:  164 sec:  600 sec:   57.692 GB:   :       : 1;
endscan;
scan No0005;
* intent = "observe"
     start=2022y262d05h36m40s; mode=lba5cm-2p-4IF; source=G962;
     station=Wa:    4 sec:  600 sec:   76.923 GB:   :       : 1;
endscan;
scan No0006;
* intent = "observe"
     start=2022y262d05h48m20s; mode=lba5cm-2p-4IF; source=G323;
     station=Wa:  380 sec:  600 sec:   96.154 GB:   :       : 1;
endscan;
scan No0007;
* intent = "observe"
     start=2022y262d06h00m00s; mode=lba5cm-2p-4IF; source=G339;
     station=Wa:    0 sec:  600 sec:  115.384 GB:   :       : 1;
```

```
endscan;
scan No0008;
* intent = "observe"
     start=2022y262d06h11m40s; mode=lba5cm-2p-4IF; source=G351;
     station=Wa:   61 sec:  600 sec:  134.615 GB:   :       : 1;
endscan;
scan No0009;
* intent = "observe"
     start=2022y262d06h23m20s; mode=lba5cm-2p-4IF; source=G962;
     station=Wa:  600 sec:  600 sec:  153.846 GB:   :       : 1;
endscan;
scan No0010;
* intent = "observe"
     start=2022y262d06h35m00s; mode=lba5cm-2p-4IF; source=G323;
     station=Wa:  290 sec:  600 sec:  173.076 GB:   :       : 1;
endscan;
scan No0011;
* intent = "observe"
     start=2022y262d06h46m40s; mode=lba5cm-2p-4IF; source=G339;
     station=Wa:    0 sec:  600 sec:  192.307 GB:   :       : 1;
endscan;
scan No0012;
* intent = "observe"
     start=2022y262d06h58m20s; mode=lba5cm-2p-4IF; source=G351;
     station=Wa:    0 sec:  600 sec:  211.538 GB:   :       : 1;
endscan;
scan No0013;
```

```
* intent = "observe"
     start=2022y262d07h10m00s; mode=lba5cm-2p-4IF; source=G962;
     station=Wa:   80 sec:  600 sec:  230.769 GB:   :       : 1;
endscan;
scan No0014;
* intent = "observe"
     start=2022y262d07h21m40s; mode=lba5cm-2p-4IF; source=G323;
     station=Wa:  184 sec:  600 sec:  249.999 GB:   :       : 1;
endscan;
scan No0015;
* intent = "observe"
     start=2022y262d07h33m20s; mode=lba5cm-2p-4IF; source=G339;
     station=Wa:    0 sec:  600 sec:  269.230 GB:   :       : 1;
endscan;
scan No0016;
* intent = "observe"
     start=2022y262d07h45m00s; mode=lba5cm-2p-4IF; source=G351;
     station=Wa:    0 sec:  600 sec:  288.461 GB:   :       : 1;
endscan;
scan No0017;
* intent = "observe"
     start=2022y262d07h56m40s; mode=lba5cm-2p-4IF; source=G962;
*              :data_good:data_stop:goto_foot: pass:  wrap :driv:tap
     station=Wa:   24 sec:  600 sec:  307.691 GB:   :       : 1;
endscan;
scan No0018;
* intent = "observe"
```

```
     start=2022y262d08h08m20s; mode=lba5cm-2p-4IF; source=G323;
     station=Wa:  119 sec:  600 sec:  326.922 GB:   :       : 1;
endscan;
scan No0019;
* intent = "observe"
     start=2022y262d08h20m00s; mode=lba5cm-2p-4IF; source=G339;
     station=Wa:    0 sec:  600 sec:  346.153 GB:   :       : 1;
endscan;
scan No0020;
* intent = "observe"
     start=2022y262d08h31m40s; mode=lba5cm-2p-4IF; source=G351;
     station=Wa:    0 sec:  600 sec:  365.384 GB:   :       : 1;
endscan;
```